Doctoral Dissertation

Studies on Acceptor Materials for Organic Photovoltaics Based on Molecular Arrangement Control in Thin-film by Molecular Design

Seihou Jinnai

January 2017

Graduate School of Engineering,
Osaka University

Preface

The study presented in this thesis has been carried out under the guidance of Professor Yoshio Aso at The Institute of Scientific and Industrial Research (ISIR), Osaka University from April 2011 to March 2016.

This thesis concerns the synthesis, properties, and photovoltaic performances of new π-conjugated compounds bearing electron withdrawing groups as acceptor materials in organic photovoltaic devices. The objective of this work is to provide insight into the relationships among the chemical structure, physical properties, thin-film properties, and photovoltaic performances of photovoltaic device for advanced acceptor material in organic photovoltaics.

The author hopes that the results and information presented in this thesis can contribute to further developments of advanced materials in organic photovoltaics.

Department of Applied Chemistry
Graduate School of Engineering
Osaka University

Suita, Osaka, Japan
January 2017

Seihou Jinnai

Table of Contents

General Introduction

As the growth of worldwide energy demand and environmental issue with an increasing industrialization of the world, solar cells have attracted much attention as renewable and alternative energy source. Of the various photovoltaic technologies, organic photovoltaics (OPVs) based on solution processing methods are one of the next-generation solar cells because of their advantages of low cost, light weight, and large-area manufacturability.[1] One of the state-of-the-art OPVs relied on the concept of bulk-heterojunction (BHJ) structure, with the organic active layer of donor and acceptor materials (Figure 1).[2] The bulk mixture of the polymer donor (p-type) and the small molecule acceptor (n-type) materials with phase-separated domain regions allow implementation of efficient photocarrier generation at extended donor/acceptor interface. On the other hand, the BHJ structure is not always effective for charge carrier transport and collection and thus fine control of nanoscale phase separation is inevitably needed to achieve both efficient photocarrier generation and charge carrier transport.[3] In addition to this, since the efficiency of photocarrier generation depends on the nature of donor/acceptor interface, construction of optimal interface is necessary to improve the efficiency. However, the difficulty of direct analysis and tuning donor/acceptor interfaces are thought to be the critical issue for development of materials.

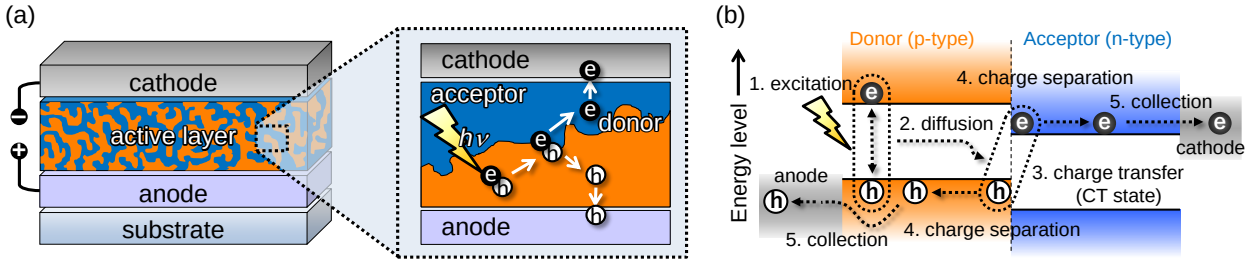

Figure 1. (a) Schematic structure of BHJ type organic photovoltaic devices and (b) process of photoelectric conversion.

Since the first time Yu *et al.* fabricated BHJ type photovoltaic device, which comprises a blend of a solubilized π-conjugated polymer as a donor material and a solubilized fullerene derivative as an acceptor material,[4]remarkable progress in donor materials have promoted a significant increase in the power conversion efficiency (PCE) of OPVs (Figure 2).[5] In contrast, developments of new acceptor materials has been relatively slow, and only a limited series of fullerene derivatives such as [6,6]-phenyl-C_x-butyric acid methyl ester (x = 61 and 71) (PC_xBM) are employed as effective acceptor materials, due to the advantages of low reorganization energy, a long-lived charge-separated state, and a rapid and isotropic mobility of electrons.[6] Despite these unique features, fullerene derivatives have an unfortunate drawback, i.e., a weak absorption in the visible region, which results in a limited light-harvesting efficiency, limited tunability in electronic structure, high synthetic costs, and morphological instability in the BHJ film.[7] Thus, novel acceptors as alternatives to fullerene derivatives are highly desired to boost the performance and diversity of OPVs.[8]

On these accounts, extended π-conjugated compounds containing electron-withdrawing groups, such as rylene diimide,[9] diketopyrrolopyrrole,[10] and benzothiadiazole[11] and others[12] are highlighted as alternative acceptor materials. This class of acceptors provides tunable absorption properties, frontier molecular orbital energy levels,

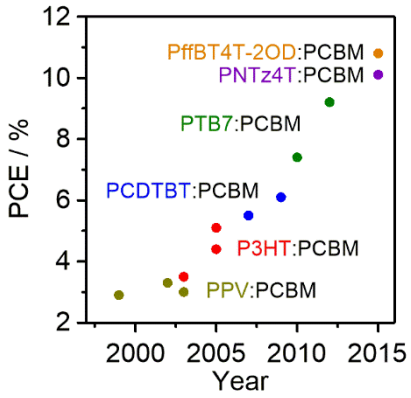

Figure 2. Timeline of PCEs in OPVs.

and thin-film properties due to their synthetic flexibility. However, the progress has been limited due to a lack of acceptor design guideline and, in this context, the basic knowledge among the chemical structure, physical properties, thin-film properties, and photovoltaic performances is essential for advancement in the research area of OPVs.

In this thesis, the author has focused on the relationship among the structural feature, physical properties, thin-film properties, and photovoltaic performances of new electron-accepting π-conjugated compounds. The thesis is divided into four chapters, each one treating different concepts of chemical structures.

Chapter 1 focuses on a series of new three-dimensional (3-D) structured acceptor materials based on the combination of a tetrahedral-covalent Si atom at the center and oligothiophenes having dicyanomethylene-substituted difluorocyclopenta[*b*]thiophene at the four arms and elucidates their OPV performances.

In chapter 2, the author elucidated the physical, thin-film, and photovoltaic characters of linearly extended phthalimide and phthaldithioimide-based acceptor materials which are suitable for investigation of structure−properties−OPV performances relationship due to its synthetic flexibility.

In chapter 3, the work is focused on the influence of structural modification of the linearly extended acceptor materials on molecular properties and orientation at donor/acceptor interfaces. The thin-film properties and OPV performances were systematically investigated using diethynylbenzothiadiazole/phthalimide based acceptors.

In the final chapter, the author designed and synthesized extended π-electron compounds with 3-D structure using perylene bisimide units. The thin-film properties and OPV performances of three-dimensional acceptors were discussed.

References

1 B. C. Thompson and J. M. J. Fréchet, *Angew. Chem., Int. Ed.*, 2008, **47**, 58; G. Dennler, M. C. Scharber and C. J. Brabec, *Adv. Mater.*, 2009, **21**, 1323; C. J. Brabec, S. Gowrisanker, J. J. M. Halls, D. Laird, S. Jia and S. P. Williams, *Adv. Mater.*, 2010, **22**, 3839; M. Jørgensen, K. Norrman, S. A. Gevorgyan, T. Tromholt, B. Andreasen and F. C. Krebs, *Adv. Mater.*, 2012, **24**, 580.

2 G. Li, R. Zhu and Y, Yang, *Nat. Photonics*, 2012, **6**, 153; H. Zhou, L. Yang and W. You, *Macromolecules*, 2012, **45**, 607; B. Walker, C. Kim and T.-Q. Nguyen, *Chem. Mater.*, 2011, **23**, 470; Y. Lin, Y. Li and X. Zhan, *Chem. Soc. Rev.*, 2012, **41**, 4245; A. Mishra and P. Bäuerle, *Angew. Chem.*, 2012, **124**, 2060; *Angew. Chem., Int. Ed.*,

2012, **51**, 2020.

3 M. T. Dang, L. Hirsch, G. Wantz and J. D. Wuest, *Chem. Rev.*, 2013, **113**, 3734

4 G. Yu, J. Gao, J. C. Hummelen, F. Wudl and A. J. Heeger, *Science*, 1995, **270**, 1789.

5 C. J. Brabec, S. E. Shaheen, C. Winder and N. S. Sariciftci, *Appl. Phys. Lett.*, 2002, **80**, 1288; M. M. Wienk, J. M. Kroon, W. J. Verhees, J. Knol, J. C. Hummelen, P. A. v. Hal and R. A. J. Janssen, *Angew. Chem., Int. Ed.*, 2003, **42**, 3371; F. Padinger, R. S. Rittberger and N. S. Sariciftci, *Adv. Funct. Mater.*, 2003, **13**, 85; G. Li, V. Shrotriya, J. Huang, Y. Yao, T. Moriarty, K. Emery and Y. Yang, *Nat. Mater.*, 2005, **4**, 864; J. Peet, J. Y. Kim, N. E. Coates, W. L. Ma, D. Moses, A. J. Heeger and G. C. Bazan, *Nat. Mater.*, 2007, **6**, 497; S. H. Park, A. Roy, S. Beaupré, S. Cho, N. Coates, J. S. Moon, D. Moses, M. Leclerc, K. Lee and A. J. Heeger, *Nat. Photonics*, 2009, **3**, 297; Y. Liang, Z. Xu, J. Xia, S.-T. Tsai, Y. Wu, G. Li, C. Ray and L. Yu, *Adv. Mater.*, 2010, **22**, E135; Z. He, C. Zhong, S. Su, M. Xu, H. Wu and Y. Cao *Nat. Photonics*, 2012, **6**, 591; Y. Liu, J. Zhao, Z. Li, C. Mu, W. Ma, H. Hu, K. Jiang, H. Lin, H. Ade and H. Yan *Nat. Commun.*, 2014, **5**, 5293; V. Vohral, K. Kawashima, T. Kakara, T. Koganezawa, I. Osaka, K. Takimiya and H. Murata *Nat. Photonics*, 2015, **9**, 403.

6 J. W. Jung, J. W. Jo, C.-C. Chueh, F. Liu, W. H. Jo, T. P. Russell, A. K.-Y. Jen, *Adv. Mater.*, 2015, **27**, 3310; C.-H. Wu, C.-C. Chueh, Y.-Y. Xi, H.-L. Zhong, G.-P. Gao, Z.-H. Wang, L. D. Pozzo, T.-C. Wen and A. K.-Y. Jen, *Adv. Funct. Mater.*, 2015, **25**, 5326.

7 D. Sun, D. Meng, Y. Cai, B. Fan, Y. Li, W. Jiang, L. Huo, Y. Sun and Z. Wang, *J. Am. Chem. Soc.*, 2015, **137**, 11156; G. Sauvé and R. Fernando, *J. Phys. Chem. Lett.*, 2015, **6**, 3770; Y. Lin, J. Wang, Z.-G. Zhang, H. Bai, Y. Li, D. Zhu and X, Zhan, *Adv. Mater.*, 2015, **27**, 1170; Y. Lin, Z.-G. Zhang, H. Bai, J. Wang, Y. Yao, Y. Li, D. Zhu and X. Zhan, *Energy Environ. Sci.*, 2015, **8**, 610.

8 A. Facchetti, *Mater. Today*, 2013, **16**, 123; A. F. Eftaiha, J.-P. Sun, I. G. Hill and G. C. Welch, *J. Mater. Chem. A*, 2014, **2**, 1201; Y. Lin and X. Zhan, *Mater. Horiz.*, 2014, **1**, 470; S. M. McAfee, J. M. Topple, I. G. Hill and G. C. Welch, *J. Mater. Chem. A*, 2015, **3**, 16393.

9 G. D. Sharma, M. Anil Reddy, D. V. Ramana and M. Chandrasekharam, *RSC Adv.*, 2014, **4**, 33279; Y. Zhong, M. T. Trinh, R. Chen, W. Wang, P. P. Khlyabich, B. Kumar, Q. Xu, C.-Y. Nam, M. Y. Sfeir, C. Black, M. L. Steigerwald, Y.-L. Loo, S. Xiao, F. Ng, X.-Y. Zhu and C. Nuckolls, *J. Am. Chem. Soc.*, 2014, **136**, 15215; J. Zhao, Y. Li, H, Lin, Y. Liu, K. Jiang, C. Mu, T. Ma, J. Y. L. Lai, H. Hu, D. Yu and H. Yan, *Energy Environ. Sci.*, 2015, **8**, 520; X. Zhang, C. Zhan, J. Yao, *Chem. Mater.*, 2015, **27**, 166; Y. Liu, J. Y. L. Lai, S. Chen, Y. Li, K. Jiang, J. Zhao, Z. Li, H. Hu, T. Ma, H. Lin, J. Liu, J. Zhang, F. Huang, D. Yu and H. Yan, *J. Mater. Chem. A*, 2015, **3**, 13632.

10 Y. Lin, Y. Li and X. Zhan, *Adv. Energy Mater.*, 2013, **3**, 724; H. Shi, W. Fu, M. Shi, J. Ling and H. Chen, *J. Mater. Chem. A*, 2015, **3**, 1902.

11 J. T. Bloking, T. Giovenzana, A. T. Higgs, A. J. Ponec, E. T. Hoke, K. Vandewal, S. Ko, Z. Bao, A. Sellinger and M. D. McGehee, *Adv. Energy Mater*., 2014, **4**, 1301426; O. K. Kwon, J.-H. Park, S. K. Park and S. Y. Park, *Adv. Energy Mater*., 2015, **5**, 1400929; S. Holliday, R. S. Ashraf, C. B. Nielsen. M. Kirkus, J. A. Röhr, C.-H. Tan, E. Collado-Fregoso, A.-C. Knall, J. R. Durrant, J. Nelson and I. McCulloch, *J. Am. Chem. Soc.*, 2015, **137**, 898.

12 Y. Kim, C. E. Song, S.-J. Moon and E. Lim, *Chem. Commun.*, 2014, **50**, 8235; Z. Mao, W. Senevirathna, J.-Y.

Liao, J. Gu, S. V. Kesava, C. Guo, E. D. Gomez and G. Sauvé, *Adv. Mater.*, 2014, **26**, 6290; H. Li, Y.-J. Hwang, B. A. E. Courtright, F. N. Eberle, S. Subramaniyan and S. A. Jenekhe, *Adv. Mater.*, 2015, **27**, 3266.

Chapter 1
Three-Dimensional Electron Acceptor Materials Bearing Dicyanomethylene-Substituted Difluorocyclopenta[*b*]thiophene

1.1 Introduction

Since the first use of fullerene derivatives in BHJ type OPVs, PC_xBM (x = 61 and 71) have been widely adopted as the standard acceptor material of choice and much progress has been made in efficiency, device architecture, and physical principles of OPVs. The intrinsic properties of fullerenes, such as high electron mobility, electron acceptability, exciton diffusion length, and small internal reorganization energy are favorable factors for acceptor materials in OPVs. Furthermore, it is considered the extended the lowest unoccupied molecular orbital (LUMO) distribute through the isotropic 3-D spherical structure can play a positive role in electron transport across acceptor domains. In this chapter, from these viewpoints, the author focused on the 3-D shaped π-conjugated acceptor materials.

In 2013, in terms of structural modifications, we demonstrated that 3-D arrangements of π-conjugated molecules has an advantage to construct the isotropic electron-transporting pathways in the BHJ films, leading to promising photovoltaic performances.[1] In very recently 3-D arranged rylene diimide derivatives are demonstrated as promising acceptor materials by several groups.[2] Under this situation, the author designed and synthesized new 3-D electron-transporting π-conjugated compounds based on the combination of a tetrahedral-covalent Si atom at the center and oligothiophenes having dicyanomethylene-substituted difluorocyclopenta[*b*]thiophene[3] at the four arms (**Tetra-T-BCN**, and **Tetra-TT-BCN**) and evaluated their properties and OPV performance (Figure 1.1). Through comparing the OPV characteristics of 3-D arranged and planar acceptor materials (**Tetra-TT-BCN**), the effectiveness of molecular arrangements are elucidated.

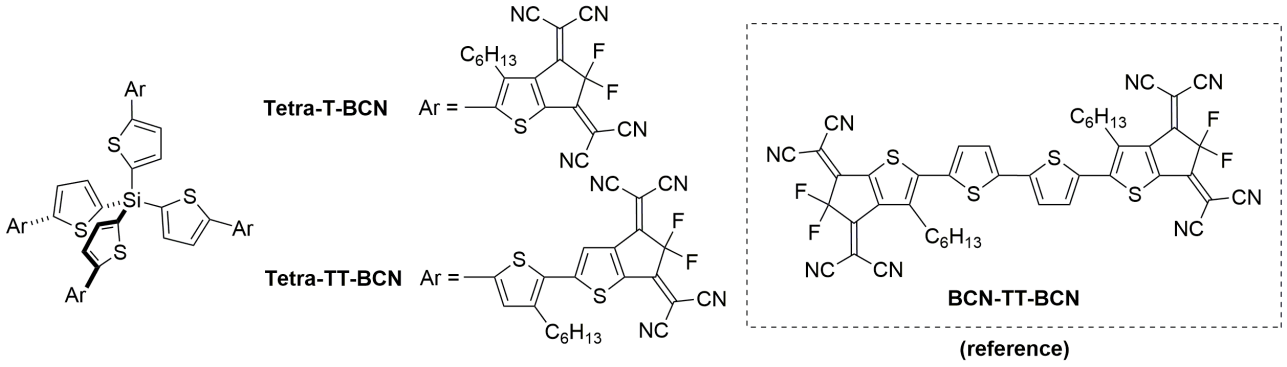

Figure 1.1. Chemical structures of **Tetra-T-BCN**, **Tetra-TT-BCN**, and **BCN-TT-BCN**.

1.2 Synthesis

The synthetic route of the target 3-D acceptor compounds **Tetra-T-BCN** and **Tetra-TT-BCN** are shown in Scheme 1. Tetrastannyl compound **2** was obtained by the lithiation of tetra(2-thienyl)silane (**1**) using *n*-BuLi in the presence of *N*,*N*,*N*′,*N*′-tetramethylethylenediamine (TMEDA) followed by quenching with tetrabutyltin chloride.[4] **Tetra-T-BCN** was synthesized by a palladium-catalyzed Stille coupling between **2** and 4.8 equiv. of **3**[3] under microwave irradiation (180 ºC, 5 min.) in a yield of 39%. The compound **6** was synthesized by the Stille coupling of **4** with 2-

tributylstannylthiophene, followed by bromination with NBS in DMF at 70 ºC. Then, the Knoevenagel condensation of **6** with malononitrile gave **7**. Finally, **Tetra-TT-BCN** was afforded by **2** and **6** under the Stille coupling reaction conditions. Owing to the contribution of non-planar molecular structure and solubilizing hexyl groups, both target compounds possess enough solubility in common organic solvents such as chloroform and *o*-dichlorobenzene, enabling us to purify them using gel-permeation chromatography (GPC) as well as to characterize their properties and semiconducting performance.

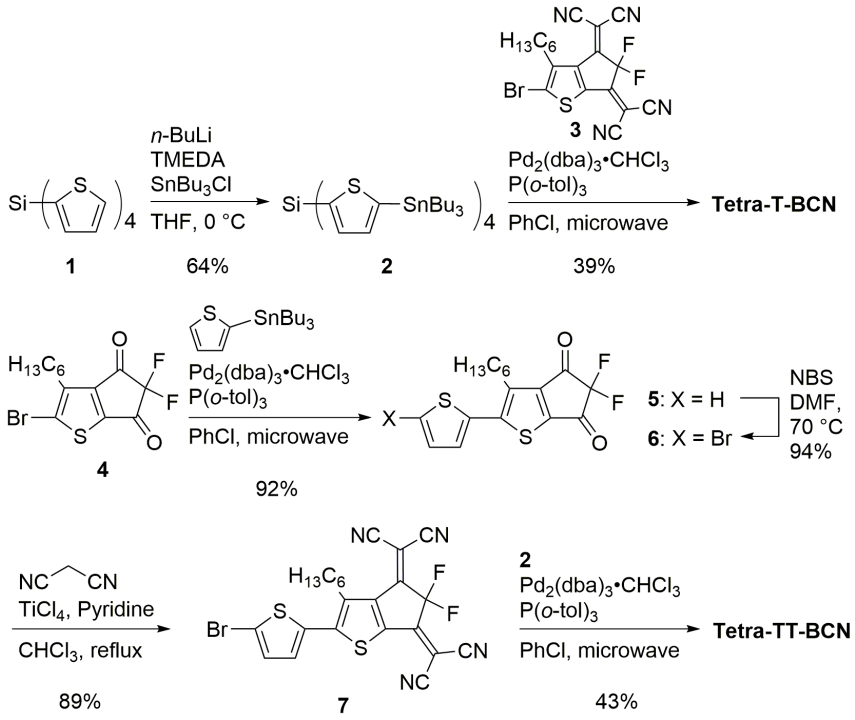

Scheme 1.1. Synthesis of **Tetra-T-BCN** and **Tetra-TT-BCN**.

1.3 Photophysical and Electrochemical Properties

The UV-vis absorption spectra of **Tetra-T-BCN** and **Tetra-TT-BCN** in chloroform display in Figure 1.2 (a), and the photophysical data are outlined in Table 1. The absorption spectrum of **Tetra-T-BCN** showed two bands at 361 and 462 nm. According to time-dependent density functional theory (DFT) calculations at the B3LYP/6-31G (d,p) level, the higher energy band is mainly attributed to transitions from the highest occupied molecular orbital (HOMO)–1 to LUMO and from HOMO to LUMO+1, and the lower energy band is attributed to HOMO–LUMO transition. The extension of π-conjugation from **Tetra-T-BCN** to **Tetra-TT-BCN** led to a pronounced red-shift of these absorptions, resulting in covering a broad wavelength range from 300 to 700 nm. The absorption onsets of 537 and 642 nm for **Tetra-T-BCN** and **Tetra-TT-BCN** correspond to the estimation of HOMO–LUMO energy gaps (ΔE_{opt}) of 2.31 and 1.93 eV, respectively. The redox potentials of these compounds were investigated by cyclic voltammetry (CV) in dichloromethane containing 0.1 M tetrabutylammonium hexafluorophosphate ($TBAPF_6$) as a supporting electrolyte by using a platinum-plate working electrode, a platinum wire as a counter electrode, and $Ag/AgNO_3$ as a reference electrode. The cyclic voltammograms are shown in Figure 1.2 (b), and the electrochemical data are summarized in Table 1. The potentials were calibrated using a ferrocene/ferrocenium (Fc/Fc^+) redox couple

as an internal standard. While no oxidation wave was observed within the measureable potential range (< +1.0 V vs Fc/Fc^+), both the compounds showed two reversible reduction waves. Since the presence of a Si atom disrupts the conjugation between neighboring oligothiophenes, we assigned that each reduction wave consists of the four-electron process. **Tetra-T-BCN** exhibited the first half-wave reduction potential ($E_{red}^{1/2}$) at −0.55 V, which is very similar to that of **Tetra-TT-BCN** (−0.57 V), indicating that the extension of conjugation has no significant influence on the reduction process of the BCN-containing π-system. This phenomenon is rationalized by the DFT calculations that LUMOs of model compounds are mainly localized on the electron-accepting BCN unit (Figure 1.3). Under the assumption that the energy level of Fc/Fc^+ is –4.8 eV below the vacuum level,[5] the LUMO energy levels (E_{LUMO}) of **Tetra-T-BCN** and **Tetra-TT-BCN** were estimated to be –4.25 and –4.23 eV, respectively, whose values are lower than that of $PC_{61}BM$ (–3.72 eV) determined under the same measurement conditions.

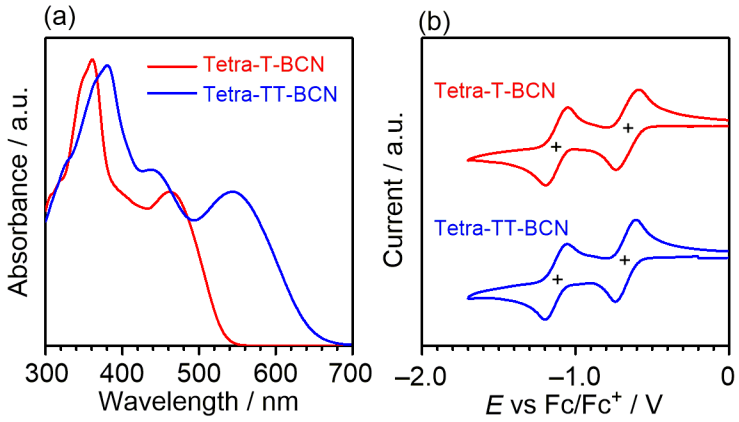

Figure 1.2. (a) UV-vis absorption spectra in chloroform and (b) cyclic voltammograms in dichloromethane containing 0.1 M $TBAPF_6$.

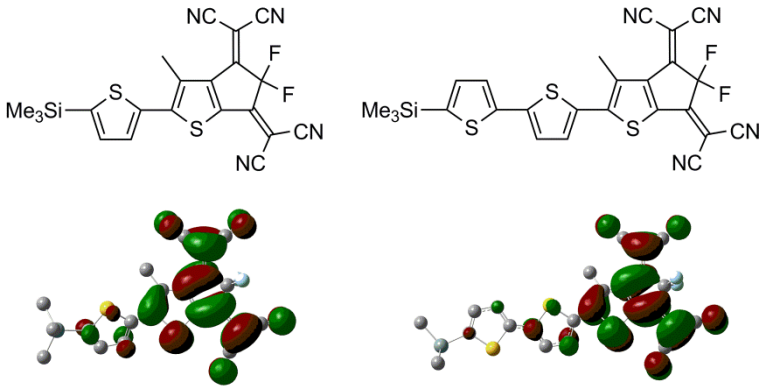

Figure 1.3. Chemical structures of model compounds and calculated LUMOs at the B3LYP/6-31G(d,p) level.

Table 1.1. Properties of **Tetra-T-BCN**, **Tetra-TT-BCN**, and **BCN-TT-BCN**.

Compounds	λ_{max} [nm][a]	ΔE_{opt} [eV][b]	$E_{red}^{1/2}$ [V][c]	E_{LUMO} [eV][d]	E_{HOMO} [eV][e]	μ_e [$cm^2 V^{-1} s^{-1}$]
Tetra-T-BCN	361, 462	2.31	−0.55, −1.12	–4.25	–6.56	3.7×10^{-6}
Tetra-TT-BCN	381, 437, 544	1.93	−0.57, −1.13	–4.21	–6.14	5.0×10^{-6}
BCN-TT-BCN	591	1.81	–0.67	–4.13	–5.94	5.4×10^{-4}

[a] In $CHCl_3$. [b] Determined by the onset of the UV-Vis absorption spectrum in $CHCl_3$. [c] In dichloromenthane containing 0.1 M $TBAPF_6$, V vs. Fc/Fc^+. [d] The approximation for the Fc/Fc^+ level is –4.8 eV vs. vacuum level. [e] Determined by E_{LUMO} and ΔE_{opt}.

1.4 Electron Mobilities and Photovoltaic Performances

Organic Field-effect transistors (OFETs) with a bottom-contact and bottom-gate configuration were employed to estimate the electron-transporting properties of **Tetra-T-BCN** and **Tetra-TT-BCN**. The active layers of **Tetra-T-BCN** and **Tetra-TT-BCN** were formed by spin-coating from a 0.5 wt% chloroform solution on the hexamethyldisilazane (HMDS)-modified SiO_2 dielectric. Irrespective of the 3-D structure disadvantageous to the carrier transport in OFETs, **Tetra-T-BCN** and **Tetra-TT-BCN** retained n-type OFET responses with electron mobilities (μ_e) of 3.7×10^{-6} and 5.0×10^{-6} $cm^2 V^{-1} s^{-1}$, respectively.

To investigate the properties of BHJ blend films of **Tetra-T-BCN** and **Tetra-TT-BCN** with a donor polymer poly(3-hexylthiophene) (P3HT) (1:1 w/w), flash-photolysis time-resolved microwave-conductivity (FP-TRMC) measurements were performed.[6] As shown in Figure 1.4 (a), the photoconductivity ($\phi\Sigma\mu$) of the P3HT/**Tetra-T-BCN** blend film was inferior to a pristine P3HT film. In contrast, both the $\phi\Sigma\mu$ maximum and its lifetime of the P3HT/**Tetra-TT-BCN** film were increased compared with those of P3HT/**Tetra-T-BCN**, suggestive of the better photovoltaic performance of the former. As shown in Figure 1.4 (b), P3HT photoluminescence of the P3HT/**Tetra-TT-BCN** film was almost quenched, whereas a detectable fluorescence remained for P3HT/**Tetra-T-BCN**. These results indicate that **Tetra-TT-BCN** has more suitable potential for the photo-induced charge transfer from P3HT.

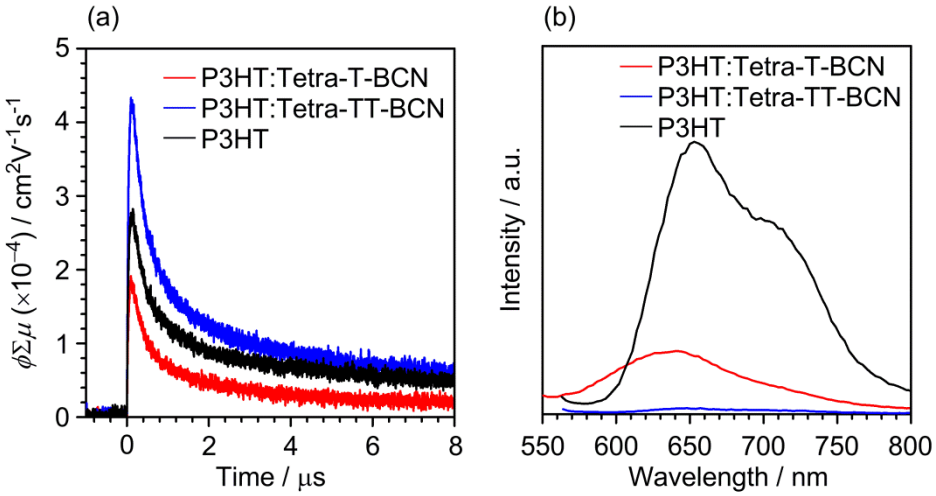

Figure 1.4. (a) FP-TRMC transients of P3HT (black), P3HT/**Tetra-T-BCN** (red), P3HT/**Tetra-TT-BCN** (blue) blend films. The transients were recorded upon exposure to a 355 nm laser pulse. (b) Fluorescence spectra of P3HT and P3HT/acceptor blend films under excitation at 355 nm.

In order to investigate the acceptor function of **Tetra-T-BCN**, **Tetra-TT-BCN**, and **BCN-TT-BCN**, BHJ type photovoltaic devices were fabricated using P3HT as the electron donor, with device structures consisting of glass/indium tin oxide (ITO)/poly(3,4-ethylenedioxythiophene:poly(styrenesulfonate) (PEDOT:PSS)/active layer/ Al. As shown in the external quantum efficiency (EQE) spectra of devices (Figure 1.5 (a)), only **Tetra-TT-BCN** showed photovoltaic current among the acceptors. The result indicates that extended 3-D arrangement of acceptors is favorable for BHJ type OPVs. The PCE of P3HT/**Tetra-TT-BCN** blend is still at a low level due to the energy level mismatch owing to the deep LUMO level of **Tetra-TT-BCN**. Thus, the author evaluated the photovoltaic performance of **Tetra-TT-BCN** as an acceptor with poly[*N*-9"-hepta-decanyl-2,7-carbazole-alt-5,5-(4',7'-di-2-thienyl-2',1',3'-benzothiadiazole) (PCDTBT)[7] as a donor by the device configuration of ITO/MoO_x/PCDTBT:**Tetra-TT-BCN** (1:1)/Al. The active layer was prepared by spin-coating from the blended solution in *o*-dichlorobenzene with a total concentration of 20 mg mL^{-1}. Under illumination of AM 1.5 G solar irradiation (100 mW cm^{-2}), this device showed OPV characteristics with a power conversion efficiency of 0.08%. The current density (*J*)–voltage (*V*) curve of the devices are shown in Figure 1.5 (b). Considering the fact that the BCN-containing planar π-conjugated system did not show any OPV response under the same conditions, we conclude that the extension of the acceptor material to the 3-D structure contributed to the appearance of photovoltaic characteristics in BHJ type OPVs.

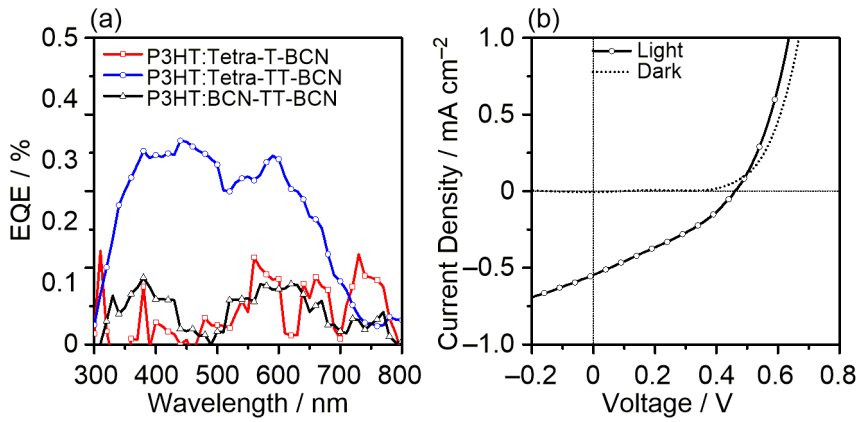

Figure 1.5. (a) EQE spectra of P3HT/**Tetra-T-BCN** (red), P3HT/**Tetra-TT-BCN** (blue), and P3HT/**BCN-TT-BCN** based OPV devices. (b) *J*–*V* curves of PCDTBT/**Tetra-TT-BCN** OPV device.

1.5 Conclusion

In summary, towards the application to acceptor materials in OPVs, new 3-D electron-transporting π-conjugated compounds containing dicyanomethylene-substituted difluorocyclopenta[*b*]thiophene units have been synthesized. The photophysical and electrochemical measurements of these compounds revealed the electronic properties and frontier-orbital energy levels. Despite the unfavorable 3-D structure for the carrier transport in OFETs, both compounds showed electron-transporting characteristics. These compounds were utilized as acceptors along with a low band gap polymer as a donor for the fabrication of BHJ solar cells. As a result, OPV device based on PCDTBT/**Tetra-TT-BCN** showed photovoltaic response. This study demonstrates the effectiveness of 3-D structure to obtain OPV characteristics in non-fullerene acceptor materials.

1.6 Experimental Section

General Information

All reactions were carried out under a nitrogen atmosphere. Solvents of the highest purity grade were used as received. All reagents were purchased from commercial sources and used without purification. Column chromatography was performed on silica gel, KANTO Chemical silica gel 60N (40–50 μm). Thin-layer Chromatography plates were visualized with UV light. Preparative GPC was performed on a Japan Analytical Industry LC-918 equipped with JAI-GEL 1H/2H. ^{1}H and ^{13}C NMR spectra were recorded on a JEOL ECS-400, or Bruker AVANCE III 700 spectrometer in $CDCl_3$ with tetramethylsilane (TMS) as an internal standard. Data are reported as follows: chemical shift in ppm (δ), multiplicity (s = singlet, d = doublet, t = triplet, m = multiplet), coupling constant (Hz), and integration. Mass spectra were obtained on a Shimadzu GCMS-QP-5050 or Shimadzu AXIMA-TOF. UV-vis spectra were recorded on a Shimadzu UV-3600 spectrophotometer. Fluorescence spectra were recorded using a Fluoromax-4 spectrometer in the photo-counting mode equipped with a Hamamatsu R928P photomultiplier. The bandpass for the emission spectra was 1.0 nm. All spectra were obtained in spectrograde solvents. CV was carried out on a BAS CV-620C voltammetric analyzer using a platinum disk as the working electrode, platinum wire as the counter electrode, and $Ag/AgNO_3$ as the reference electrode at a scan rate of 100 mV s^{-1}. Elemental analyses were performed on Perkin Elmer LS-50B by the Elemental Analysis Section of Comprehensive Analysis Center (CAC), ISIR, Osaka University.

OFET Device Fabrication and Evaluation

The field-effect mobility was measured using bottom-contact thin-film FET geometry. The p-doped silicon substrate functions as the gate electrode. A thermally grown silicon oxide dielectric layer on the gate substrate was 300 nm thick with a capacitance of 10.0 nF cm^{-2}. Interdigital source and drain electrodes were constructed with gold (30 nm) that were formed on the SiO_2 layer. The channel width (W) and channel length (L) were 294 mm and 25 μm, respectively. The silicon oxide surface was washed with toluene, acetone, water, and 2-propanol. The silicon oxide surface was then activated by ozone treatment and pretreated with HMDS. The semiconductor layer was spin-casted on the Si/SiO_2 substrate from 1 wt% chloroform solution. The characteristics of the OFET devices were measured at room temperature under a pressure of 10^{-3} Pa. The current-voltage characteristics of devices were measured by using a KEITHLEY 4200SCS semiconductor parameter analyzer. The μ_e was calculated in the saturated region at the V_{DS} of 80 V and the current on/off ratio (I_{on}/I_{off}) was determined from the I_{DS} at V_{GS} = 0 V (I_{off}) and V_{GS} = 80 V (I_{on}) by the following equation.

$$I_{DS} = \frac{W}{2L} C_i \mu (V_{GS} - V_{th})^2$$

FP-TRMC Measurements

A resonant cavity was used to obtain a high degree of sensitivity in the conductivity measurement. The resonant frequency and microwave power were set at ca. 9.1 GHz and 3 mW, respectively, so that the electric field of the microwave was sufficiently small not to disturb the motion of charge carriers. Third harmonic generation (THG; 355 nm) of a Nd:YAG laser (Continuum Inc., Surelite II, 5-8 ns pulse duration, 10 Hz) was used as an excitation

source. The nanosecond laser intensity was set at 4.6×10^{15} photons cm^{-2} $pulse^{-1}$. The samples were drop-casted on a quartz plate from the polymer/acceptor solutions and dried in a vacuum oven. The TRMC experiments were performed in air at room temperature.

OPV Device Fabrication and Evaluation

Organic photovoltaic devices were prepared with a structure of ITO/MoO_x/active layer/Al. ITO-coated glass substrates were first cleaned by ultrasonication in toluene, acetone, H_2O, and 2-propanol for 10 min, respectively. ITO-coated glass substrates were then activated by ozone treatment for 1 h. MoO_x layers were spin-coated from isopropanol solution of bis(2,4-pentanedionato)molybdenum(VI) dioxide on the ITO surface at 2000 rpm for 1 min and dried at ambient temperature for 1 h. The active layers were then prepared by spin-coating on the ITO/MoO_x electrode at 1000 rpm for 2 min in a glove box. The typical thickness of the active layer was 90–110 nm. Al electrode were evaporated on the top of active layer through a shadow mask to define the active area of the devices (0.09 cm^2) under a vacuum of 10^{-5} Pa to a thickness of 100 nm determined by a quartz crystal monitor. After sealing the device from the air, the photovoltaic characteristics were measured in air under simulated AM 1.5G solar irradiation (100 mW cm^{-2}) (SAN-EI ELECTRIC, XES-301S). The *J*−*V* characteristics of photovoltaic devices were measured by using a KEITHLEY 2400 source meter. The EQE spectra were measured by using a Soma Optics Ltd. S-9240. The thickness of active layer was determined by KLA Tencor Alpha-step IQ.

Synthesis

*Synthesis of **2***: **1** (1.00 g, 2.77 mmol), and tetramethylethylenediamine (2.67 g, 23.0 mmol) was placed in a 300 mL two-necked round-bottomed flask and dissolved with THF (140 mL). *n*-BuLi (1.6 M hexane solution, 7.66 mL, 12.3 mmol) was added to the mixture at –78 °C. After stirring for 1 h at –78 °C, tributyltin chloride (5.42 g, 16.7 mmol) was added. The mixture was gradually warmed up to room temperature. After further stirring for 1 h, the reaction was quenched by the addition of water, and the organic layer was separated. The aqueous layer was extracted with hexane, and the combined organic layer was washed with water and dried over Na_2SO_4. After removal of the solvent under reduced pressure, the residue was purified by column chromatography on silica gel (hexane), followed by preparative GPC ($CHCl_3$) to give **2** (2.67 g, 64%). Colorless oil; ^{1}H NMR (400 MHz, $CDCl_3$, TMS): δ 7.58 (d, J = 3.2 Hz, 4H), 7.28 (d, J = 3.2 Hz, 4H), 1.55 (m, 24H), 1.32 (m, 24H), 1.09 (t, J = 8.5 Hz, 24H), 0.88 (t, J = 7.4 Hz, 36H); ^{13}C NMR (100 MHz, $CDCl_3$): δ 144.99, 140.17, 138.75, 136.07, 28.94, 27.22, 13.68, 10.88. This compound was used without further purification.

*Synthesis of **Tetra-T-BCN***: **2** (141 mg, 0.093 mmol), **3** (200 g, 0.45 mmol), $Pd_2(dba)_3 \cdot CHCl_3$ (8 mg, 0.007 mmol), tri-*o*-tolylphosphine (9 mg, 0.03 mmol), and chlorobenzene (6 mL) were placed in a microwave proof walled glass vial equipped with a snap cap. The glass vial was purged with nitrogen, securely sealed, and heated in a microwave reactor, keeping the temperature at 180 °C for 5 min. After removal of the solvent under reduced pressure, the residue was first isolated by column chromatography on silica gel ($CHCl_3$). The fraction containing **Tetra-T-BCN** was further purified by preparative GPC ($CHCl_3$), followed by precipitation using $CHCl_3$ and hexane to give **Tetra-T-BCN** (96 mg, 39%). Red solid; ^{1}H NMR (700 MHz, $CDCl_3$, TMS): δ 7.89 (d, J = 8.4 Hz, 4H), 7.84 (d, J = 8.4

Hz, 2H), 3.29 (t, *J* = 8.2 Hz, 8H), 1.61 (m, 8H), 1.37 (m, 8H), 1.22 (m, 16H), 0.79 (t, *J* = 7.4 Hz, 12H); ^{13}C NMR (176 MHz, $CDCl_3$): δ 151.47, 151.34, 150.12, 150.04, 146.22, 141.16, 141.09, 140.40, 140.35, 138.88, 136.03, 131.99 , 120.18 (t, *J* = 261.4 Hz), 112.11, 111.52, 109.78, 108.79, 31.52, 31.42, 28.63, 28.02, 22.46, 14.06; MS (MALDI-TOF (1,8,9-trihydroxyanthracene matrix)) *m/z* 1824.27 (M–, Calcd 1824.26). Anal. Calcd for $C_{92}H_{60}F_8N_{16}S_8Si$: C, 60.51; H, 3.31; N, 12.27. Found: C, 60.48; H, 3.50; N, 12.08.

*Synthesis of **5***: **4** (2.01 g, 5.72 mmol), 2-(tributylstannyl)thiophene (2.55 g, 6.83 mmol), $Pd_2(dba)_3{\cdot}CHCl_3$ (236 mg, 0.23 mmol), tri-*o*-tolylphosphine (277 mg, 0.91 mmol), and chlorobenzene (10 mL) were placed in a microwave proof walled glass vial equipped with a snap cap. The glass vial was purged with nitrogen, securely sealed, and heated in a microwave reactor, keeping the temperature at 180 °C for 5 min. After removal of the solvent under reduced pressure, the residue was purified by column chromatography on silica gel (hexane/$CHCl_3$ = 2/1) to give **5** (934 mg, 92%). Yellow solid; ^{1}H NMR (400 MHz, $CDCl_3$, TMS): δ 7.62 (dd, *J* = 5.0, 0.9 Hz, 1H), 7.43 (dd, *J* = 3.7, 0.9 Hz, 1H), 7.21 (dd, *J* = 5.0, 3.7 Hz, 1H), 3.07 (t, *J* = 8.2 Hz, 2H), 1.66 (m, 2H), 1.43 (m, 2H), 1.32 (m, 4H), 0.89 (t, *J* = 7.3 Hz, 3H); ^{13}C NMR (100 MHz, $CDCl_3$): δ 180.26 (t, *J* = 24.8 Hz), 177.46 (t, *J* = 24.8 Hz), 153.52, 151.64, 150.13, 136.55, 132.46, 130.13, 129.58, 128.50, 106.99 (t, *J* = 266.7 Hz), 31.34, 30.05, 29.15, 27.36, 22.53, 14.04; MS (EI) *m/z* 354 (M+, Calcd 354); Anal. Calcd for $C_{17}H_{16}F_2O_2S_2$: C, 57.61; H, 4.55. Found: C, 57.42; H, 4.75.

*Synthesis of **6***: **5** (934 mg, 2.64 mmol) was placed in a 50 mL round-bottomed flask and dissolved in DMF (26 mL) and *N*-bromosuccinimide (609 mg, 3.42 mmol) was added to the mixture. After stirring for 20 h at 70 °C, the reaction was quenched by the addition of 2 M aqueous $Na_2S_2O_3$. The aqueous layer was extracted with EtOAc, and the combined organic layer was washed with water and dried over Na_2SO_4. After removal of the solvent under reduced pressure, the residue was purified by column chromatography on silica gel (hexane/$CHCl_3$ = 1/1) to give **6** (1.07 g, 94%). Orange solid; ^{1}H NMR (400 MHz, $CDCl_3$, TMS): δ 7.07 (s, 2H), 3.02 (t, *J* = 8.2 Hz, 2H), 1.64 (m, 2H), 1.43 (m, 2H), 1.34–1.30 (m, 4H), 0.90 (t, *J* = 8.0 Hz, 3H); ^{13}C NMR (100 MHz, $CDCl_3$): δ 180.11 (t, *J* = 25.2 Hz), 177.46 (t, *J* = 25.6 Hz), 153.36, 150.30, 150.08, 136.99, 133.74, 131.27, 129.74, 117.68, 106.88 (t, *J* = 263.4 Hz), 31.33, 30.12, 29.13, 27.39, 22.52, 14.04; MS (EI) *m/z* 432 (M–, Calcd 432); Anal. Calcd for $C_{17}H_{15}BrF_2O_2S_2$: C, 47.12; H, 3.49. Found: C, 47.26; H, 3.72.

*Synthesis of **7***: **6** (1.07 g, 2.47 mmol) was placed in a 100 mL two-necked flask and dissolved with $CHCl_3$ (40 mL). To the mixture were added malononitrile (491 mg, 7.43 mmol), $TiCl_4$ (2.35 g, 12.4 mmol), and pyridine (2 mL), and the mixture was stirred at 60 °C for 4 h. The reaction was quenched by addition of water, and the organic layer was separated. The aqueous layer was washed with $CHCl_3$, and the combined organic layer was washed with water and dried over Na_2SO_4. After removal of the solvent under reduced pressure, the residue was purified by column chromatography on silica gel ($CHCl_3$) to give **7** (1.16 g, 89%). Red solid; ^{1}H NMR (400 MHz, $CDCl_3$, TMS): δ 7.22 (s, 1H), 7.22 (s, 1H), 3.25 (t, *J* = 8.4 Hz, 2H), 1.56 (m, 2H), 1.43 (m, 2H), 1.29 (m, 4H), 0.88 (t, *J* = 6.9 Hz, 3H); ^{13}C NMR (100 MHz, $CDCl_3$): δ 156.22, 151.43, 150.88, 147.24, 146.86, 145.01, 134.68, 129.01 (t, *J* = 305.01 Hz), 128.60, 121.18, 120.02, 118.77, 118.57, 111.85, 110.92, 109.09, 108.66, 31.49, 30.27, 30.15, 29.08, 22.49, 14.02; MS (EI) *m/z* 528 (M+, Calcd 528); Anal. Calcd for $C_{23}H_{15}BrF_2N_4S_2$: C, 52.18; H, 2.86; N, 10.58. Found: C, 51.99;

H, 3.08; N, 10.62.

Synthesis of ***Tetra-TT-BCN***: **2** (624 mg, 0.41 mmol), **7** (1.05 g, 1.97 mmol), $Pd_2(dba)_3{\cdot}CHCl_3$ (36 mg, 0.035 mmol), tri-*o*-tolylphosphine (40 mg, 0.13 mmol), and chlorobenzene (12.7 mL) were placed in a microwave proof walled glass vial equipped with a snap cap. The glass vial was purged with nitrogen, securely sealed, and heated in a microwave reactor, keeping the temperature at 180 °C for 5 min. After removal of the solvent under reduced pressure, the residue was first isolated by column chromatography on silica gel ($CHCl_3$). The fraction containing **Tetra-TT-BCN** was further purified by preparative GPC ($CHCl_3$), followed by precipitation using $CHCl_3$ and methanol to give **Tetra-TT-BCN** (385 mg, 43%). Black solid; ^{1}H NMR (400 MHz, $CDCl_3$, TMS): δ 7.55 (d, J = 3.7 Hz, 4H), 7.49 (d, J = 3.7 Hz, 4H), 7.42 (d, J = 3.8 Hz, 4H), 7.38 (d, J = 3.8 Hz, 4H), 3.33 (t, J = 7.8 Hz, 8H), 1.63 (m, 8H), 1.45 (m, 8H), 1.32-1.27 (m, 16H), 1.32-1.27 (t, J = 7.3 Hz, 12H); ^{13}C NMR (100 MHz, $CDCl_3$): δ 152.04, 151.39, 151.18, 149.61, 149.37, 146.49, 145.43, 143.73, 142.55, 140.01, 137.54, 133.14, 131.87, 131.41, 127.12, 125.97, 120.36 (t, J = 266.9 Hz), 112.23, 111.75, 110.00, 109.18, 31.47, 31.39, 28.66, 28.07, 22.45, 14.02; MS (MALDI-TOF (1,8,9-trihydroxyanthracene matrix)) *m/z* 2152.21 (M–, Calcd 2152.21); Anal. Calcd for $C_{108}H_{68}F_8N_{16}S_{12}Si$: C, 60.20; H, 3.18; N, 10.40. Found: C, 59.98; H, 3.43; N, 10.16.

1.7 References

1 Y. Lin, P. Cheng, Y. Li and X. Zhan, *Chem. Commun.*, 2012, **48**, 4773; Y. Ie, T. Sakurai, S. Jinnai, M. Karakawa, K. Okuda, S. Mori and Y. Aso, *Chem. Commun.*, 2013, **49**, 8386.

2 X. Zhang, C. Zhan and J. Yao, *Chem. Mater.*, 2015, **27**, 166; Y. Liu, C. Mu, K. Jiang, J. Zhao, Y. Li, L. Zhang, Z. Li, J. Y. L. Lai, H. Hu, T. Ma, R. Hu, D. Yu, X. Huang, B. Tang and H. Yan, *Adv. Mater.*, 2015, **27**, 1015; Y. Liu, J. Y. L. Lai, S. Chen, Y. Li, K. Jiang, J. Zhao, Z. Li, H. Hu, T. Ma, H. Lin, J. Liu, J. Zhang, F. Huang, D. Yu and H. Yan, *J. Mater. Chem. A*, 2015, **3**, 13632; J. Zhao, Y. Li, H. Lin, Y. Liu, K. Jiang, C. Mu, T. Ma, L. Lai, H. Hu, D. Yu and H. Yan, *Energy Environ. Sci.*, 2015, **8**, 520.

3 Y. Ie, K. Nishida, M. Karakawa, H. Tada, A. Asano, A. Saeki, S. Seki and Y. Aso, *Chem. Eur. J.*, 2011, **17**, 4750; Y. Ie, K. Nishida, M. Karakawa, H. Tada and Y. Aso, *J. Org. Chem.*, 2011, **76**, 6604.

4 J. Nakayama and J.-S. Lin, *Tetrahedorn. Lett.*, 1997, **38**, 6043.

5 A. J. Bard and L. R. Faulkner, *Electrochemical Methods–Fundamentals and Applications*: Wiley: New York, (1984); J. Pommerehne, H. Vestweber, W. Guss, R. F. Mahrt, H. Bässler, M. Porsch and J. Daub, *Adv. Mater.*, 1995, **7**, 551.

6 A. Saeki, Y. Koizumi, T. Aida and S. Seki, *Acc. Chem. Res.*, 2012, **45**, 1193.

7 S. H. Park, A. Roy, S. Beaupré, S. Cho, N. Coates, J. S. Moon, D. Moses, M. Leclerc, K. Lee and A. J. Heeger, *Nat. Photonics*, 2009, **3**, 297.

Chapter 2
Linearly Extended Acceptor Materials End-Capped with Solubilized Phthalimide and Phthaldithioimide Derivatives.

2.1 Introduction

From the results of chapter 1, 3-D arranged acceptor materials were demonstrated to be favorable as acceptor materials compared to planar π-conjugated systems. However the PCEs of devices were at the still low level. Toward the further evaluation of chemical structure−properties−OPV performances relationship, high-performance acceptor materials various structures can be realized with are considered to be essential. On these background, in this chapter, the author focused on the utilization of solubilized phthalimide derivatives.

Electron-withdrawing cyclic imide groups are the most commonly inserted into π-conjugated systems to apply to electron accepting materials.[1] Cyclic imide are prepared by one step condensation reaction of cyclic dicarboxyanhydride with primary amines (Figure 2.1). By utilizing this synthetic methodology, the author aimed to make it easy to compare the acceptor properties and performances by use of cyclic imide derivatives. In addition, the oxygen atoms of cyclic imide derivatives can be substituted to sulfur atoms by treating with Lawesson's reagent or Davy's reagent. As shown in the results of DFT calculation at the B3LYP/6-31G(d,p) level (Figure 2.2), the thiocarbonyl groups of S-Imi(Me) more strongly participate in the LUMO than the carbonyl groups of Imi(Me), and as a consequence, S-Imi(Me) possesses a notably lower LUMO energy level than Imi(Me). Furthermore, from large coefficients on the sulfur atoms in the dithioimides, it can be expected to increase the intermolecular overlap of LUMOs in the solid state, as for the case that the sulfur atoms with large coefficients of the HOMO in thienoacene derivatives contribute intermolecular HOMO overlap. As a consequence of these reaction, diverse acceptor materials with different physical properties are derivable from cyclic imide systems. Based on this view point, the author designed new phthalimide based acceptors (**Imi-a-BT**, **Imi-T-BT**, and **Imi-TzTz**) and phthaldithioimide based acceptors (**S-Imi-a-BT**, **S-Imi-T-BT**, and **S-Imi-TzTz**). Furthermore, not only thermophysical, photophysical and Electrochemical Properties, but also OFETs and OPVs performances of these compounds were investigated. From these systematical analysis on this chapter, the author attempted to extract the physical properties that can be responsible for the OPV performances.

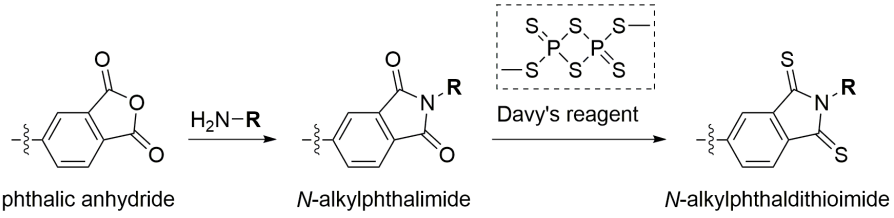

Figure 2.1. Synthetic scheme of phthalimide and phthaldithioimide derivatives.

2.2 Synthesis

The synthetic routes of target compounds are shown in Scheme 2.1. First, we planned to use dithioimide compound **9** as a starting unit for **S-Imi-a-BT**. However, all attempts of Pd-catalyzed cross-coupling reactions using **9** as a substrate resulted in complex mixtures owing to the catalytic poison of the thioimide group. To

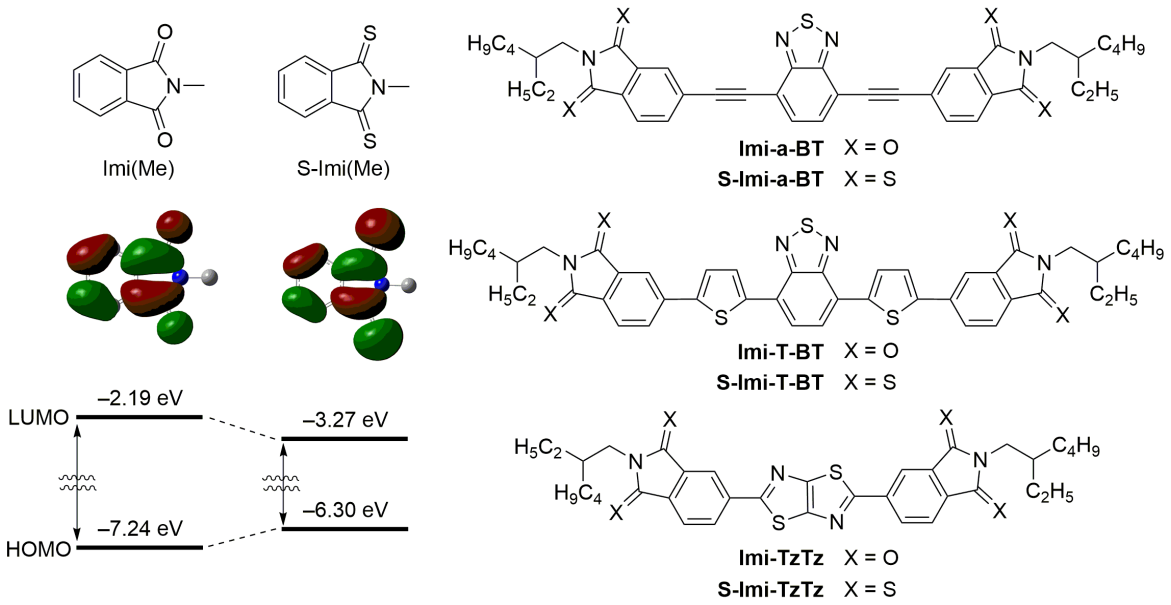

Figure 2.2. HOMO and LUMO energies calculated with DFT at the B3LYP/6-31G(d,p) level and chemical structures used in this study.

overcome this problem, we decided to apply thionation after constructing the π-conjugated framework. Thus, Pd-catalyzed Sonogashira-Hagihara coupling of **8** with diethynyl compound **10**[2] in THF/NEt(*i*-Pr)$_2$ gave **Imi-a-BT**, which was then thionated with Davy's reagent to form **S-Imi-a-BT** in 88% yield. **Imi-T-BT** was obtained by Stille coupling of **8** with dithienyl compound **11**,[3] which was also then treated with Davy's reagent to form **S-Imi-T-BT** in 62% yield. Since the thiazolothiazole (TzTz) structure can be synthesized by the condensation reaction of aldehyde with ethanedithioamide, we established the synthetic route of key aldehyde unit **14** from commercially available 4-methylphthalic anhydride. After completing the synthesis of **Imi-TzTz**, subsequent transformation with Davy's reagent gave **S-Imi-TzTz** in 88% yield. Due to the presence of branched alkyl chains, these compounds are soluble in common organic solvents such as chloroform, chlorobenzene, and *o*-dichlorobenzene. However, the solubilities of the dithioimide compounds are considerably lower than those of the imide compounds.

2.3 Thermophysical, Photophysical and Electrochemical Properties

The thermal properties of the synthesized compounds were investigated by differential scanning calorimetry (DSC). As shown in Figure 2.3, **S-Imi-a-BT** and **S-Imi-T-BT** showed no obvious peaks up to 300 ˚C on a heating run, whereas the trace of **Imi-a-BT** and **Imi-T-BT** showed clear melting peaks at 223 and 227 ˚C, respectively. Compared to **Imi-TzTz**, the peak of crystallization for **S-Imi-TzTz** is more separated from the melting peak and more broadened. These results indicate a weak crystallization nature of the dithioimide compounds. On the other hand, the higher melting temperature of **S-Imi-TzTz** compared to that of **Imi-TzTz** is likely the result of strong intermolecular interactions, which is consistent with a presumption from the low solubility of the dithioimide compounds (*vide supra*).

The UV-vis absorption spectra of the new π-conjugated compounds were measured in a chloroform solution and as a film on a quartz plate, and the photophysical data are summarized in Table 2.1. As shown in Fig. 2, the

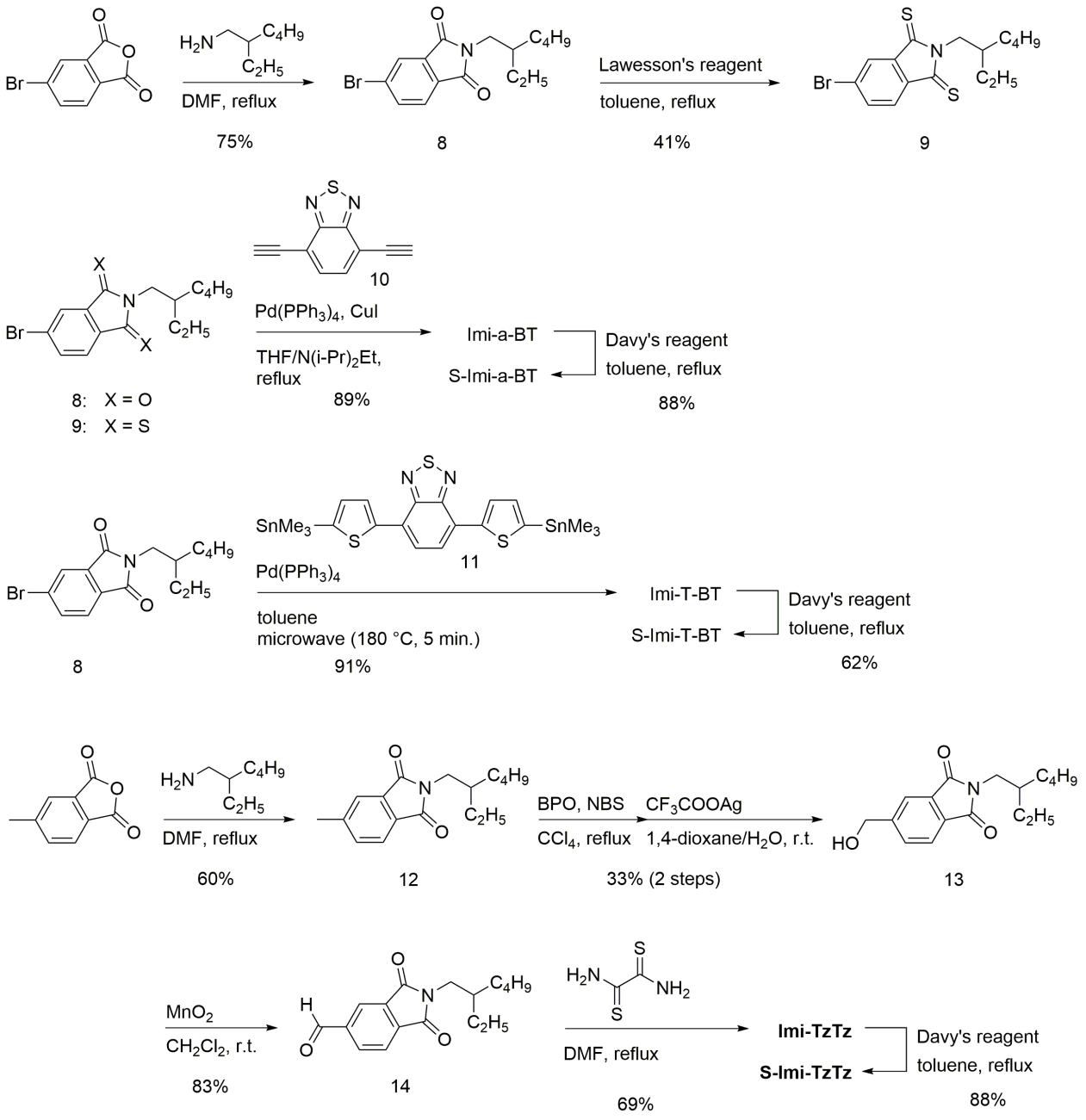

Scheme 2.1. Synthesis of target compounds.

absorption spectra of the phthaldithioimide compounds in solution exhibit two obvious absorption bands in visible region, while the phthalimide compounds exhibit one absorption band. According to time-dependent DFT calculations of the dithioimide compounds at the Coulomb attenuated method (CAM) corrected B3LYP/6-31G(d,p) level, the band at longer wavelength is mainly ascribable to the transition between HOMO and LUMO. Thus, the measured spectra indicate that the HOMO–LUMO gaps of the dithioimide compounds are narrower than those of the imide compounds. Compared to the spectra of the imide compounds in solution, an additional well-structured shoulder appeared in their absorption spectra in the solid state, which is attributed to intermolecular electronic interactions of π–π stacked backbones. In contrast, the absorption spectra of the dithioimide compounds in the solid

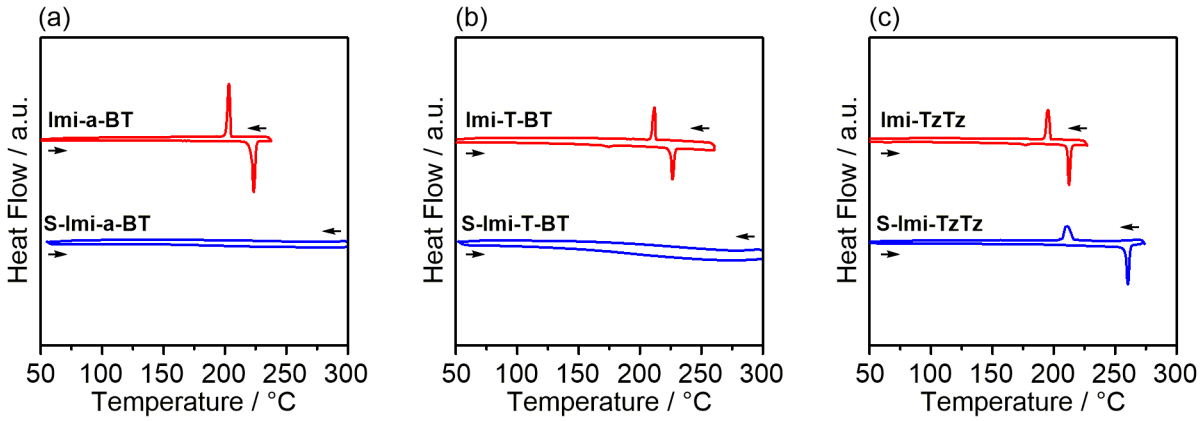

Figure 2.3. DSC profiles of (a) **Imi-a-BT** and **S-Imi-a-BT**, (b) **Imi-T-BT** and **S-Imi-T-BT**, and (c) **Imi-TzTz** and **S-Imi-TzTz** with a heating rate of 10 °C min^{-1} in N_2.

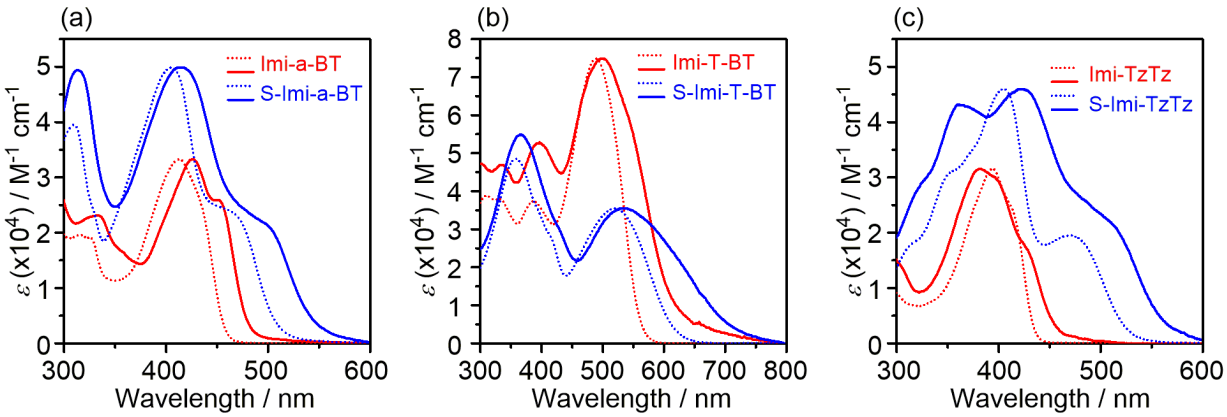

Figure 2.4. UV-vis absorption spectra of (a) **Imi-a-BT** and **S-Imi-a-BT**, (b) **Imi-T-BT** and **S-Imi-T-BT**, (c) **Imi-TzTz** and **S-Imi-TzTz**, in $CHCl_3$ (dashed line) and film (solid line).

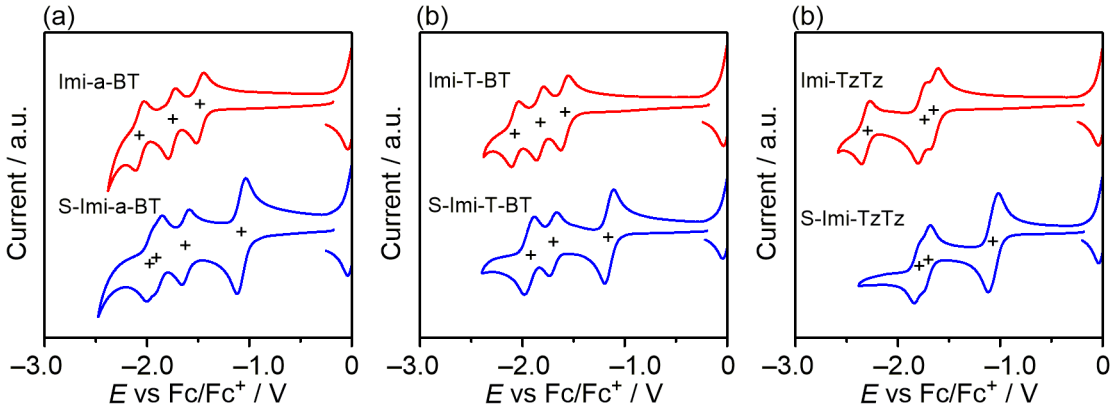

Figure 2.5. Cyclic voltammograms of (a) **Imi-a-BT** (red) and **S-Imi-a-BT** (blue), (b) **Imi-T-BT** (red) and **S-Imi-T-BT** (blue) (c) **Imi-TzTz** (red) and **S-Imi-TzTz** (blue) in *o*-dichlorobenzene/acetonitrile containing 0.1 M $TBAPF_6$.

state were markedly red-shifted with a concomitant of broadening compared to those in a solution state, which are also an indication of strong intermolecular electronic interactions. These results imply that the replacement of the

Table 2.1. Properties of compounds

Compounds	λ_{max} [nm][a]	ΔE_{opt} [eV][b]	$E_{red}^{1/2}$ [V][c]	E_{LUMO} [eV][d]	E_{HOMO} [eV][e]
Imi-a-BT	412	2.70	–1.48, –1.75, –2.07	–3.32	–6.02
S-Imi-a-BT	405, 463	2.24	–1.08, –1.62, –1.88, –1.96	–3.72	–5.96
Imi-T-BT	488	2.20	–1.59, –1.83, –2.07	–3.21	–5.41
S-Imi-T-BT	357, 520	2.00	–1.15, –1.70, –1.94	–3.65	–5.65
Imi-TzTz	394	2.72	–1.65, –1.77, –2.31	–3.15	–5.86
S-Imi-TzTz	405, 473	2.20	–1.07, –1.77, –1.81	–3.73	–5.93

[a] In $CHCl_3$. [b] Determined by the onset of the UV-Vis absorption spectrum in $CHCl_3$. [c] In *o*-DCB/acetonitrile (5/1), 0.1 M $TBAPF_6$, V vs. Fc/Fc^+. [d] Estimated from the approximation that the Fc/Fc^+ level is –4.8 eV vs. vacuum. [e] Determined by E_{LUMO} and ΔE_{opt}.

imide oxygen to sulfur in π-conjugated systems induces the appearance of different organizations and/or intermolecular interactions in the solid state. From the onset of the absorption in the film state, the optical HOMO–LUMO energy gaps (ΔE_{opt}) of **S-Imi-a-BT**, **S-Imi-T-BT**, and **S-Imi-TzTz** were estimated to be 2.24, 2.00, and 2.20 eV, respectively, whose values are noticeably reduced compared with those similarly estimated for the imide compounds (**Imi-a-BT** : 2.58 eV, **Imi-T-BT** : 2.20 eV, and **Imi-TzTz** : 2.72 eV).

To investigate the electrochemical properties of the imide and dithioimide compounds, CV were employed. Figure 2.5 depict the cyclic voltammograms of these compounds, and the electrochemical data extracted from the cyclic voltammograms are listed in Table 2.1. All the compounds showed reversible reduction waves, since the presence of electron-accepting terminal units in the π-system contributes to both decreasing the LUMO energy level and increasing the thermodynamic stability of the resulting anionic species. Interestingly, replacing the imide group with thioimide group dramatically changed not only the above-mentioned photophysical properties but also electrochemical properties of the π-systems. It is notable that the first half-wave potentials ($E_{red1/2}$) of the

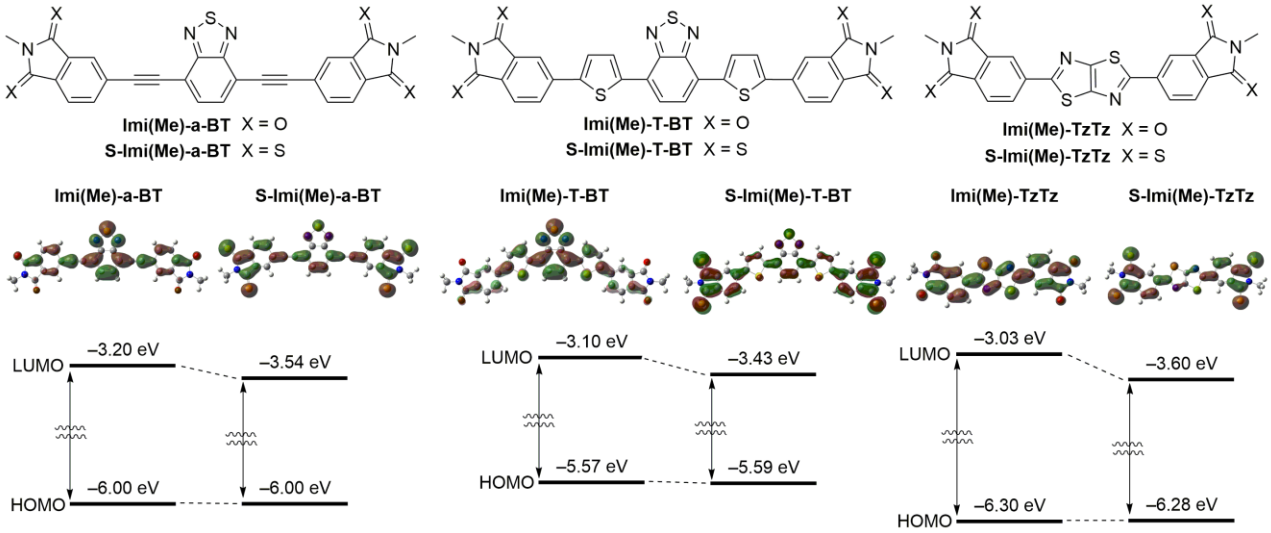

Figure 2.6. HOMO, LUMO, and LUMO+1 energies calculated with DFT at the B3LYP/6-31G(d,p) level and LUMO orbitals. 2-Ethylhexyl groups were replaced with methyl groups to ease the calculation.

dithioimide compounds are positively shifted compared to those of the imide compounds. This can be explained by the fact that the introduction of strong electron-withdrawing dithioimide units contributes to increase the electron-accepting nature of π-system. Moreover, the dithiothienoimide unit has more electron-accepting characteristics than the dithiophthalimide unit as predicted by the theoretical calculations (Figure. 2.6). As listed in Table 1, the LUMO energy levels for the dithioimide and imide compounds were estimated from their first-$E_{red1/2}$ values relative to Fc/Fc^+ under the assumption that the energy level of Fc/Fc^+ is –4.8 eV below the vacuum level.[4] The HOMO energy levels of these compounds were estimated by their LUMO energy levels and ΔE_{opt} (Table 2.1). The obtained values indicate that the HOMO energy levels of the dithioimide compounds are slightly lower or the same level compared to that of the corresponding imide compound. These estimated LUMO and HOMO energy levels are in good agreement with the theoretical results (Figure. 2.6).

2.4 Electron Mobility

To investigate the influence of above-mentioned properties on the charge-transport properties, OFETs with a bottom-contact and bottom-gate configuration were fabricated using the respective dithioimide and imide compounds as the semiconductors. The active layers were formed by drop-casting from a chlorobenzene solution on the octadecyltrichlorosilane (ODTS)-modified SiO_2 dielectric at solvent-evaporation temperature of 90 °C and subsequent annealing at 160 °C in a vacuum. As the results, all the compounds exhibited typical n-type OFET responses, as expected from the estimation of the low-lying LUMO energy levels. It should be mentioned that the μ_es of the dithioimide compounds were found to increase by two orders of magnitude or more, compared to those of the imide compounds, and the highest μ_e of 1.1×10^{-2} cm^2 V^{-1} s^{-1} was obtained for the device using **S-Imide-TzTz**.

Since the charge-transport characteristics in OFETs are known to be strongly dependent on the structural order of molecules in the solid state, X-ray diffraction (XRD) of these thin films were investigated. As shown in Figure 2.7, the imide compounds exhibited clear reflections, indicating the formation of a crystalline ordered structure. On the other hand, surprisingly, the XRD scans of the dithioimide compounds did not show any reflections, indicating that these films take the amorphous nature. This film behavior of the dithioimide compounds is generally considered as a disadvantageous orientation for charge transport in the OFET geometry.[5] We tentatively explained this unexpected phenomenon as follows: the presence of strong intermolecular electronic interactions for the dithioimide compounds, which was implied by the UV–vis measurements in the solid state, induces the construction of non-

Table 2.2. OFET characteristics of compounds

Compounds	μ_e [cm^2 V^{-1} s^{-1}]	I_{on}/I_{off}	V_{th} [V]
Imi-a-BT	5.4×10^{-6}	10^3	70
S-Imi-a-BT	1.4×10^{-4}	10^6	69
Imi-T-BT	1.2×10^{-5}	10^3	33
S-Imi-T-BT	1.3×10^{-3}	10^3	7
Imi-TzTz	4.0×10^{-6}	10^2	85
S-Imi-TzTz	1.1×10^{-2}	10^8	29

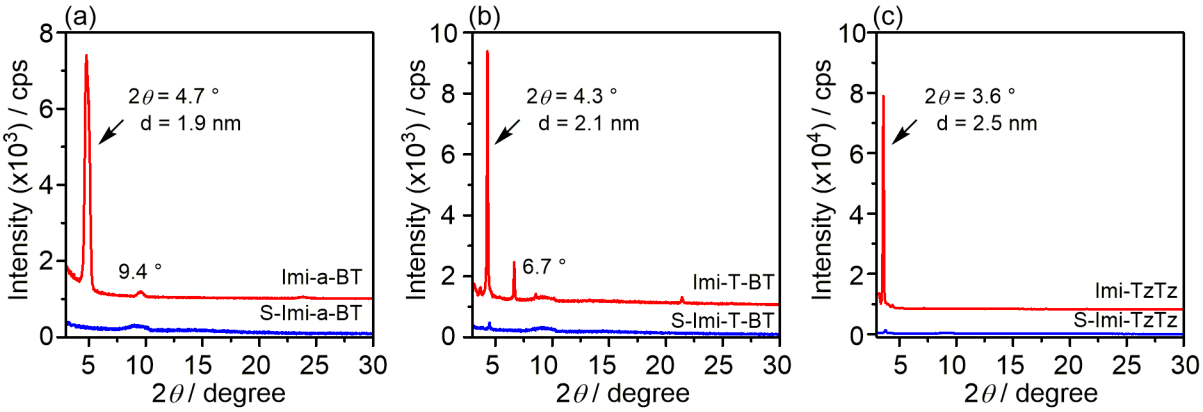

Figure 2.7. XRD profiles of (a) **Imi-a-BT** (red) and **S-Imi-a-BT** (blue), (b) **Imi-T-BT** (red) and **S-Imi-T-BT** (blue) (c) **Imi-TzTz** (red) and **S-Imi-TzTz** (blue)-based films coated on ODTS-modified SiO_2.

directional charge-transport pathways that can compensate low-crystallinity-derived deformation from desirable molecular alignment. Therefore, the high electron mobilities of the thioimide compounds might be ascribable to the combination of both low-lying LUMO energy level in molecular properties and strong intermolecular electronic interactions in the solid state.

2.5 Photovoltaic Performances and Thin-film Properties

To investigate the photovoltaic performance of new acceptor materials, BHJ type OPV devices were fabricated using P3HT as the electron donor, with device structures consisting of glass/ITO/PEDOT:PSS/active layer/Ca/Al. The fabrication conditions of the active BHJ layer were optimized by varying the blend composition, processing solvent, and thermal annealing temperature, and the *J*–*V* characteristics and the corresponding parameters were shown in Figure 2.8 (a) and Table 2.3. While the device based on **Imi-a-BT** showed moderate OPV performances with PCE of 1.58%, contrary to our expectations, the dithioimide compounds showed poor PCEs. To gain insight into this unexpected result, we compared the photo luminescence (PL) spectra and atomic-force microscopy (AFM) image of the P3HT/acceptor blend films (Figure 2.8 (b) and Figure 2.9). The PL spectra of each the films showed

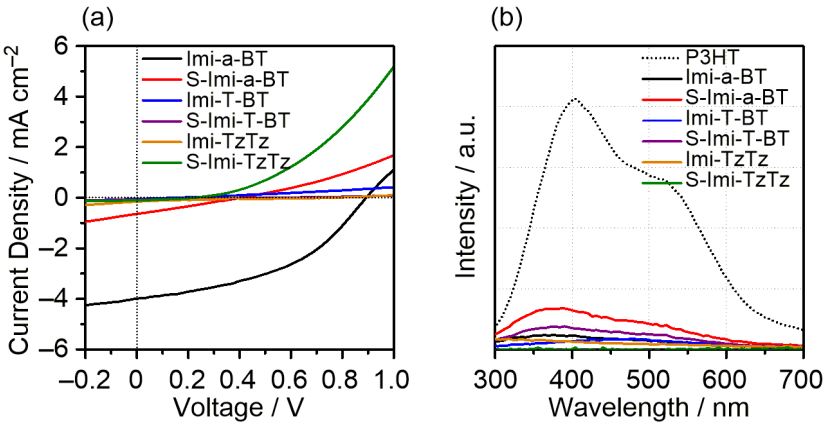

Figure 2.8. (a) *J*–*V* curves of the OPV devices. (b) Fluorescence spectra of P3HT film and P3HT/acceptor blended films excited at absorption maximum.

Table 3.2. OPV characteristics and SFEs of acceptors.

Compounds	J_{SC} [mA cm^{-2}]	V_{OC} [V]	FF	PCE [%]	γ^d [mJ m^{-2}]	γ^p [mJ m^{-2}]	SFE [mJ m^{-2}]
Imi-a-BT	3.99	0.89	0.45	1.58	26.1	0.0	26.1
S-Imi-a-BT	0.64	0.41	0.26	0.07	8.2	4.9	11.1
Imi-T-BT	0.53	0.78	0.24	0.10	8.1	11.1	19.2
S-Imi-T-BT	0.87	0.55	0.24	0.11	9.4	6.6	16.0
Imi-TzTz	0.15	0.75	0.19	0.02	0.1	21.1	21.2
S-Imi-TzTz	0.10	0.23	0.35	0.01	6.0	13.4	19.4
$PC_{61}BM$					27.6	6.1	33.7

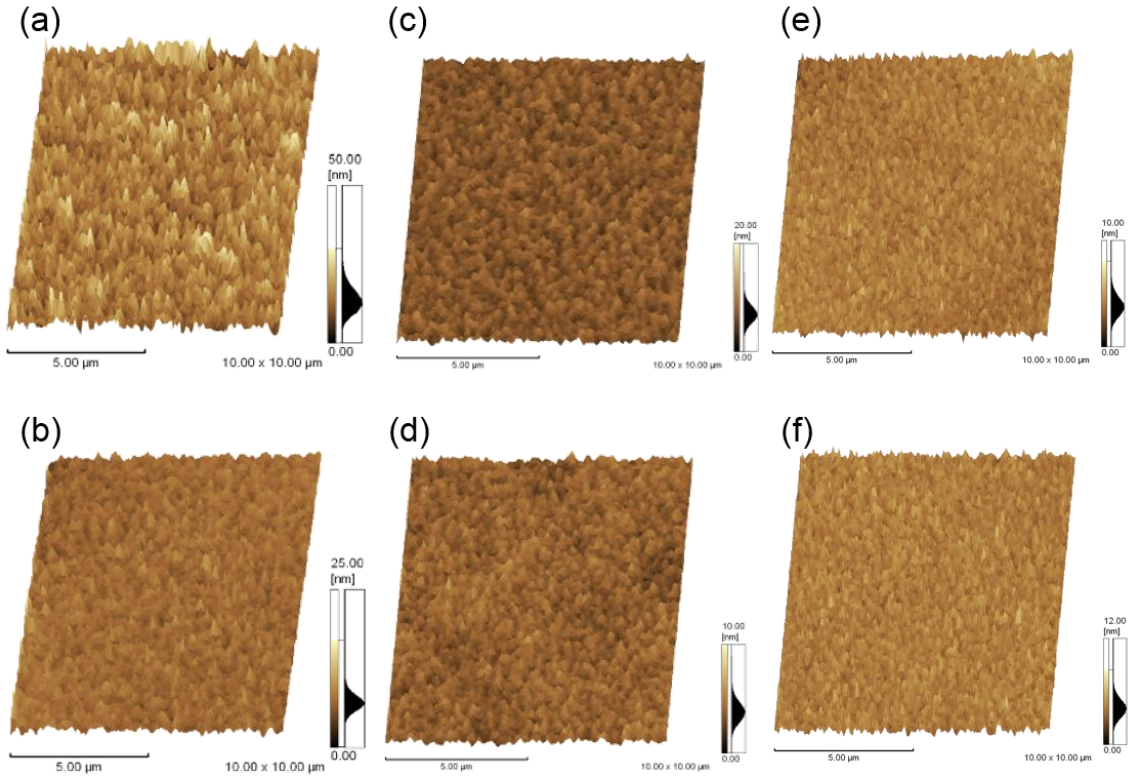

Figure 2.9. AFM images of (a) P3HT/**Imi-a-BT**, (b) P3HT/**S-Imi-a-BT**,(c) P3HT/**Imi-T-BT**, (d) P3HT/**S-Imi-T-BT**, (e) P3HT/**Imi-TzTz**, and (f) P3HT/**S-Imi-TzTz**-based active layers of OPV devices.

effective quenching of the fluorescence from P3HT, implying that photoinduced charge separation between P3HT and the acceptor materials takes place effectively. On the other hand, the AFM

To further elucidate the relationship between photovoltaic characteristics and thin-film properties, the surface free energies (SFEs) of acceptor films were estimated from their contact-angle measurements. It appears that **Imi-a-BT** (26.1 mJ m^{-2}) indicated the largest SFE values, originated from its high London dispersion component (γ^d), among the new acceptors. Under the same conditions, the SFE and γ^d values of $PC_{61}BM$ were estimated to be 33.7, and 27.6 mJ m^{-2}, respectively.[6,7] These results imply that a larger SFE (and/or γ^d) might have promoted to form desirable interace in active layers.

2.6 Conclusion

In summary, a new family of π-conjugated system, whose structures was incorporated with phthalimides and phthaldithioimides as electron-accepting terminal units, were designed and successfully synthesized. The utilization of thionation to the imide compounds in the final step of the synthesis enabled us to complete the construction of dithioimide-containing π-systems. The thermal, photophysical, and electrochemical properties of the dithioimide compounds were significantly different from those of the imide compounds, clearly demonstrating the uniqueness of the dithioimide as a new electron-accepting unit. The author also noticed that the OFET performances of the dithioimide compounds were dramatically improved, despite of their tendency to form amorphous films, compared to those for the crystalline films of the corresponding imide derivatives. This trend is apparently opposite to the conventional understanding that the crystalline state of the active layer in thin films is essential to obtaining high OFET characteristics. Among the new acceptors, imide-based **Imi-a-BT** showed a moderate PCEs in spite of its shallow LUMO energy level and small μ_e compared to those of **S-Imi-a-BT**. As a results of thin-film analysis, P3HT/**Imi-a-BT** blended films indicated the formation of nanometer-scale grain structure. Furthermore, relatively high SFE and γ^d values were indicated with not only **Imi-a-BT** but also $PC_{61}BM$ from the contact angle measurements. Detailed relationship between SFE (and/or γ^d) values and OPV performances was studied in the following chapter.

2.7 Experimental Section

General Information

Column chromatography was performed on silica gel, KANTO Chemical silica gel 60N (40–50 μm). Thin-layer Chromatography plates were visualized with UV light. GPC was performed on a Japan Analytical Industry LC-918 equipped with JAI-GEL 1H/2H. Melting points are uncorrected. ^1H and ^{13}C NMR spectra were recorded on a JEOL ECS-400 spectrometer in $CDCl_3$ or $CDCl_3/CS_2$ with TMS as an internal standard. Data are reported as follows: chemical shift in ppm (δ), multiplicity (s = singlet, d = doublet, t = triplet, m = multiplet, br = broad), coupling constant (Hz), and integration. Mass spectra were obtained on a Shimadzu GCMS-QP-5050 or Shimadzu AXIMA-TOF. DSC and TGA were performed under nitrogen at a heating rate of 10 °C min^{-1} with a Shimadzu DSC-60 and a Shimadzu TGA-50, respectively. UV-vis-NIR spectra were recorded on a Shimadzu UV-3600 spectrophotometer. Fluorescence spectra were recorded using a Fluoromax-2 spectrometer in the photo-counting mode equipped with a Hamamatsu R928 photomultiplier. The bandpass for the emission spectra was 1.0 nm. All spectra were obtained in spectrograde solvents. CV was carried out on a BAS CV-620C voltammetric analyzer using a platinum disk as the working electrode, platinum wire as the counter electrode, and $Ag/AgNO_3$ as the reference electrode at a scan rate of 100 mV s^{-1}. Photoemission yield spectroscopy was carried out using a Riken Keiki Co. Ltd. AC-3 with a light intensity of 10 mW. Elemental analyses were performed on Perkin Elmer LS-50B by the Elemental Analysis Section of CAC, ISIR, Osaka University. The surface structures of the deposited organic film were observed by atomic force microscopy (Shimadzu, SPM9600), and the film crystallinity was evaluated by an X-ray diffractometer (Rigaku, SmartLab). X-ray diffraction patterns were obtained using Bragg-Brentano geometry with CuKα radiation as an X-ray source with an acceleration voltage of 45 kV and a beam current of 200 mA. The scanning mode was set to 2θ scans between 3°–30° with scanning steps of 0.01°.

OFET Device Fabrication and Evaluation

The field-effect mobility was measured using bottom-contact thin-film FET geometry. The p-doped silicon substrate functions as the gate electrode. A thermally grown silicon oxide dielectric layer on the gate substrate was 300 nm thick with a capacitance of 10.0 nF cm^{-2}. Interdigital source and drain electrodes were constructed with gold (30 nm) that were formed on the SiO_2 layer. The W and L were 294 mm and 25 μm, respectively. The silicon oxide surface was washed with toluene, acetone, water, and 2-propanol. The silicon oxide surface was then activated by ozone treatment and pretreated with ODTS. The semiconductor layer was drop-casted on the Si/SiO_2 substrate from 10 mg/mL chlorobenzene solution. The characteristics of the OFET devices were measured at room temperature under a pressure of 10^{-3} Pa. The current-voltage characteristics of devices were measured by using a KEITHLEY 4200SCS semiconductor parameter analyzer. The μ_e was calculated in the saturated region at the V_{DS} of 100 V and the current I_{on}/I_{off} was determined from the I_{DS} at V_{GS} = –20 V (I_{off}) and V_{GS} = 100 V (I_{on}) by the following equation.

$$I_{DS} = \frac{W}{2L} C_i \mu (V_{GS} - V_{th})^2$$

OPV Device Fabrication and Evaluation

Organic photovoltaic devices were prepared with a structure of ITO/PEDOT:PSS/active layer/Ca/Al. ITO-coated glass substrates were first cleaned by ultrasonication in toluene, acetone, H_2O, and 2-propanol for 10 min, respectively, followed by O_2 plasma treatment for 10 min. ITO-coated glass substrates were then activated by ozone treatment for 1 h. PEDOT:PSS was spin-coated on the ITO surface at 3000 rpm for 1 min and dried at 135 °C for 10 min. The active layers were then prepared by spin-coating on the ITO/PEDOT:PSS electrode at 1000 rpm for 2 min in a glove box. The typical thickness of the active layer was 90–110 nm. Ca and Al electrode were evaporated on the top of active layer through a shadow mask to define the active area of the devices (0.09 cm^2) under a vacuum of 10^{-5} Pa to a thickness of 30, 100 nm determined by a quartz crystal monitor. After sealing the device from the air, the photovoltaic characteristics were measured in air under simulated AM 1.5G solar irradiation (100 mW cm^{-2}) (SAN-EI ELECTRIC, XES-301S). The current-voltage characteristics of photovoltaic devices were measured by using a KEITHLEY 2400 source meter. The EQE spectra were measured by using a Soma Optics Ltd. S-9240. The thickness of active layer was determined by KLA Tencor Alpha-step IQ.

Surface Free Energy Estimation

The contact angles of compounds were measured by a NiCK LSE-ME1 with distilled water and glycerol. The surface free energy was estimated based on the established theory.[3,4]

Computational Details

All calculations were conducted using Gaussian 09 program. The geometry was optimized with the restricted Becke Hybrid (B3LYP) at 6-31 G(d, p) level. TD-DFT calculation was performed at the B3LYP/6-31G(d,p) level.

The calculated excited state of **Imi(Me)-a-BT**

Excited State 1: 2.5290 eV 490.25 nm f=1.2273

HOMO(129)-LUMO(130) 0.70092

Excited State 2: 3.2067 eV 386.64 nm f=0.3042
129-132 0.69469

The calculated excited state of **S-Imi(Me)-a-BT**

Excited State 1: 2.1606 eV 573.83 nm f=1.0217
HOMO(145)-LUMO(146) 0.69646
Excited State 2: 2.6754 eV 463.43 nm f=0.3801
145-148 0.69412

The calculated excited state of **Imi(Me)-T-BT**

Excited State 1: 2.1614 eV 573.64 nm f=0.9954
HOMO(159)-LUMO(160) 0.70074
Excited State 2: 2.8440 eV 435.96 nm f=0.4144
159-162 0.69477
Excited State 3: 2.8557 eV 434.17 nm f=0.0123
158-160 0.35441
159-161 0.60399
Excited State 4: 3.0529 eV 406.12 nm f=0.1002
158-160 0.59490
159-161 -0.35242
159-164 -0.10564

The calculated excited state of **S-Imi(Me)-T-BT**

Excited State 1: 1.8745 eV 661.44 nm f=0.9759
HOMO(175)-LUMO(176) 0.70031
Excited State 2: 2.0190 eV 614.09 nm f=0.0282
173-177 0.15223
174-176 0.15735
175-177 0.66368
Excited State 3: 2.2760 eV 544.75 nm f=0.2480
175-178 0.69827
Excited State 4: 2.7053 eV 458.31 nm f=0.0391
168-176 -0.14710
172-176 0.66579

The calculated excited state of **Imi(Me)-TzTz**

Excited State 1: 2.9933 eV 414.21 nm f=1.1768
HOMO(118)-LUMO(119) 0.70302

Excited State	2:	3.7981 eV	326.44 nm	f=0.1604
111-119			-0.11327	
114-119			-0.14888	
118-121			0.66764	

The calculated excited state of **S-Imi(Me)-TzTz**

Excited State	1:	2.3385 eV	530.19 nm	f=0.5492
HOMO(134)-LUMO(135)			0.64397	
128-135			-0.14128	
130-135			-0.16167	
131-136			0.13989	
Excited State	2:	3.1555 eV	392.92 nm	f=0.0562
128-135			0.59155	
129-136			0.34169	

Materials

All reactions were carried out under a nitrogen atmosphere. Solvents of the highest purity grade were used as received. Unless stated otherwise, all reagents were purchased from commercial sources and used without purification. Intermediate **10**[8] and **11**[3] were prepared by reported procedure, and ^{1}H NMR data of this compound was in agreement with those previously reported.

Synthesis

*Synthesis of **8***: 4-Bromophthalic anhydride (2.0 g, 8.8 mmol) and 2-ethyl-1-hexylamine (1.2 g, 8.8 mmol) were placed in a round-bottomed flask and dissolved with DMF (50 mL), and the resulting mixture was stirred at 140 ºC for 12 h. After being cooled to room temperature, the reaction was quenched by the addition of H_2O. The aqueous layer was extracted with ethyl acetate (EtOAc), and the combined organic layer was washed with water and dried over Na_2SO_4. After removal of the solvent under reduced pressure, the residue was purified by column chromatography on silica gel (hexane/EtOAc = 10/1) to give **8** (2.3 g, 75%). Colorless solid; m.p.: 72-73 °C; ^{1}H NMR (400 MHz, $CDCl_3$, TMS): δ 7.96 (d, J = 1.6 Hz, 1H), 7.83 (dd, J = 7.8, 1.6 Hz, 1H), 7.69 (d, J = 7.8 Hz, 1H), 3.56 (d, J = 7.3 Hz, 2H), 1.81 (m, 1H), 1.35-1.25 (m, 8H), 0.91-0.85 (m, 6H); ^{13}C NMR (100 MHz, $CDCl_3$): δ 167.91, 167.36, 136.85, 133.75, 130.62, 128.77, 126.58, 124.56, 42.12, 38.24, 30.46, 28.46, 23.80, 22.99, 14.07, 10.39; MS (GC) *m/z* 337 (M^+, Calcd 337). Anal. Calcd for $C_{16}H_{20}BrNO_2$: C, 56.82; H, 5.96; N, 4.14. Found: C, 56.88; H, 6.01; N, 4.06.

*Synthesis of **9***: **8** (100 mg, 0.30 mmol) and Lawesson's reagent (238 mg, 0.59 mmol) were placed in a test tube with screw cap and dissolved with toluene (5 mL), and the resulting mixture was stirred at 120 ºC for 12 h. After removal of the solvent under reduced pressure, the residue was purified by column chromatography on silica gel (hexane/EtOAc = 10/1) to give **9** (45 mg, 41%). Dark brown oil; ^{1}H NMR (400 MHz, $CDCl_3$, TMS): δ 7.97 (d, J =

1.1 Hz, 1H), 7.79 (dd, *J* = 7.8, 1.1 Hz, 1H), 7.70 (d, *J* = 7.8 Hz, 1H), 4.36 (dd, *J* = 7.3, 2.1 Hz, 2H), 2.18 (m, 1H), 1.36-1.21 (m, 8H), 0.90-0.85 (m, 6H); ^{13}C NMR (100 MHz, $CDCl_3$): δ 197.07, 196.52, 135.75, 135.74, 133.23, 127.80, 126.25, 124.63, 48.06, 38.18, 30.55, 28.50, 23.94, 22.99, 14.05, 10.79; MS (GC) *m/z* 369 (M^+, Calcd 369). Anal. Calcd for $C_{16}H_{20}BrNS_2$: C, 51.89; H, 5.44; N, 3.78. Found: C, 51.62; H, 5.44; N, 3.80.

*Synthesis of **12***: 4-Methylphthalic anhydride (3.0 g, 18.5 mmol) and 2-ethyl-1-hexylamine (2.4 g, 18.5 mmol) were placed in a round-bottomed flask and dissolved with DMF (75 mL), and the resulting mixture was stirred at 140 ºC for 12 h. After being cooled to room temperature, the reaction was quenched by the addition of H_2O. The aqueous layer was extracted with EtOAc, and the combined organic layer was washed with water and dried over Na_2SO_4. After removal of the solvent under reduced pressure, the residue was purified by column chromatography on silica gel (hexane/EtOAc =10/1) to give **12** (3.0 g, 60%). Colorless solid; m.p.: 47-49 °C; ^{1}H NMR (400 MHz, $CDCl_3$, TMS): δ 7.71 (d, *J* = 7.6 Hz, 1H), 7.63 (d, *J* = 1.1 Hz, 1H), 7.48 (dd, *J* = 7.6, 1.1 Hz, 1H), 3.55 (d, *J* = 7.3 Hz, 2H), 2.50 (s, 3H), 1.83-1.80 (m, 1H), 1.37-1.26 (m, 8H), 0.92-0.85 (m, 6H); ^{13}C NMR (100 MHz, $CDCl_3$): δ 168.92, 168.82, 145.03, 134.32, 132.45, 129.47, 123.69, 123.03, 41.79, 38.23, 30.45, 28.47, 23.78, 22.96, 21.96, 14.03, 10.38; MS (GC) *m/z* 273 (M^+, Calcd 273). Anal. Calcd for $C_{17}H_{23}NO_2$: C, 74.69; H, 8.48; N, 5.12. Found: C, 74.66; H, 8.35; N, 5.12.

*Synthesis of **13***: To a stirred solution of **12** (1.00 g, 3.65 mmol) in CCl_4 (15 mL) was added NBS (0.97 g, 5.47 mmol), benzoyl peroxide (BPO) (88 mg, 0.37 mmol), and the resulting mixture was stirred at 90 ºC for 12 h. After being cooled to room temperature, the reaction was quenched by the addition of $NaHCO_3$ aq., and the organic layer was separated. The aqueous layer was extracted with $CHCl_3$, and the combined organic layer was washed with water and dried over Na_2SO_4. After removal of the solvent under reduced pressure, the residue was purified by column chromatography on silica gel (hexane/EtOAc = 10/1) to give bromo compound **A** (1.00 g). ^{1}H NMR (400 MHz, $CDCl_3$, TMS): δ 7.84 (br, 1H), 7.79 (d, *J* = 7.3 Hz, 1H), 7.70 (dd, *J* = 7.3, 1.6 Hz, 1H), 5.56 (d, *J* = 6.9 Hz, 2H), 4.54 (s, 2H), 2.03 (m, 1H), 1.42-1.23 (m, 8H), 0.95-0.86 (m, 6H). This compound was used for next step without further purification.

A mixture of **A** (1.00 g), silver trifluoroacetate (748 mg, 3.39 mmol) in 1,4-dioxane (8 mL) and water (2mL) was stirred at room temperature. After stirring for 12 h, the reaction mixture was filtered over celite with $CHCl_3$ as an eluent, and the organic layer was separated. The aqueous layer was extracted with $CHCl_3$, and the combined organic layer was washed with water and dried over Na_2SO_4. After removal of the solvent under reduced pressure, the residue was purified by column chromatography on silica gel (hexane/EtOAc = 3/1) to give alcohol **13** (350 mg, 33% (2 steps)). Colorless solid; m.p.: 80-81 °C; ^{1}H NMR (400 MHz, $CDCl_3$, TMS): δ 7.85 (d, *J* = 1.6 Hz, 1H), 7.82 (d, *J* = 7.8 Hz, 1H), 7.71 (dd, *J* = 7.8, 1.6 Hz, 1H), 4.87 (s, 2H), 3.57 (d, *J* = 7.4 Hz, 2H), 1.93 (br, 1H), 1.83 (m, 1H), 1.36-1.25 (m, 8H), 0.93-0.86 (m, 6H); ^{13}C NMR (100 MHz, $CDCl_3$): δ 168.69, 168.62, 147.76, 132.57, 131.76, 131.19, 123.33, 121.21, 64.38, 41.94, 38.27, 30.49, 28.49, 23.81, 23.00, 14.07, 10.41; MS (GC) *m/z* 351 (M^+, Calcd 351). Anal. Calcd for $C_{17}H_{23}NO_3$: C, 70.56; H, 8.01; N, 4.84. Found: C, 70.73; H, 7.32; N, 4.81.

*Synthesis of **14***: To a stirred solution of **13** (300 mg, 1.03 mmol) in CH_2Cl_2 (10 mL) was added MnO_2 (895 mg, 10.3

mmol), and the resulting mixture was stirred at room temperature. After stirring for 12 h, the reaction mixture was filtered over celite with $CHCl_3$ as an eluent. After removal of the solvent under reduced pressure, the residue was purified by column chromatography on silica gel (hexane/EtOAc = 3/1) to give aldehyde **14** (245 mg, 83%). Colorless solid; m.p.: 47-50 °C; ^{1}H NMR (400 MHz, $CDCl_3$, TMS): δ 10.17 (s, 1H), 8.34 (s, 1H), 8.25 (dd, J = 7.8, 1.4 Hz, 1H), 8.02 (d, J = 1.4 Hz, 1H), 3.62 (d, J = 7.5 Hz, 2H), 1.85 (m, 1H), 1.36-1.26 (m, 8H), 0.94-0.87 (m, 6H); ^{13}C NMR (100 MHz, $CDCl_3$): δ 190.23, 167.52, 167.40, 140.56, 136.38, 135.24, 132.89, 124.02, 123.88, 42.29, 38.24, 30.46, 28.43, 23.80, 22.97, 14.04, 10.36; MS (GC) *m/z* 287 (M^+, Calcd 287). Anal. Calcd for $C_{17}H_{21}BNO_3$: C, 71.06; H, 7.37, N, 4.87. Found: C, 70.73; H, 7.32; N, 4.81.

*Synthesis of **Imi-a-BT***: **8** (189 mg, 0.67 mmol), **10** (89 mg, 0.30 mmol), CuI (5 mg, 0.03 mmol), and $Pd(PPh_3)_4$ (39 mg, 0.03 mmol) were placed in a test tube with screw cap and dissolved with THF (6 mL) and diisopropylethylamine (0.6 mL). After being cooled to room temperature, the reaction mixture was filtered over celite with $CHCl_3$ as an eluent. After removal of the solvent under reduced pressure, the residue was purified by column chromatography on silica gel ($CHCl_3$), followed by purification with preparative GPC ($CHCl_3$) to give **Imi-a-BT** (189 mg, 89%). Yellow solid; m.p.: 225-226 °C; ^{1}H NMR (400 MHz, $CDCl_3$, TMS): δ 8.10 (d, J = 0.9 Hz, 2H), 7.98 (dd, J = 7.8, 0.9 Hz, 2H), 7.86 (d, J = 7.8 Hz, 2H), 7.86 (s, 2H), 3.59 (d, J = 7.3 Hz, 4H), 1.84 (m, 2H), 1.37-1.27 (m, 16H), 0.93-0.86 (m, 12H); ^{13}C NMR (100 MHz, $CDCl_3$): δ 167.98, 167.86, 154.18, 137.17, 132.91, 132.43, 131.60, 128.37, 126.42, 123.29, 117.04, 95.83, 88.93, 42.13, 38.27, 30.48, 28.47, 23.83, 23.00, 14.06, 10.40; MS MALDI-TOF(1,8,9-trihydroxyanthracene matrix) *m/z* 698.14 (M^+, Calcd 698.29); Anal. Calcd for $C_{42}H_{42}N_4O_4S$: C, 72.18; H, 6.06; N, 8.02. Found: C, 71.92; H, 6.14; N, 7.90.

*Synthesis of **S-Imi-a-BT***: **Imi-a-BT** (230 mg, 0.24 mmol) and Davy's reagent (375 mg, 1.32 mmol) were placed in a test tube with screw cap and dissolved with toluene (36 mL), and the resulting mixture was stirred at 120 ºC for 12 h. After removal of the solvent under reduced pressure, the residue was purified by column chromatography on silica gel ($CHCl_3$), followed by precipitation using $CHCl_3$ and acetone to give **S-Imi-a-BT** (220 mg, 88%). Red Solid; m.p.: > 300 °C; ^{1}H NMR (400 MHz, $CDCl_3/CS_2$, TMS): δ 8.07 (d, J = 1.5 Hz, 2H), 7.90 (dd, J = 7.8, 1.5 Hz, 2H), 7.84 (d, J = 7.8 Hz, 2H), 7.82 (s, 2H), 4.37 (d, J = 7.0 Hz, 4H), 2.18 (m, 2H), 1.39-1.25 (m, 16H), 0.92-0.86 (m, 12H); ^{13}C NMR (100 MHz, $CDCl_3/CS_2$): δ 196.44, 196.39, 154.02, 135.75, 134.63, 133.88, 132.55, 127.17, 126.55, 123.24, 117.08, 96.76, 89.28, 47.81, 38.18, 30.62, 28.62, 24.09, 23.20, 14.16, 10.86; MS MALDI-TOF(1,8,9-trihydroxyanthracene matrix) *m/z* 762.09 (M^+, Calcd 762.20); Anal. Calcd for $C_{42}H_{42}N_4S_5$: C, 66.10; H, 5.55; N, 7.34. Found: C, 65.84; H, 5.79; N, 7.42.

*Synthesis of **Imi-T-BT***: **8** (128 mg, 0.38 mmol), **11** (100 mg, 0.15 mmol), $Pd(PPh_3)_4$ (18 mg, 0.016 mmol) and toluene (5 mL) were placed in a microwave proof walled glass vial with a snap cap. The glass vial was purged with nitrogen, securely sealed and heated in a microwave reactor, keeping the temperature at 180 °C for 5min. After removal of the solvent under reduced pressure, the residue was purified by column chromatography on silica gel ($CHCl_3$), followed by purification with preparative GPC ($CHCl_3$) to give **Imi-T-BT** (128 mg, 91%). Red solid; m.p.: ^{1} H NMR (400 MHz, $CDCl_3$, TMS): δ 8.15 (d, 2H, J = 5.5 Hz), 8.15 (s, 2H), 8.00 (d, 2H, J = 7.8 Hz), 7.96 (s, 2H),

7.85 (d, 2H, *J* = 7.8 Hz), 7.59 (d, 2H, *J* = 5.5 Hz), 3.60 (d, 4H, *J* = 7.8 Hz), 1.85 (m, 2H), 1.30 (m, 16H), 0.91 (m, 12H); Anal. Calcd for $C_{46}H_{46}N_4O_4S_3$: C, 67.78; H, 5.69; N, 6.87; Found: C, 67.63; H, 5.74; N, 6.88.

Synthesis of ***S-Imi-T-BT***: **Imi-T-BT** (50 mg, 0.061 mmol) and Davy's reagent (68 mg, 0.24 mmol) were placed in a test tube with screw cap and dissolved with toluene (5 mL), and the resulting mixture was stirred at 120 ºC for 12 h. After removal of the solvent under reduced pressure, the residue was purified by column chromatography on silica gel ($CHCl_3$), followed by precipitation using $CHCl_3$ and acetone to give **S-Imi-T-BT** (33 mg, 62%). Deep Purple Solid; ^{1}H NMR (400 MHz, $CDCl_3/CS_2$, TMS): δ 8.15 (d, *J* = 1.4 Hz, 2H), 8.11 (d, *J* = 4.1, Hz, 2H), 7.91 (dd, *J* = 7.8 and 1.4 Hz, 2H), 7.90 (s, 2H), 7.82 (d, *J* = 7.8 Hz, 2H), 7.59 (d, *J* = 4.1, Hz, 2H), 4.38 (d, *J* = 7.0 Hz, 4H), 2.20 (m, 2H), 1.32 (m, 16H), 0.89 (m, 12H).

Synthesis of ***Imi-TzTz***: **14** (220 mg, 1.03 mmol), etahnedithioamide (368 mg, 3.06 mmol) were placed in a test tube with screw cap and dissolved with DMF (10 mL), and the resulting mixture was stirred at 140 ºC for 12 h. After being cooled to room temperature, the reaction mixture was quenched by addition of water, and the organic layer was separated with $CHCl_3$. After removal of the solvent under reduced pressure, the residue was purified by column chromatography on silica gel ($CHCl_3$), followed by precipitation using $CHCl_3$ and acetone to give **Imi-TzTz** (174 mg, 69%). Yellow solid; m.p.: 218-220 °C; ^{1}H NMR (400 MHz, $CDCl_3$, TMS): δ 8.44 (d, *J* = 1.6 Hz, 2H), 8.38 (dd, *J* = 7.8, 1.6 Hz, 2H), 7.95 (d, *J* = 7.8 Hz, 2H), 3.62 (d, *J* = 7.1 Hz, 4H), 1.85 (m, 2H), 1.38-1.28 (m, 16H), 0.93-0.86 (m, 12H); ^{13}C NMR (100 MHz, $CDCl_3$): δ 167.84, 167.75, 167.70, 152.36, 138.95, 133.25, 133.23, 131.57, 124.04, 121.01, 42.21, 38.25, 30.47, 28.46, 23.81, 22.99, 14.06, 10.39; MS MALDI-TOF(1,8,9-trihydroxyanthracene matrix) *m/z* 656.00 (M^+, Calcd 656.25); Anal. Calcd for $C_{36}H_{40}N_4O_4S_2$: C, 65.83; H, 6.14; N, 8.53. Found: C, 65.82; H, 6.14; N, 8.56.

Synthesis of ***S-Imi-TzTz***: **Imi-TzTz** (100 mg, 0.15 mmol) and Davy's reagent (173 mg, 0.61 mmol) were placed in a test tube with screw cap and dissolved with toluene (10 mL), and the resulting mixture was stirred at 120 ºC for 12 h. After removal of the solvent under reduced pressure, the residue was purified by column chromatography on silica gel ($CHCl_3$), followed by precipitation using $CHCl_3$ and acetone to give **S-Imi-TzTz** (97 mg, 88%). Red solid; m.p.: 261-262 °C; ^{1}H NMR (400 MHz, $CDCl_3/CS_2$, TMS): δ 8.38 (d, *J* = 1.4 Hz, 2H), 8.31 (dd, *J* = 7.8, 1.4 Hz, 2H), 7.89 (d, *J* = 7.8 Hz, 2H), 4.36 (dd, *J* = 7.3, 2.3 Hz, 4H), 2.17 (m, 2H), 1.38-1.24 (m, 16H), 0.92-0.86 (m, 12H); ^{13}C NMR (100 MHz, $CDCl_3/CS_2$): δ 196.01, 195.98, 167.57, 152.28, 137.61, 135.23, 135.18, 130.10, 123.85, 121.04, 47.81, 38.16, 30.63, 28.63, 24.13, 23.24, 14.20, 10.87; MS MALDI-TOF(1,8,9-trihydroxyanthracene matrix) *m/z* 719.85 (M^+, Calcd 720.16); Anal. Calcd for $C_{36}H_{40}N_4S_6$: C, 59.96; H, 5.59; N, 7.77. Found: C, 60.06; H, 5.64; N, 7.78.

2.8 References

1 X. Zhan, A. Facchetti, S. Barlow, T. J. Marks, M. A. Ratner, M. R. Wasielewski and S. R. Marder, *Adv. Mater.*, 2011, **23**, 268; C. Huang, S. Barlow and S. R. Marder, *J. Org. Chem.*, 2011, **33**, 2386; C. Li, H. Wonneberger, *Adv. Mater.*, 2012, **24**, 613; H. E. Katz, A. J. Lovinger, J. Johnson, C. Kloc, T. Siegrist, W. Li, Y.-Y. Lin and A.

Dodabalapur, *Nature*, 2000, **404**, 478; B. A. Jones, M. J. Ahrens, M.-H. Yoon, A. Facchetti, T. J. Marks and M. R. Wasielewski, *Angew. Chem., Int. Ed.*, 2004, **43**, 6363; X. Zhan, A. Facchetti, S. Barlow, T. J. Marks, M. A. Ratner, M. R. Wasielewski, S. R. Marder, *Adv. Mater.*, 2011, **23**, 268; M.-M. Ling, P. Erk, M. Gomez, M. Koenemann, J. Locklin, Z. Bao, *Adv. Mater.*, 2007, **19**, 1123; H. Yan, Z. Chen, Y. Zheng, C. Newman, J. R. Quinn, F. Dötz, M. Kastler, A. Facchetti, *Nature*, 2009, **457**, 679; X. Gao, C.-a. Di, Y. Hu, X. Yang, H. Fan, F. Zhang, Y. Liu, H. Li, D. Zhu, *J. Am. Chem. Soc.*, 2010, **132**, 3697; J. Li, J.-J. Chang, H. S. Tan, H. Jiang, X. Chen, Z. Chen, J. Zhangb and J. Wu, *Chem. Sci.*, 2012, **3**, 846; J. Chang, J. Li, K. L. Chang, J. Zhang and J. Wu, *RSC Advances*, 2013, **3**, 8721; M. Melucci, M. Zambianchi, L. Favaretto, M. Gazzano, A. Zanelli, M. Monari, R. Capelli, S. Troisi, S. Toffanind and M. Muccini, *Chem. Commun.*, 2011, **47**, 11840; L. Schmidt-Mende, A. Fechtenkoötter, K. Müllen, E. Moons, R. H. Friend, J. D. MacKenzie, *Science*, 2001, **293**, 1119; E. Ahmed, G. Ren, F. S. Kim, E. C. Hollenbeck and S. A. Jenekhe, *Chem. Mater.*, 2011, **23**, 4563; J. T. Bloking, X. Han, A. T. Higgs, J. P. Kastrop, L. Pandey, J. E. Norton, C. Risko, C. E. Chen, J.-L. Brédas, M. D. McGehee and A. Sellinger, *Chem. Mater.*, 2011, **23**, 5484; T. V. Pho, F. M. Toma, M. L. Chabinyc and F. Wudl, *Angew. Chem., Int. Ed.*, 2013, **52**, 1446.

2 S. T. Turner, P. Pingel, R. Steyrleuthner, E. J. W. Crossland, S. Ludwigs and D. Neher, *Adv. Funct. Mater.*, 2011, **21**, 4640; Yamagata and F. C. Spano, *J. Chem. Phys.*, 2012, **136**, 184901.

3 B. Fu, J. Baltazar, Z. Hu, A.-T. Chien, S. Kumar, C. L. Henderson, D. M. Collard and E. Reichmanis, *Chem. Mater.*, *2012*, **24**, 4123..

4 A. J. Bard and L. R. Faulkner, *Electrochemical Methods–Fundamentals and Applications*: Wiley: New York, 1984; J. Pommerehne, H. Vestweber, W. Guss, R. F. Mahrt, H. Bässler, M. Porsch and J. Daub, *Adv. Mater.*, 1995, **7**, 551.

5 M. Mas-Torrent and C. Rovira, *Chem. Rev.*, 2011, **111**, 4833.

6 Kim, T. D. Anthopoulos, P. N. Stavrinou, D. D. C. Bradley and J. Nelson, *Nat. Mater.*, 2008, **7**, 158; Y.-S. Hsiao, W.-T. Whang, S.-C. Suen, J.-Y. Shiu and C.-P. Chen, *Nanotechnology*, 2008, **19**, 415603; C. M. Björström, A. Bernasik, J. Rysz, A. Budkowski, S. Nilsson, M. Svensson, M. R. Andersson, K. O. Magnusson and E. Moons, *J. Phys.: Condens. Matter.*, 2005, **17**, L529.

7 D. H. Kaelble and K. C. Uy, *J. Adhesion*, 1970, 2, 50.

8 F. Schlütter, A. Wild, A. Winter, M. D. Hager, A. Baumgaertel, C. Friebe and U. S. Schubert, *Macromolecules*, 2010, **43**, 2759.

Chapter 3
Structural Modification of Linearly Extended Acceptor Materials and the Influence on Molecular Properties and Photovoltaic Performances

3.1 Introduction

Nanoscale structure, which including morphology, molecular arrangements and orientations has been recognized as a critical research issue in BHJ type OPVs.[1] As the results of chapter 2, the author developed phthalimide and phthaldithioimide-based compounds containting benzothiadiazole as a central unit (Figure 3.1). The OPV device whose active layer consists of P3HT as a donor and **Ph-EH** as acceptor materials, showed moderate OPV performance. In contrast, despite the LUMO energy level close to that of $PC_{61}BM$ and a superior electron-transporting (n-type) field-effect response than that of **Ph-EH** in transistors, OPVs based on S-**Ph-EH** showed a poor PCE. Interestingly, as indicated by contact angle measurements, **Ph-EH** and $PC_{61}BM$ appears notably high SFE and γ^d values. The author considered these index could be a representable character influence to the OPV performances.

Thanks to the synthetic flexibility of terminal imide unit, it is possible to design a series of benzothiadiazole based acceptor materials with different crystallinity, electronic properties, and thin-film properties. With this concept in mind, the author designed and systematically investigated the molecular and film properties, and electron-transporting and photovoltaic characteristics of a series of Ph-X (X = H, D, EH, MH, and Ipop) and Ar-EH (Ar = Th, Py, and Na) (Figure 3.1). Their central structures were fixed to the strongly electron-withdrawing benzothiadiazole unit and only the terminal alkyl chains or π-conjugated imide units were modified; the effect of this modification on the photovoltaic characteristics was monitored. Through comparing properties and OPV characteristics, the relationships among chemical structure, physical properties, thin-film properties, and photovoltaic performances of photovoltaic device were tried to explicate.

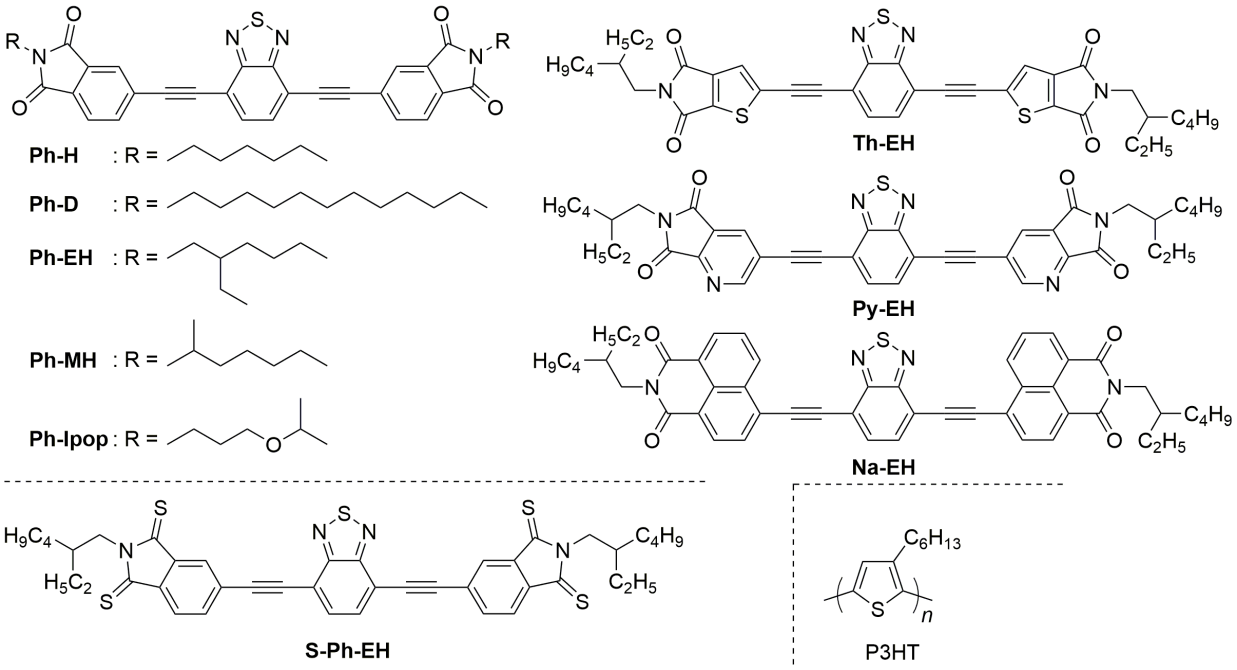

Figure 3.1. Chemical structures of Ph-X (X = H, D, EH, MH, and Ipop) and Ar-EH (Ar = Th, Py, and Na).

3.2 Synthesis

The synthesis of the target compounds was carried out in a modular synthetic approach, i.e., the central and terminal units were obtained separately and then con-nected via transition metal-catalyzed cross-coupling reactions (Scheme 3.1). The synthesized compounds, except for **Na-EH**, were soluble in common organic solvents such as $CHCl_3$, chlorobenzene (CB), and *o*-DCB.

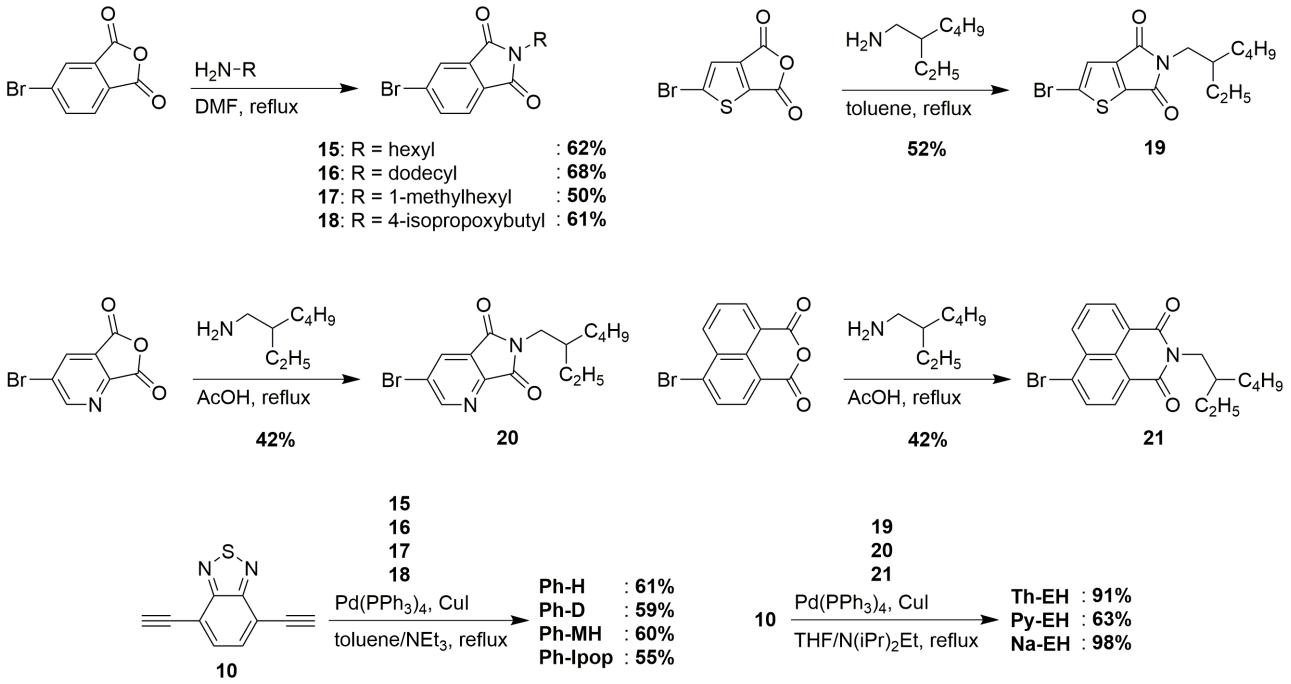

Scheme 3.1. Synthesis of target compounds.

3.3 Thermophysical, Photophysical and Electrochemical Properties

The thermal properties were investigated using thermogravimetric analysis (TGA) and DSC. As shown in Figure 3.2 and Table 3.1, all compounds showed a good thermal behavior with a 5% weight loss temperature (T_d) over 400 °C, suggesting a sufficient thermal stability for the application in organic electronic devices. During the DSC analysis, these compounds exhibited typical melting and crystallization peaks; no other significant thermal phase transition was observed (Figure 3.3). Notably, the peaks corresponding to the crystallization of **Ph-MH** and **Ph-Ipop** in the cooling run are broad and show a larger separation from their melting peaks compared with the others, indicating that the introduction of 1-methylhexyl (MH) and 3-isopropoxypropyl (Ipop) chains lead to weak crystallinity of the compounds.

The photophysical properties of Ph-X (X = H, D, EH, MH, and Ipop) and Ar-EH (Ar = Ph, Th, and Py) series were investigated by UV-Vis spectroscopy in a dilute $CHCl_3$ solution and films. The relevant optoelectronic data are collected in Table 3.1. As shown in Figure 3.4, all compounds exhibit similar spectra in solution, e.g., both absorption maxima (λ_{max}) and onset of Ph-X compounds in solution overlap, implying that the absorption profiles of the π-conjugated systems are virtually unaffected by the terminal alkyl groups. In contrast, the terminal areneimide units in Ar-EH compounds exert a clear influence on the optical energy gaps (ΔE_{opt}), which were determined form absorption onsets. In contrast to the solution spectra, the absorption bands in the film state of all

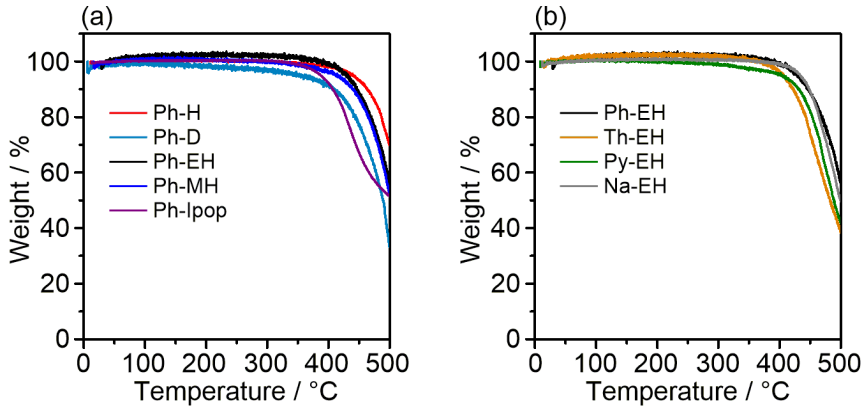

Figure 3.2. TGA curves of (a) Ph-X (X = H, D, EH, MH, and Ipop) and (b) Ar-EH (Ar = Ph, Th, Py, and Na) with a scanning rate of 10 °C min^{-1} under N_2.

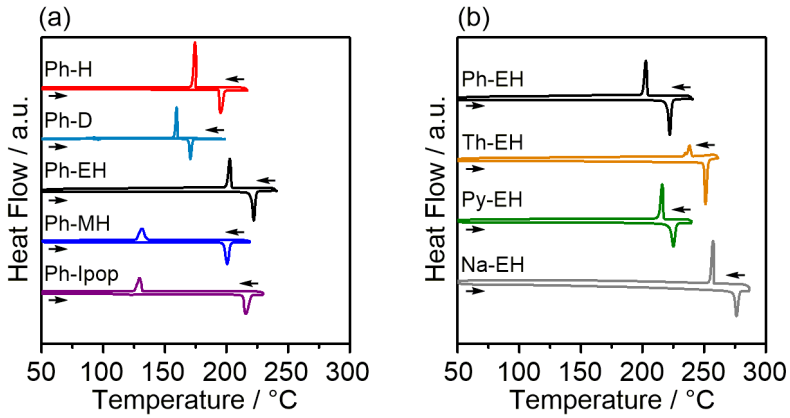

Figure 3.3. DSC profiles of (a) Ph-X (X = H, D, EH, MH, and Ipop) and (b) Ar-EH (Ar = Ph, Th, Py, and Na) with a scanning rate of 10 °C min^{-1} under N_2.

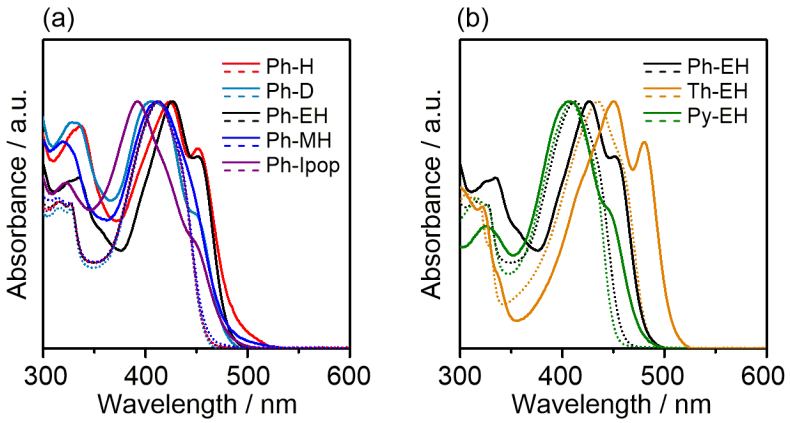

Figure 3.4. UV-Vis absorption spectra of (a) Ph-X (X = H, D, EH, MH, and Ipop) and (b) Ar-EH (Ar = Ph, Th, and Py) in a $CHCl_3$ solution (dashed line) and in a film state (solid line).

compounds showed a small red-shift, except for **Ph-Ipop**, which was characterized by a broadening of the peak and a blue-shift of λ_{max}. This may be due to the Davydov-splitting[2] or to the polymorphism nature[3] of **Ph-Ipop**. In

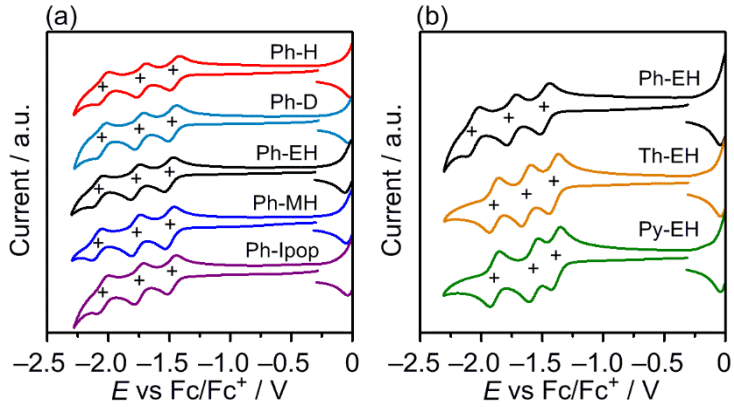

Figure 3.5. Cyclic voltammograms of (a) Ph-X (X = H, D, EH, MH, and Ipop) and (b) Ar-EH (Ar = Ph, Th, and Py), measured in *o*-DCB/acetonitrile (5/1) containing 0.1 M $TBAPF_6$.

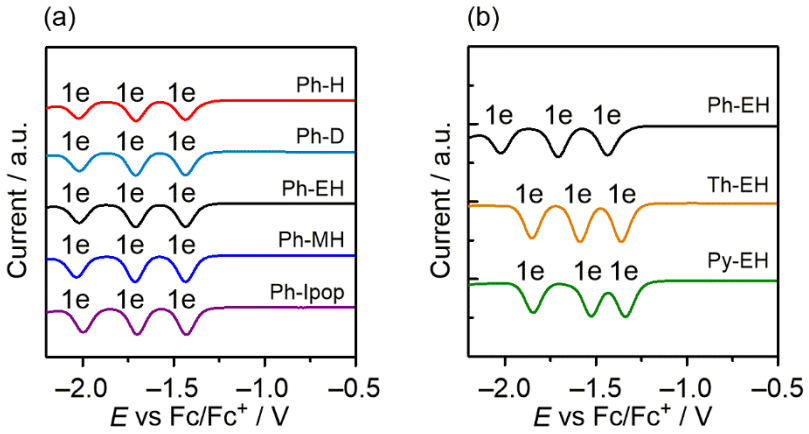

Figure 3.6. Differential pulse voltammograms of (a) Ph-X (X = H, D, EH, MH, and Ipop) and (b) Ar-EH (Ar = Ph, Th, and Py), measured in *o*-DCB/acetonitrile (5/1) containing 0.1 M $TBAPF_6$.

Table 3.1. Properties of compounds.

Compounds	λ_{max} [nm][a]	ΔE_{opt} [eV][b]	$E_{red1/2}$ [eV][c]	E_{LUMO} [eV][d]	E_{HOMO} [eV][e]	T_m/T_c [°C][f]
Ph-H	412	2.70	–1.48, –1.75, –2.07	–3.32	–6.02	195 / 174
Ph-D	412	2.70	–1.48, –1.75, –2.06	–3.32	–6.02	170 / 159
Ph-EH	412	2.70	–1.48, –1.78, –2.07	–3.32	–6.02	223 / 202
Ph-MH	412	2.70	–1.49, –1.76, –2.08	–3.31	–6.01	201 / 131
Ph-Ipop	412	2.70	–1.48, –1.75, –2.04	–3.32	–6.02	216 / 129
Th-EH	435	2.58	–1.40, –1.64, –1.90	–3.40	–5.98	251 / 238
Py-EH	409	2.76	–1.38, –1.48, –1.89	–3.42	–6.18	225 / 216
Na-EH			not measured			276 / 257

[a] In $CHCl_3$. [b] Determined by the onset of the UV-Vis absorption spectrum in $CHCl_3$. [c] In *o*-DCB/acetonitrile (5/1), 0.1 M $TBAPF_6$, V vs. Fc/Fc^+. [d] Estimated from the approximation that the Fc/Fc^+ level is –4.8 eV vs. vacuum. [e] Determined by E_{LUMO} and ΔE_{opt}. [f] Melting point determined by DSC analysis.

addition, all compounds, except for **Ph-MH**, showed a distinct shoulder peak, which can be ascribed to a tighter crystal packing, possibly originating from an intermolecular π–π stacking of the backbones. In contrast, the decreased resolution of the peak shoulder detected for **Ph-MH** suggests that these interactions may be less strong because of steric hindrance of the branched alkyl chains. These results indicate again the weaker crystallinity of **Ph-MH** and **Ph-Ipop** than that of the others.

CV was employed to investigate the electrochemical properties of Ph-X and Ar-EH series. CV was performed in *o*-DCB/acetonitrile (5/1) solutions containing 0.1 M $TBAPF_6$. The measured potentials were calibrated using a ferrocene/ferrocenium (Fc/Fc+) redox couple as an internal standard. Their anodic CV scan detected no oxidation wave within the potential win-dow of solvent. In contrast, three reversible reduction waves in cathodic sweep were observed as shown in Figure 3.5 and Table 1. The differential pulse voltammetry measurements (Figure 3.6) confirmed that each reduction wave participated in one-electron process. This finding suggested that all compounds could be reversibly reduced into corresponding anionic species, a process facilitated by the presence of electron-withdrawing π-conjugated units. The LUMO energy levels (E_{LUMO}) of the Ph-X system are calculated from the half- wave reduction potential ($E_{red1/2}$) of the first reduction process, being virtually consistent with each other (−3.31 ~ −3.32 eV). This is possibly due to the small electronic contribution of the terminal alkyl groups to the

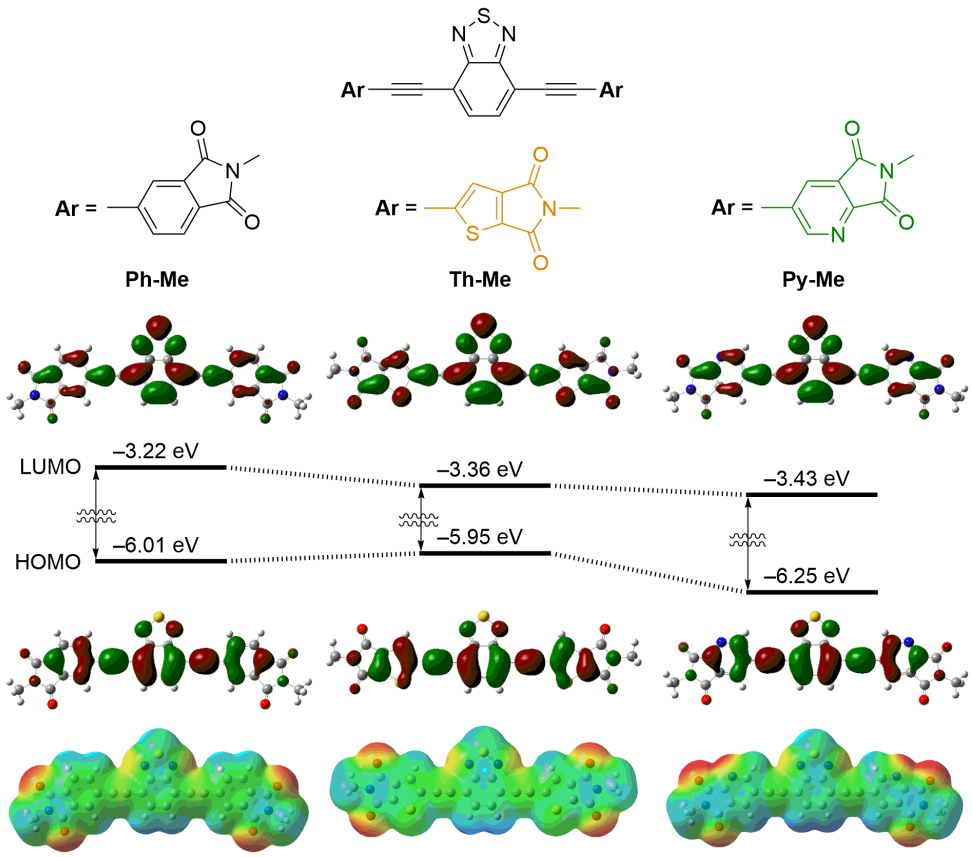

Figure 3.7. HOMO, LUMO, and ESP of model compounds calculated using DFT at the B3LYP/6-31G (d,p) level.

conjugated backbone. In contrast, terminal arene-imide units exert a significant influence on the LUMO energy levels, i.e., for **Ph-EH**, **Th-EH**, and **Py-EH** these were estimated to be –3.32, –3.40, and –3.42 eV, respectively. We

would like to remark that the experimentally estimated E_{LUMO} and ΔE_{opt} values are in qualitative good agreement with those obtained from DFT calculation at the B3LYP/6-31G (d,p) level of theory (Figure 3.7). The HOMO energy levels of these compounds deduced from the E_{LUMO} and ΔE_{opt} range between −5.98 and −6.18 eV. The estimated HOMO and LUMO energies for these compounds are thus lower than those of P3HT, estimated as −4.89 and −2.70 eV, respectively. This confirms that these compounds can be employed as acceptors when combined with P3HT in OPVs.

3.4 Electron Mobilities and Thin-film Properties

To obtain a relationship between molecular structure and film properties, we evaluated the electron-transporting characteristics of these compounds using OFET as well as the space-charge-limited currents (SCLC) techniques. The μ_e were measured using a bottom-gate/bottom-contact device configuration with spin-coated thin-films of the compounds on ODTS-treated Si/SiO_2 substrates. Primarily optimization of active layers was focused on the

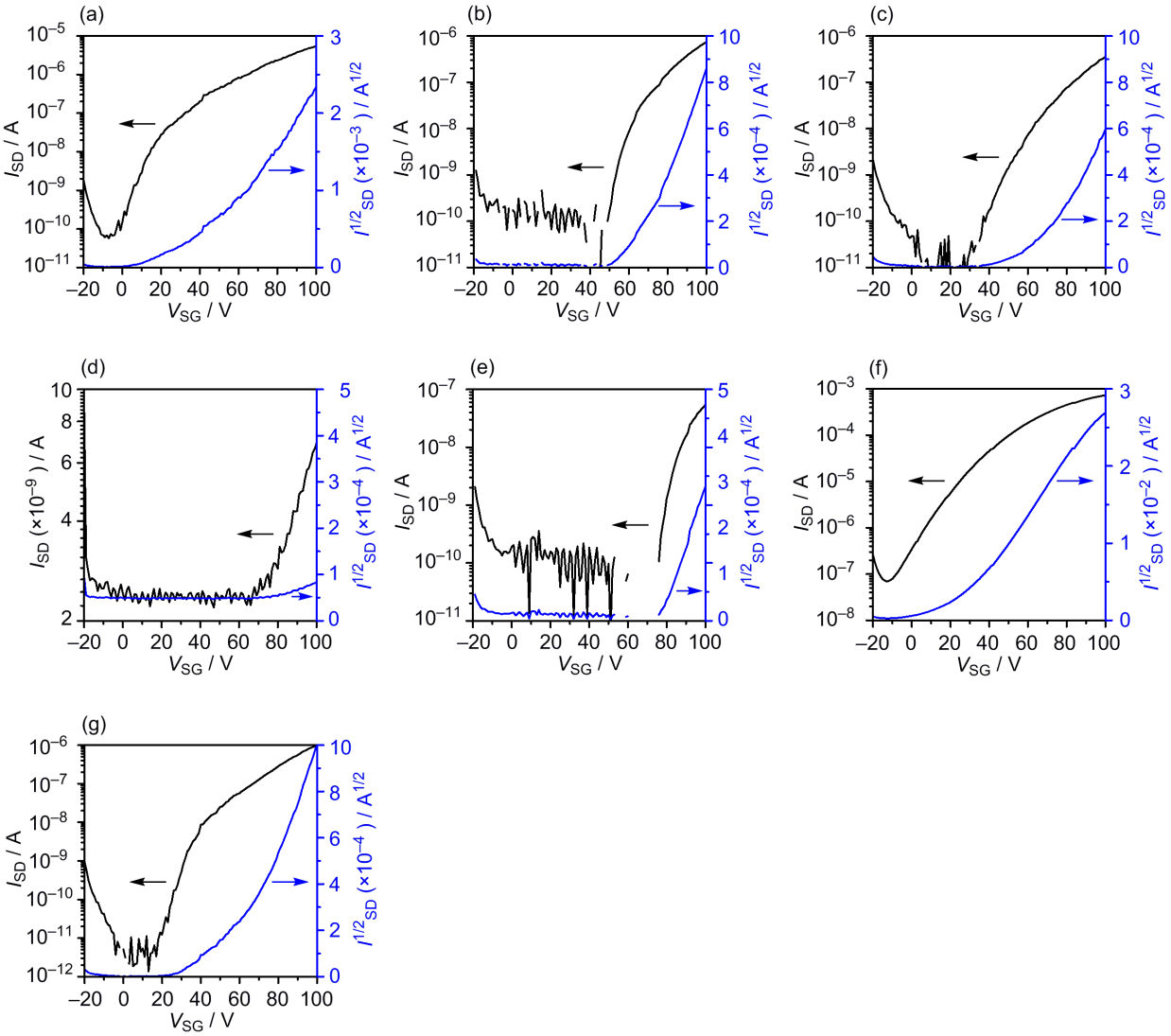

Figure 3.8. Transfer characteristics of (a) **Ph-H**, (b) **Ph-D**, (c) **Ph-EH**, (d) **Ph-MH**, (e) **Ph-Ipop**, (f) **Th-EH**, and (g) **Py-EH** -based OFETs. I_{SD} and V_{SG} denote source-drain current and gate voltage, respectively.

Table 3.2. Field-effect characteristics of Ph-X- and Ar-EH-based devices.

Compounds	T_a [°C]	μ_e [cm^2 V^{-1} s^{-1}]	I_{on} / I_{off}	V_{th} [V]
Ph-H	160	3.4×10^{-5}	10^5	67
Ph-D	190	9.3×10^{-6}	10^3	63
Ph-EH	160	5.4×10^{-6}	10^3	70
Ph-MH	130	4.1×10^{-8}	3	47
Ph-Ipop	190	1.9×10^{-6}	10^2	78
Th-EH	160	4.9×10^{-4}	10^4	38
Py-EH	160	1.1×10^{-5}	10^5	62

annealing temperature (T_a), and the representative parameters, including μ_e, I_{on}/I_{off}, and V_{th}, obtained from the optimized devices are summarized in Table 3.2. All compounds exhibited typical n-type responses, as expected from the estimation of the low-lying LUMO energy levels; the transfer characteristics are shown in Figure 3.8. A comparison of Ph-X (X = H, D, EH, MH, and Ipop) series with the same π-conjugated backbone shows that the terminal alkyl substituents exert a significant effect on the electron-transporting characteristics. In addition, it was found that the OFET device based on **Ph-H** has the highest electron mobility among Ph-X. Moreover, the decrease of the electron mobility was followed by a shift of the branching point of the alkyl chains towards the terminal imide unit (**Ph-EH** vs. **Ph-MH**). An analysis of the OFET characteristics of the π-conjugated systems having different terminal arene-imide units, but with the same 2-ethylhexyl groups Ar-EH (Ar = Th, Ph, and Py) revealed a significantly high electron mobility of **Th-EH**.

The large deviation in the electron mobility observed in this study was further investigated with XRD (Figure 3.9). In particular, **Ph-MH** films showed no obvious diffraction peaks on out-of-plane XRD measurements, suggesting an amorphous character of the thin films, which should be reflected in the low electron mobility. In contrast, other films displayed the first diffraction peaks in the range of 3°~6° (d = 2.9~1.5 nm), which correspond

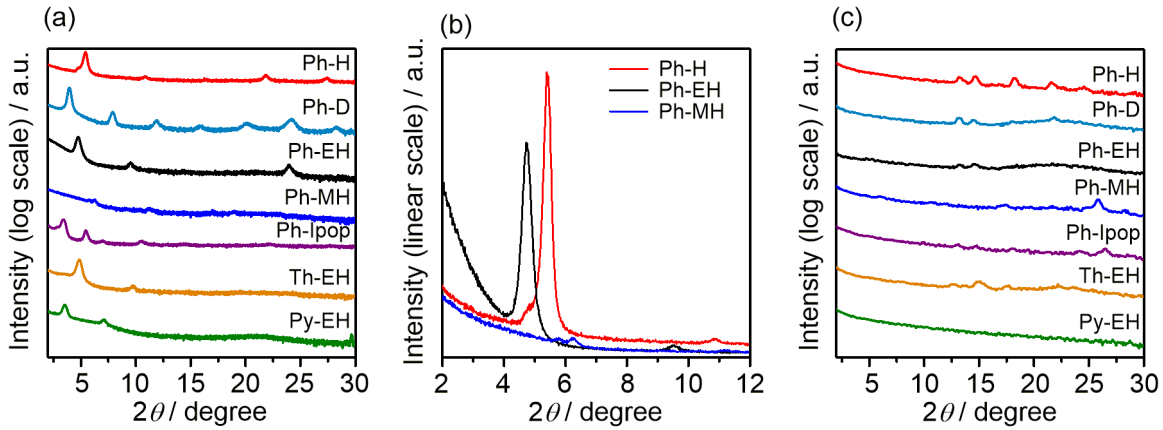

Figure 3.9. (a) Out-of-plane X-ray diffractograms of Ph-X (X = H, D, EH, MH, and Ipop) and Ar-EH (Ar = Th and Py) films. (b) Excerption of diffractograms for **Ph-H**, **Ph-EH**, and **Ph-MH**. (c) In-plane X-ray diffractograms of Ph-X (X = H, D, EH, MH, and Ipop) and Ar-EH (Ar = Th and Py) films.

to the lattice spacing of each molecular length toward long-axis direction. In addition, none of the films exhibited diffractions around 3° ~ 6° in in-plane XRD measurements (Figure 3.9). Thus, these results indicate that all compounds, except for **Ph-MH**, take an alignment with edge-on orientation on the SiO_2 surface, which is favorable for the carrier transport in OFETs. In fact, the electron mobilities estimated from the SCLC technique, which is known to measure charge-transporting properties in the direction perpendicular to the surface of the substrates, were rather low on the order of $10^{-6} \sim 10^{-8}$ cm^2 V^{-1} s^{-1} (Figure 3.10). However, in contrast to the trend of the field-effect mobilities, the amorphous **Ph-MH** films exhibited relatively high SCLC mobility (2.9×10^{-6} cm^2 V^{-1} s^{-1}) among all studied compound, interestingly being comparable with the field-effect mobility. A further analysis of the first XRD peak of the **Ph-EH** films showed a larger full width at half maximum value (0.74°) than that of **Ph-H** films (0.61°); moreover, a lower intensity of the diffraction peak of the **Ph-EH** films implied lower crystallinity than in the case of **Ph-H** (Figure 3.10 (b)).

Notably, a relationship between field-effect electron mobility and crystallinity of thin films was observed during the optimization of **Ph-EH**-based OFET devices. The **Ph-EH** thin films were fabricated on Si/SiO_2 substrates with different surface conditions: (1) bare substrate, (2) HMDS-modified substrate, (3) ODTS- modified substrate, and (4) ODTS-modified substrate with annealing at 160 °C, followed by FET measurements and out-of-plane XRD

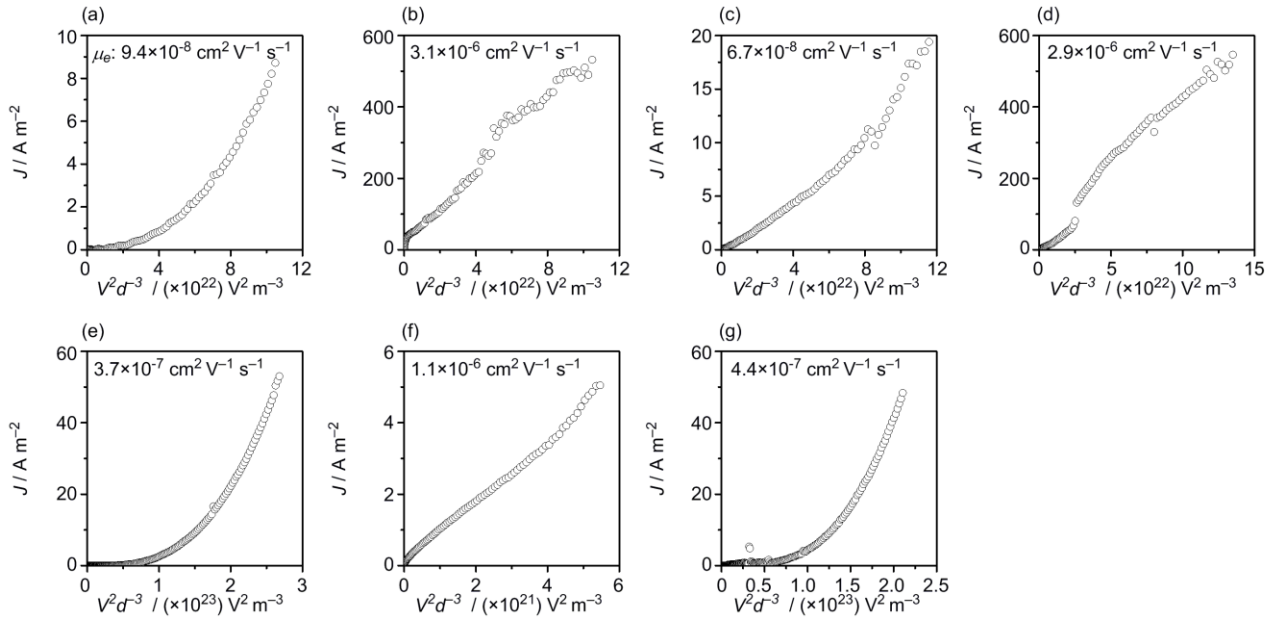

Figure 3.10. J–V^2d^{-3} characteristics of electron-only device for (a) **Ph-H**, (b) **Ph-D**, (c) **Ph-EH**, (d) **Ph-MH**, (e) **Ph-Ipop**, (f) **Th-EH**, and (g) **Py-EH** films.

Table 3.3. Field-effect mobilities of **Ph-EH**-based FET devices and contact angle data of **Ph-EH** films.

condition	substrate treatment	T_a [°C]	μ_e [cm^2 V^{-1} s^{-1}]	θ_{water} [°]	$\theta_{glycerol}$ [°]	γ^d [mJ cm^{-2}]	γ^p [mJ cm^{-2}]	SFE [mJ cm^{-2}]
1	bare	as spun	no FET	104.92	87.34	25.4	0.2	25.6
2	HMDS	as spun	1.7×10^{-7}	101.98	88.93	18.0	1.6	19.6
3	ODTS	as spun	8.7×10^{-7}	100.39	89.12	15.5	2.6	18.1
4	ODTS	160	5.4×10^{-6}	99.03	90.37	12.0	4.2	16.1

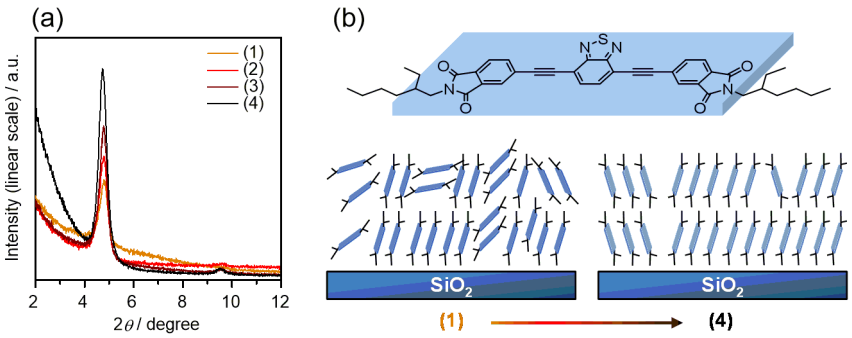

Figure 3.11. (a) Out-of-plane X-ray diffractograms of **Ph-EH**-based films coated on (1) bare SiO_2, (2) HMDS-modified SiO_2, (3) ODTS-modified SiO_2, and (4) thermally annealed film of (3). (b) Graphical representation of the molecular orientation in conditions (1) and (4).

analyses. As shown in Table 3.3 and Figure 3.11 (a), the electron mobilities gradually increased with the intensity of the diffraction peak at 4.7°. From this result, it can be inferred that **Ph-EH** takes edge-on alignment varying between partially disordered state (condition (1)) and well-ordered state (condition (4)) as graphically represented in Figure 3.11 (b), depending on the fabricating conditions.

To further elucidate this relationship, the SFE of the **Ph-EH** films was estimated from the contact-angle measurements using H_2O (θ_{water}) and glycerol ($\theta_{glycerol}$) as probe liquids. According to the theory of Kaelble and Uy,[4] the SFE of a compound in the film state can be expressed as a sum of contributions from γ^d and polar (γ^p) components of their interfacial energies. The observed contact-angles as well as the estimated SFE, γ^d, and γ^p values are given in Table 3.3. The analysis of the SFE components together with XRD data (Figure 3.11 (a)) reveals that the value of γ^d decreases monotonously with the intensity of the diffraction peak; γ^p showed a reverse trend. It is generally established that the values of γ^d and γ^p originate from the polarizability and permanent dipole, respectively,[5] and that these values are mainly influenced by the chemical group at the surface. Since the polarizability of a π -conjugated framework is larger than an alkyl group, a higher γ^d indicates an increase of the amount of π -conjugated backbone exposed to the surface. This interpretation is consistent with the molecular arrangements in the film state, i.e., the higher γ^d is observed in edge-on alignment with concomitant disordered state in condition (1). In addition, the calculated electrostatic potential (ESP) of π-conjugated backbone of PH-Me showed that the localized negative charges are located on the carbonyl groups (Figure 3.7), which indicates that the alignment of the carbonyl groups to the surface tend to increase the γ^p value in well-ordered edge-on state, such as condition (4). Therefore, we concluded that γ^d, γ^p, field-effect μ_e, and the diffraction intensities in out-of-plane XRD measurements show a strong correlation among them.

3.5 Photovoltaic Performances

In order to assess the effect of the alkyl chains and the terminal arene-imide units on the photovoltaic performance, BHJ-type photovoltaic devices were fabricated, which contained the compounds synthesized in this work as an acceptor with P3HT as a donor material; the OPV device was characterized by the conventional structure of ITO/PEDOT:PSS/active layer/Ca/Al. The active layers were prepared by spin-coating from their blended solutions.

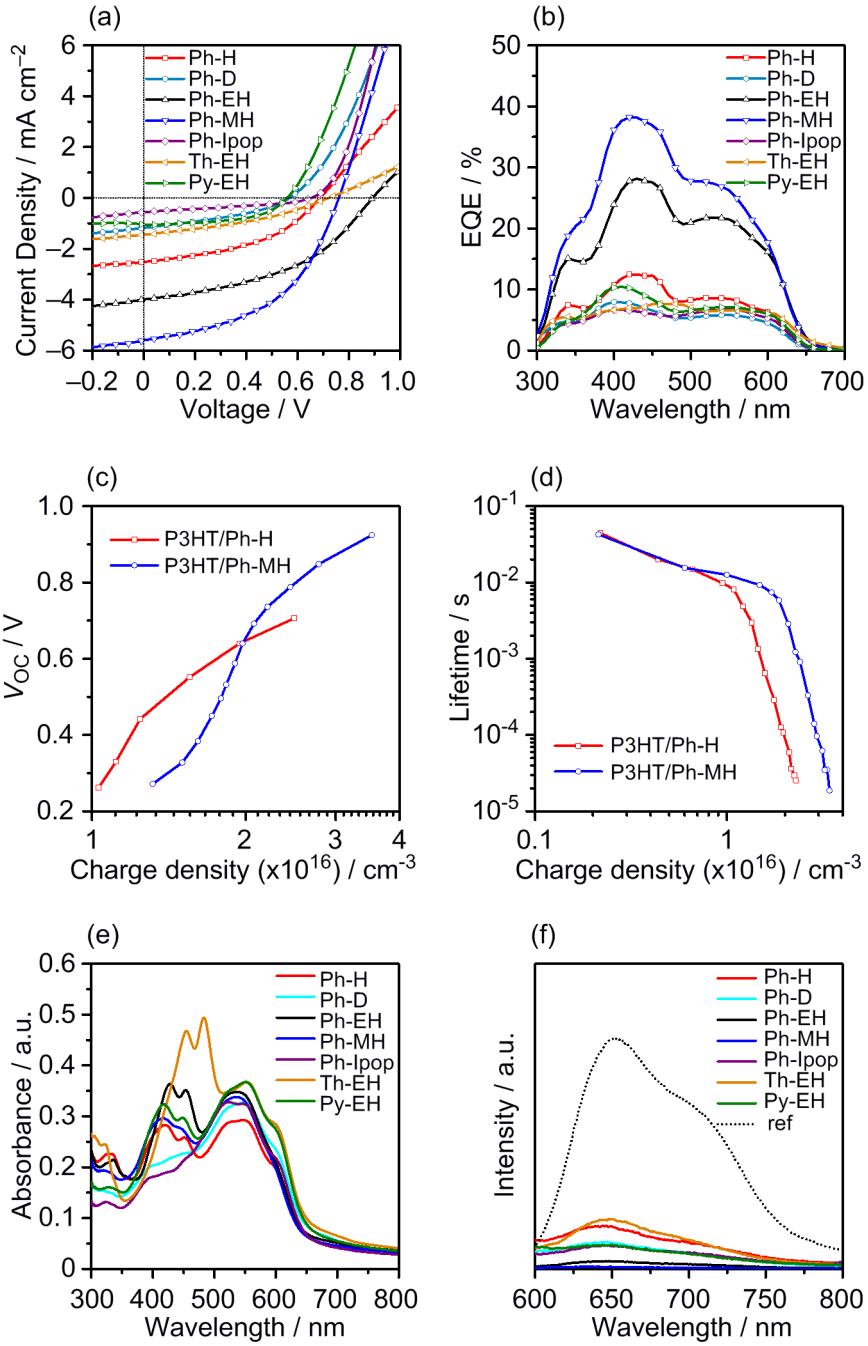

Figure 3.12. (a) *J*-*V* curves and (b) EQE spectra of the optimized P3HT/acceptor OPV devices. (c) Plot of open circuit voltage vs. charge density and (d) recombination lifetime vs. charge density for OPV devices prepared from P3HT/**Ph-H** (red), P3HT/**Ph-MH** (blue). (e) UV-Vis absorption spectra of the P3HT/acceptor blend films. (f) Fluorescence spectra of the P3HT/acceptor blend films.

The fabrication optimization of the active layer was con-ducted by varying the blending ratio, concentration, processing solvents, and thermal annealing temperatures. The *J*–*V* characteristics of devices under AM 1.5 G solar irradiation (100 mW cm^{-2}) are shown in Figure 3.12 (a) and Figure S3.1. The optimized conditions and the relevant solar cell parameters extracted from *J*–*V* curves are listed in Tables S3.1–S3.7 and Table 3.4, respectively. All

Table 3.4. OPV characteristics and properties of blend films.

blend films	J_{SC} [mA cm^{-2}]	V_{OC} [V]	FF	PCE [%]	PLQE [%]	μ_e [cm^2 V^{-1} s^{-1}]	μ_h [cm^2 V^{-1} s^{-1}]
P3HT/**Ph-H**	2.52	0.69	0.44	0.77	82	8.4×10^{-7}	9.0×10^{-6}
P3HT/**Ph-D**	1.03	0.51	0.31	0.16	88	6.0×10^{-6}	1.0×10^{-5}
P3HT/**Ph-EH**	3.99	0.89	0.45	1.58	97	1.1×10^{-6}	2.3×10^{-5}
P3HT/**Ph-MH**	5.59	0.76	0.48	2.05	99	3.7×10^{-6}	9.3×10^{-6}
P3HT/**Ph-Ipop**	0.55	0.66	0.29	0.11	89	1.2×10^{-6}	1.6×10^{-5}
P3HT/**Th-EH**	1.44	0.72	0.36	0.38	78	2.0×10^{-7}	8.4×10^{-6}
P3HT/**Py-EH**	1.44	0.47	0.42	0.32	90	1.1×10^{-5}	7.0×10^{-6}

devices showed a typical photovoltaic conversion phenomenon, indicating that these compounds function as acceptors. Their PCEs varied between 0.11% and 2.05%, depending on the structure of acceptors. The highest PCE (2.05%) with an V_{OC} of 0.76 V, a short-circuit current density J_{SC} of 5.59 mA cm^{-2}, and a FF of 0.48 was obtained for the device employing **Ph-MH** as an acceptor. The EQE measurements showed that all devices exhibit a broad photoresponse between 300 and 650 nm (Figure 3.12 (b)). In particular, the photocurrent at wavelength regions of 300~450 nm and 450~600 nm can be attributed to the absorption of the acceptor material and P3HT, respectively (Figures 3.4 and S2). This finding clearly indicates that both the donor and acceptor materials contribute to the photocurrent generation. We preliminary investigated the inverted OPV devices using P3HT/**Ph-MH** composite and obtained the PCE of 1.88% (Figures 3.13), indicating that **Ph-MH** possesses applicability against device structures. One major variedness was found in the V_{OC} values. Although it has been commonly suggested that the V_{OC} values of OPV devices strongly depend on the energy gap between the HOMO level of donor and the LUMO level of acceptor, no such correlation was found in the studied devices.

In order to gain an insight into the origin of the V_{OC} differences, charge-extraction measurements were conducted on P3HT/**Ph-MH** and P3HT/**Ph-H** devices. The dependence of the V_{OC} on the charge densities of devices is displayed in Figure 3.12 (c). The difference in the V_{OC} values between the two solar cells at the matched charge

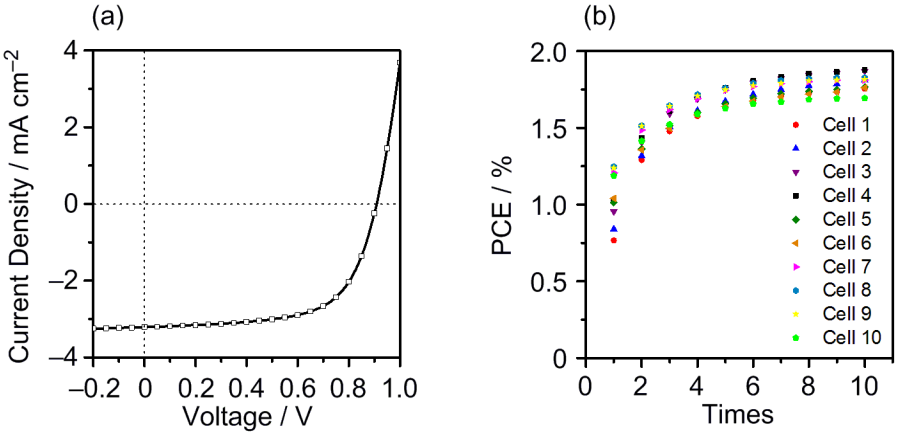

Figure 3.13. (a) *J*–*V* curve inverted type OPV device with a structure of ITO/TiO_x/P3HT:**Ph-MH**/MoO_x/Ag[6] and (b) repeated PCEs characteristics of ten OPV devices.

density could be caused by the difference in the gaps be-tween the energy levels of acceptor and donor materials, in trap density and distribution, and in the formation of dipole layer at the interface of acceptor and donor materials. Since the LUMO levels of the acceptors are almost the same, the difference in Figure 3.12 (c) should be caused by different trap and/or interface dipole conditions. Higher trap density may be expected from amorphous materials such as **Ph-MH**. However, the solar cells using **Ph-MH** showed higher V_{OC} values at high charge concentration region, implying less trap density in the device.[7] Therefore, the high V_{OC} values of the solar cells using **Ph-MH** seems to be caused partially by desired dipole layer formed at the interface.[8] The dependence of charge lifetime on charge density is shown in Figure 3.12 (d). The charge lifetime of P3HT/**Ph-MH** device is longer than that of P3HT/**Ph-H** device at any given charge densities. Thus, the long life-time (i.e. slow charge recombination) of P3HT/**Ph-MH** device is another factor for the large V_{OC} values. The longer lifetime of the P3HT/**Ph-MH** device is worthy of remark because the device may have larger driving force for the charge recombination owing to larger difference in p-type HOMO and n-type LUMO energy levels caused by the desired interface layer. The slow charge recombination might be obtained by a spatial gap at the inter-face between P3HT and acceptors, which would be formed by the branched alkyl chains. The gap would de-crease the interfacial charge transfer probability.

Meanwhile, interestingly, we found that the acceptor molecules with relatively higher field-effect electron mobilities (i.e. **Ph-H**, **Ph-D**, **Th-EH**, and **Py-EH**) were characterized by poor PCEs, which is primarily due to a decrease in J_{SC}. This in turn means that the FET mobility is not directly associated with J_{SC}. Further evidence for this important point can be found by comparing the EQE spectra of the devices. As shown in Figure 3.12 (b), the device containing **Ph-MH** showed a maximum in EQE equal to 38% at 420 nm (to compare with 28% and 12% of **Ph-EH** and **Ph-H**, respectively). Considering that a large difference of J_{SC} values was found for both the Ph-X (X = H, D, EH, MH, and Ipop) and Ar-EH (Ar = Ph, Th, and Py) series, it can be inferred that both the structure of solubilizing alkyl groups and terminal arene-imide units exert a significant influence on the photovoltaic performance.

3.6 Discussions of Photocurrent Generation

It has been suggested that the EQE of organic solar cells mainly depends on the following five efficiency factors: incident photon absorption (η_{Abs}), the exciton diffusion to the donor-acceptor interface (η_{ED}), the charge transfer at the interface (η_{CT}), the charge separation into the free carrier (η_{CS}), and the charge collection to the electrode (η_{CC}) (Figure 1).[9] In order to clarify the relevance of these factors to the OPV performance of our compounds, we collected UV-Vis absorption and photoluminescence spectra of blended films, which were prepared on quartz plates under identical conditions of optimized active layers in OPVs. As shown in Figure 3.12 (e), all blend films did not show much difference in absorbance and spectral shape. Thus, the η_{Abs} is virtually the same for the P3HT/Ph-X (X = H, D, EH, MH, and Ipop) and P3HT/Ar-EH (Ar = Ph, Th, and Py) series. Photoluminescence spectra of the blend films along with P3HT pristine film, normalized by the fractions of their absorbed photons on excitation at the maximum absorption of the long wave-length region (500~550 nm), are shown in Figure 3.12 (d). The PL of all blend films is almost quenched, whereas an intense fluorescence was found for pristine P3HT, which may be explained by the photo-induced charge-transfer from P3HT to the acceptors. As displayed in Table 3.4, the PL quenching efficiencies (PLQEs) of the blended films relative to the PL intensity of P3HT films are calculated to be between 78% and 99%,

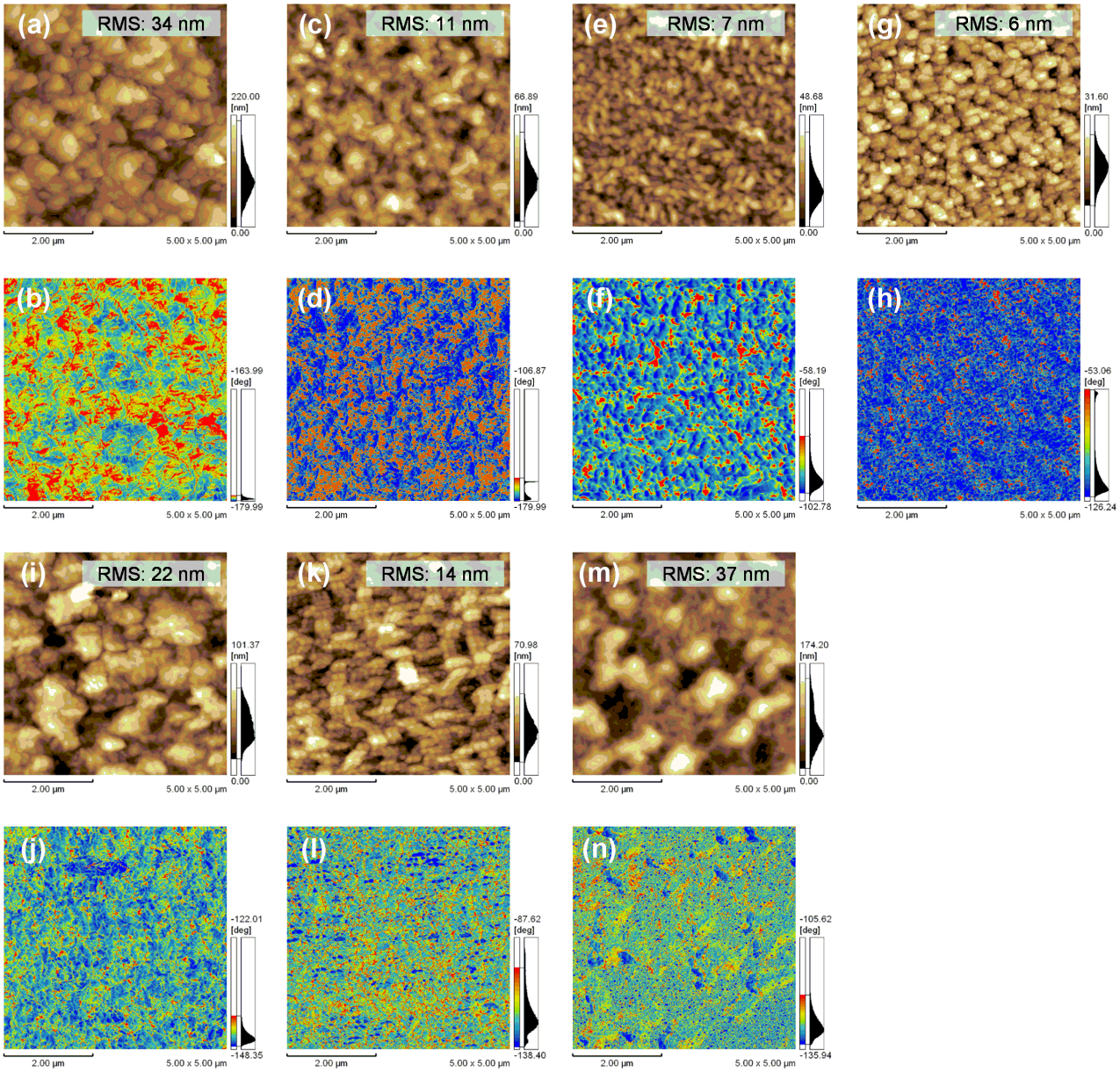

Figure 3.14. AFM height and phase images of (a, b) P3HT/**Ph-H**, (c, d) P3HT/**Ph-D**, (e, f) P3HT/**Ph-EH**, (g, h) P3HT/**Ph-MH**, (i, j) P3HT/**Ph-Ipop**, (k, l) P3HT/**Th-EH**, and (m, n) P3HT/**Py-EH** blend films.

suggesting that η_{ED} and η_{CT} possess high efficiencies in all blend films. In addition, since the ratio of the difference in PLQEs are not significant compared with that in PCEs, we concluded that η_{ED} and η_{CT} are not the relevant factors in determining a high photovoltaic performance for the studied compounds. Nevertheless, further comparison of PLQEs and PCEs showed that quantitative PLQEs for P3HT/**Ph-MH** and P3HT/**Ph-EH** films may contribute to some extent in increasing the PCEs. This is indeed in line with AFM measurements showing that the surface of P3HT/**Ph-MH** and P3HT/**Ph-EH** films is characterized by relatively small grains (Figure 3.14).

Finally, the η_{CC} values were evaluated using the SCLC technique with the device structures of ITO/TiOx/active layer/Ca/Al and ITO/PEDOT:PSS/active layer/Au for electron and hole only devices, respectively.[10] The estimated

electron and hole mobilities are listed in Table 3.4. In particular, the hole mobility varies within narrow range, between 7.0×10^{-6} and 2.3×10^{-5} cm^2 V^{-1} s^{-1}, whereas the electron mobilities exhibit larger deviations, between 2.0×10^{-7} and 1.1×10^{-5} cm^2 V^{-1} s^{-1}. For all studied compounds, except for P3HT/**Py-EH** film, the hole mobility is higher than the corresponding electron mobility. It is established that a high carrier mobility and/or a balanced distribution between hole and electron mobilities in blend films are favorable properties in order to achieve a high PCE.[11] However, such a trend was not observed in our system; no clear correlation between carrier mobilities and PCEs was found, implying that η_{CC} is not the dominant factor.

Considering these data, we concluded that the η_{CS} may be the factor that determines the PCEs of our systems and mainly ascribed to the charge-separation into the free carrier at the donor–acceptor interfaces. As indicated in chapter 2, the analysis of SFE of each material may provide us with further information in bulk heterojunction OPVs. In this study, a qualitative analysis was performed by plotting the estimated γ^d versus the J_{SC} in OPV device (Figure 3.15 and Table S3.8). Under the same measurement conditions, the γ^d values of P3HT and $PC_{61}BM$ were estimated to be 5.4 and 32.4 mJ cm^{-2}, respectively. This plot indicates the presence of correlation between γ^d and J_{SC}. Previously, we concluded that the small difference of SFE between P3HT and an amorphous acceptor (**S-Ph-EH**) resulted in the high miscibility, which disturbed the formation of phase-separated nanomorphology in the blend films. On the other hand, the acceptors having small γ^d used in this study showed the crystalline characteristics.

In fact, apparent grains were observed from AFM images (Figure 3.14). Thus, the small γ^d molecules take well-ordered state in the blend film, which results in the dis-advantage morphology for charge-separation (Figure 3.15 (b)). In contrast, the acceptors with a large γ^d tend to increase the amount of exposed π-conjugated framework to the phase interface between the acceptor and P3HT, which can promote the formation of desirable charge-separated states. Since the spherical structure of fullerene derivatives can directly face their π-conjugated framework to the donor materials, this result provides a solid strategy to build the ideal interface between donor and non-fullerene acceptors. Finally, our results demonstrated that the preparation of novel non-fullerene acceptor materials should take into account not only the molecular electronic features but also the properties of the films, such as the γ^d component of the interfacial energies.

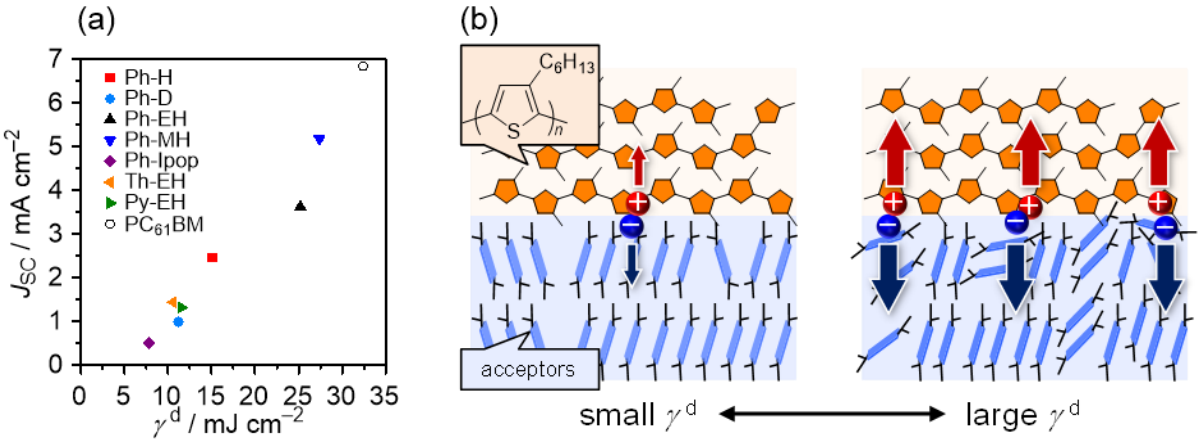

Figure 3.15. (a) Plot of γ^d vs. J_{SC} values for acceptor materials used in this study. (b) Graphical representation of the molecular orientation at donor/acceptor interface.

3.7 Conclusion

In order to establish a successful design strategy to fine-tune the interface between donor and acceptor in the BHJ films, the author have synthesized a series of non-fullerene acceptor materials having electron-withdrawing benzothiadiazole and arenedicarboximide as central and terminal units, respectively, with varied terminal alkyl groups. In contrast to the photophysical properties of the compound in a solution, those in the film state strongly depended on the terminal alkyl groups, which correlated to the crystallinity of the com-pounds. Electrochemical analysis of the compounds revealed that the LUMO energy levels ranged between –3.31 and –3.42 eV. As a consequence of the low-lying LUMO energy levels, all compounds exhibited a typical electron-transporting semiconducting behavior in solution-processed OFET devices. The comparison of XRD and SFE measurements of **Ph-EH** films showed that the crystallinity of the compounds in the film state well correlates with the γ^{d} and γ^{p} components of their interfacial energies. Bulk-heterojunction OPV devices fabricated from these acceptors in combination with P3HT as a donor showed suitable photovoltaic characteristics, and the best PCE was measured to 2.05%. The OPV performance was significantly influenced by the terminal alkyl substitutions and/or arene-imide units of the studied acceptors. To further explore this point, absorption, photoluminescence, and carrier mobility measurements of blend films were performed. These provided a clear understanding of the charge-separation into the free carriers at the donor–acceptor interfaces, which is the key process that determines the photovoltaic performance of the studied compounds. It was found that the J_{SC} of OPV devices shows a strong correlation with γ^{d} of the acceptors, i.e., the J_{SC} increases with γ^{d}. These results suggested that the introduction of sterically bulky terminal groups in linear π-conjugated systems produce a positive effect on the charge-separation process at the donor–acceptor interfaces in BHJ films. This phenomenon can be explained by the fact that the increased amorphous behavior contributes to increasing the amount of exposed π-conjugated framework to the grain surface. This approach should thus be considered as a promising step towards the successful development of non-fullerene acceptors for OPVs.

3.8 Experimental Section

Supplemental Figures and Tables

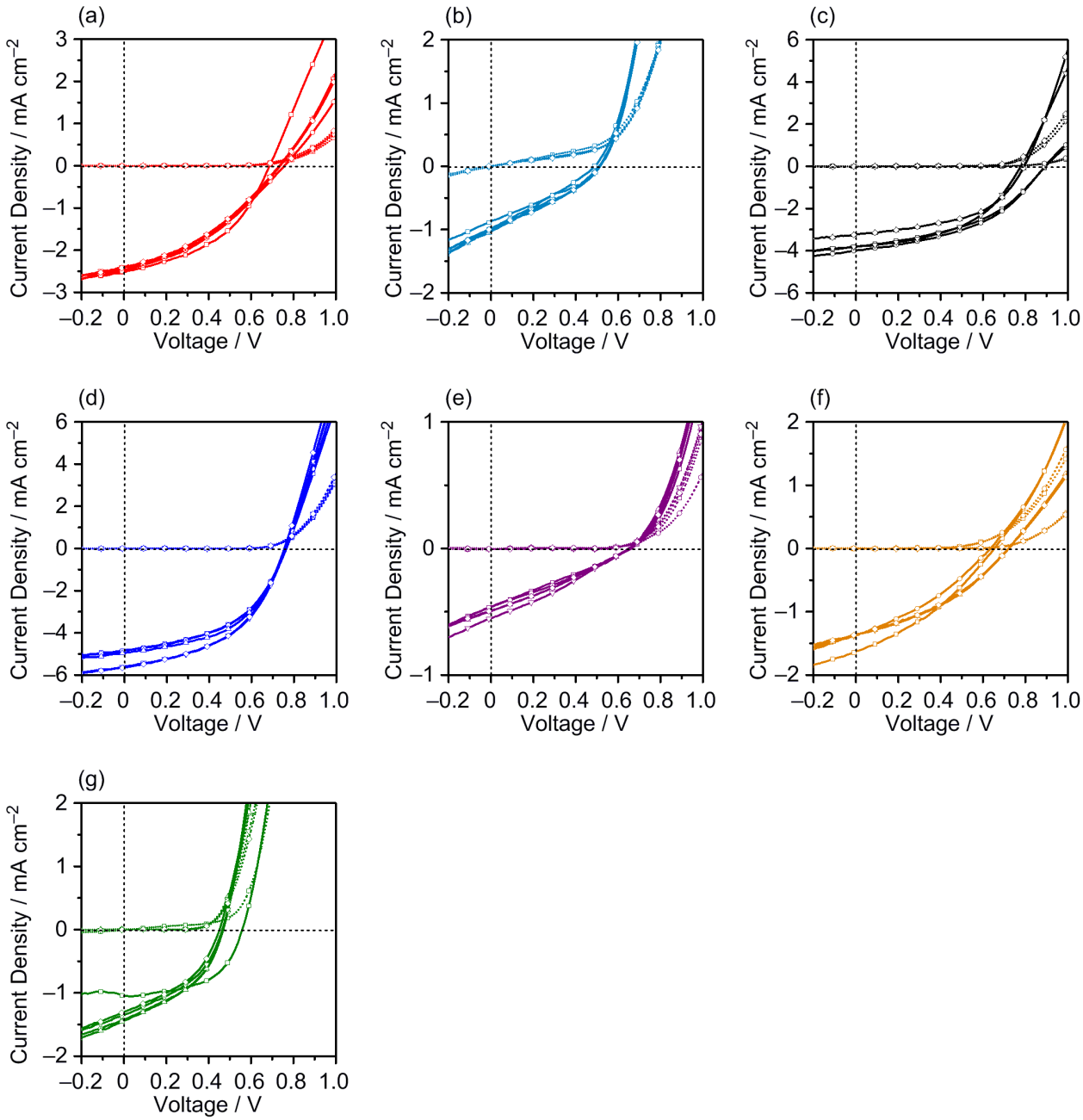

Figure S3.1. *J–V* curves of OPV devices for (a) P3HT/**Ph-H**, (b) P3HT/**Ph-D**, (c) P3HT/**Ph-EH**, (d) P3HT/**Ph-MH**, (e) P3HT/**Ph-Ipop**, (f) P3HT/**Th-EH**, and (g) P3HT/**Py-EH** films.

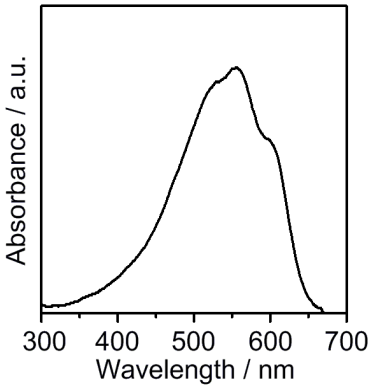

Figure S3.2. UV-Vis absorption spectrum of P3HT film.

Table S3.1. OPV performance based on P3HT/**Ph-H** films.

Run	V_{OC} [V]	J_{SC} [mA cm^{-2}]	FF	PCE [%]
1	0.69	2.52	0.44	0.77
2	0.76	2.47	0.36	0.68
3	0.74	2.43	0.37	0.70
4	0.73	2.40	0.37	0.65
5	0.74	2.42	0.36	0.64
average	0.73 ± 0.01	2.45 ± 0.02	0.38 ± 0.02	0.69 ± 0.02

The fabrication conditions of the active BHJ layer were optimized: the blend composition of a 1:1.5 weight ratio of P3HT:**Ph-H**, a concentration of 20 mg mL^{-1} in CB for spin-coating, and with thermal annealing at 110 °C for 10 min under N_2.

Table S3.2. OPV performance based on P3HT/**Ph-D** films.

Run	V_{OC} [V]	J_{SC} [mA cm^{-2}]	FF	PCE [%]
1	0.49	0.87	0.31	0.13
2	0.51	0.98	0.27	0.14
3	0.51	1.03	0.31	0.16
4	0.51	1.01	0.31	0.16
5	0.51	0.99	0.32	0.16
average	0.51 ± 0.00	0.98 ± 0.03	0.30 ± 0.01	0.15 ± 0.01

The fabrication conditions of the active BHJ layer were optimized: the blend composition of a 1:1 weight ratio of P3HT:**Ph-D**, a concentration of 20 mg mL^{-1} in *o*-DCB for spin-coating, and without thermal annealing.

Table S3.3. OPV performance based on P3HT/**Ph-EH** films.

Run	V_{OC} [V]	J_{SC} [mA cm^{-2}]	FF	PCE [%]
1	0.90	3.80	0.44	1.50
2	0.89	3.99	0.45	1.58
3	0.80	3.26	0.50	1.29
4	0.78	3.81	0.48	1.42
5	0.79	3.23	0.50	1.28
average	0.83 ± 0.03	3.62 ± 0.16	0.47 ± 0.01	1.41 ± 0.06

The fabrication conditions of the active BHJ layer were optimized: the blend composition of a 1:1 weight ratio of P3HT:**Ph-EH**, a concentration of 20 mg mL^{-1} in CB for spin-coating, and without thermal annealing.

Table S3.4. OPV performance based on P3HT/**Ph-MH** films.

Run	V_{OC} [V]	J_{SC} [mA cm^{-2}]	FF	PCE [%]
1	0.76	4.83	0.48	1.79
2	0.76	4.85	0.49	1.79
3	0.76	4.95	0.50	1.88
4	0.75	5.64	0.48	2.04
5	0.76	5.59	0.48	2.05
average	0.76 ± 0.00	5.17 ± 0.18	0.49 ± 0.00	1.91 ± 0.06

The fabrication conditions of the active BHJ layer were optimized: the blend composition of a 1:1 weight ratio of P3HT:**Ph-MH**, a concentration of 10 mg mL^{-1} in $CHCl_3$ for spin-coating, and without thermal annealing.

Table S3.5. OPV performance based on P3HT/**Ph-Ipop** films.

Run	V_{OC} [V]	J_{SC} [mA cm^{-2}]	FF	PCE [%]
1	0.66	0.46	0.27	0.08
2	0.66	0.46	0.29	0.09
3	0.65	0.50	0.29	0.09
4	0.66	0.55	0.29	0.11
5	0.66	0.49	0.29	0.09
average	0.66 ± 0.00	0.49 ± 0.02	0.29 ± 0.00	0.09 ± 0.01

The fabrication conditions of the active BHJ layer were optimized: the blend composition of a 1:1 weight ratio of P3HT:**Ph-Ipop**, a concentration of 20 mg mL^{-1} in *o*-DCB for spin-coating, and without thermal annealing.

Table S3.6. OPV performance based on P3HT/**Th-EH** films.

Run	V_{OC} [V]	J_{SC} [mA cm^{-2}]	FF	PCE [%]
1	0.65	1.62	0.34	0.37
2	0.64	1.37	0.34	0.29
3	0.72	1.44	0.36	0.38
4	0.72	1.37	0.36	0.36
5	0.72	1.36	0.37	0.36
average	0.69 ± 0.02	1.43 ± 0.05	0.35 ± 0.01	0.35 ± 0.02

The fabrication conditions of the active BHJ layer were optimized: the blend composition of a 1:1 weight ratio of P3HT:**Th-EH**, a concentration of 20 mg mL^{-1} in *o*-DCB for spin-coating, and without thermal annealing.

Table S3.7. OPV performance based on P3HT/**Py-EH** films.

Run	V_{OC} [V]	J_{SC} [mA cm^{-2}]	FF	PCE [%]
1	0.56	1.04	0.54	0.32
2	0.47	1.43	0.42	0.28
3	0.47	1.44	0.42	0.28
4	0.46	1.35	0.41	0.26
5	0.45	1.30	0.41	0.24
average	0.48 ± 0.02	1.31 ± 0.07	0.44 ± 0.03	0.28 ± 0.01

The fabrication conditions of the active BHJ layer were optimized: the blend composition of a 1.5:1 weight ratio of P3HT:**Py-EH**, a concentration of 20 mg mL^{-1} in *o*-DCB for spin-coating, and without thermal annealing.

Table S3.8. Contact angles and calculated surface free energy data of acceptor films.

Compounds	θ_{water} [°]	$\theta_{glycerol}$ [°]	γ^d [mJ cm^{-2}]	γ^p [mJ cm^{-2}]	SFE [mJ cm^{-2}]
Ph-H	101.16	90.0	15.1	2.5	17.6
Ph-D	102.84	94.03	11.2	3.2	14.3
Ph-EH	101.1	84.3	25.2	0.7	25.9
Ph-MH	97.6	80.4	27.4	0.1	28.4
Ph-Ipop	82.0	79.5	7.8	15.9	23.7
Th-EH	105.5	96.6	10.6	2.6	13.2
Py-EH	101.3	92.5	11.5	3.5	15.0
P3HT	107.2	102.6	5.4	4.3	9.7
$PC_{61}BM$	84.9	67.1	32.4	3.4	35.8

General Information

Column chromatography was performed on silica gel, KANTO Chemical silica gel 60N (40–50 μm). TLC plates were visualized with UV light. Preparative GPC was performed on a Japan Analytical Industry LC-918 equipped with JAI-GEL 1H/2H. ^{1}H and ^{13}C NMR spectra were recorded on a JEOL ECS-400 spectrometer in $CDCl_3$ with TMS as an internal standard. Data are reported as follows: chemical shift in ppm (δ), multiplicity (s = singlet, d = doublet, t = triplet, m = multiplet, br = broad), coupling constant (Hz), and integration. Mass spectra were obtained on a Shimadzu GCMS-QP-5050 or Shimadzu AXIMA-TOF. DSC and TGA were performed under nitrogen at a heating rate of 10 °C min^{-1} with a Shimadzu DSC-60 and a Shimadzu TGA-50, respectively. UV-Vis spectra were recorded on a Shimadzu UV-3600 spectrophotometer. Fluorescence spectra were recorded using a Fluoromax-4 spectrometer in the photo-counting mode equipped with a Hamamatsu R928P photomultiplier. The bandpass for the emission spectra was 1.0 nm. All spectra were obtained in spectrograde solvents. CV was carried out on a BAS CV-620C voltammetric analyzer using a platinum disk as the working electrode, platinum wire as the counter electrode, and $Ag/AgNO_3$ as the reference electrode at a scan rate of 100 mV s^{-1}. Elemental analyses were performed on Perkin Elmer LS-50B by the Elemental Analysis Section of CAC, ISIR, Osaka University. The surface structures of the deposited organic films were observed by atomic force microscopy (Shimadzu, SPM9600), and the film crystallinity was evaluated by an X-ray diffractometer (Rigaku, SmartLab). X-ray diffraction patterns were obtained using Bragg-Brentano geometry with CuKα radiation as an X-ray source with an acceleration voltage of 45 kV and a beam current of 200 mA. The scanning mode was set to 2θ scans between 3º–30º with scanning steps of 0.01º.

OFET Device Fabrication and Evaluation

The field-effect mobility was measured using bottom-contact thin-film FET geometry. The p-doped silicon substrate functions as the gate electrode. A thermally grown silicon oxide dielectric layer on the gate substrate was 300 nm thick with a capacitance of 10.0 nF cm^{-2}. Interdigital source and drain electrodes were constructed with gold (30 nm) that were formed on the SiO_2 layer. The W and L were 294 mm and 25 μm, respectively. The silicon oxide surface was washed with toluene, acetone, water, and 2-propanol and the silicon oxide surface was then activated by ozone treatment. This substrate was used for condition (1). The ODTS-modified substrates were prepared by 1.0 wt% ODTS toluene solution under N_2 at 60 °C for 1 h. This substrate was used for condition (3). For the HMDS-modification (condition (2)), the Si/SiO_2 substrates were immersed in 1.0 wt% HMDS toluene solution under N_2 at 60 °C for 1 h. Then all the substrates were washed again with toluene, acetone, water, and 2-propanol. The semiconductor layer was spin-casted on the Si/SiO_2 substrates from 10 mg mL^{-1} $CHCl_3$ solution. Thermal annealing was conducted for 1 h under a vacuum condition (10^{-2} Pa). The characteristics of the OFET devices were measured at room temperature under a pressure of 10^{-3} Pa. The current–voltage characteristics of devices were measured by using a KEITHLEY 4200SCS semiconductor parameter analyzer. The μ_e was calculated in the saturated region at the source-drain voltage of 100 V and the current I_{on}/I_{off} ratio was determined from the I_{SD} at V_{SG} = 0 V (I_{off}) and V_{SG} = 100 V (I_{on}) by the following equation.

$$I_{DS} = \frac{W}{2L} C_i \mu (V_{GS} - V_{th})^2$$

OPV Device Fabrication and Evaluation

Organic photovoltaic devices were prepared with a structure of ITO/PEDOT:PSS/active layer/Ca/Al. ITO-coated glass substrates were first cleaned by ultrasonication in toluene, acetone, H_2O, and 2-propanol for 10 min, respectively. ITO-coated glass substrates were then activated by ozone treatment for 1 h. PEDOT:PSS was spin-coated on the ITO surface at 3000 rpm for 1 min and dried at 135 °C for 10 min. The active layers were then prepared by spin-coating on the ITO/PEDOT:PSS electrode at 1000 rpm for 2 min in a glove box. The typical thickness of the active layer was 90–110 nm. Ca and Al electrode were evaporated on the top of active layer through a shadow mask to define the active area of the devices (0.09 cm^2) under a vacuum of 10^{-5} Pa to a thickness of 30, 100 nm determined by a quartz crystal monitor. After sealing the device from the air, the photovoltaic characteristics were measured in air under simulated AM 1.5G solar irradiation (100 mW cm^{-2}) (SAN-EI ELECTRIC, XES-301S). The current–voltage characteristics of photovoltaic devices were measured by using a KEITHLEY 2400 source meter. The EQE spectra were measured by using a Soma Optics Ltd. S-9240. The thickness of active layer was determined by KLA Tencor Alpha-step IQ.

Charge Density Measurements

Photo-generated charge densities of the photovoltaic devices were measured by charge extraction method. The device, a nanosecond response switch (SR-05 Asama Lab, Japan), and an oscilloscope with 50 Ohm internal resistance were connected in series. The device was initially irradiated by a diode laser (Cube, Coherent, 641 nm) at open circuit condition. The timing to turn off the laser and to switch the circuit to short circuit was controlled by a delay generator (Stanford Research Systems, DG645). When the laser was turned off, the switch was simultaneously turned on to short circuit condition. Then accumulated charges at open circuit condition were flowing out to external circuit. The current was measured on the oscilloscope and integrated numerically on a PC. Charge density was obtained by dividing the integrated charges by the volume of the active layer. The open circuit voltage versus charge density plot was obtained by repeating the measurement with different laser intensities. Charge extraction measurement was also performed with different delay times between the timings of turning off the laser and turning on the switch. Recombination lifetime was obtained from the slope of the plot of the charge density versus delay time.

SCLC Measurements

Hole-only and electron-only devices were prepared with a structure of ITO/PEDOT:PSS/active layer/Au and ITO/TiO_x/active layer/Ca/Au, respectively. The active layers were prepared from 20 mg mL^{-1} solution of materials in $CHCl_3$. The carrier mobilities of these devices were calculated by the following equation:

$$J = \frac{9}{8}\varepsilon\varepsilon_0\mu\frac{V^2}{d^3}$$

where ε, ε_0, μ, and d are the dielectric constant of the active layer, the permittivity of free space, the carrier mobility, and the measured thickness of active layer, respectively. We used the values of $\varepsilon = 3$, $\varepsilon_0 = 8.8 \times 10^{-12}$ F/m.

Surface Free Energy Estimation

The contact angles of film surface were measured by a NiCK LSE-ME1 using distilled water and glycerol. SFEs were estimated based on the theory established by Kaelble and Uy.

PLQE Estimation

Blended films were prepared on the quartz substrate by spin-coating under identical condition of optimized active layers in OPVs. PLQE of blended films were calculated using following equation:

$$\mathrm{PLQE} = 1 - \frac{\phi_{p:n}}{\phi_p}$$

where Φ_p and $\Phi_{p:n}$ are the normalized photoluminescence intensities of reference and blended films at λ_{max}, respectively.

Materials

All reactions were carried out under a nitrogen atmosphere. Solvents of the highest purity grade were used as received. Unless stated otherwise, all reagents were purchased from commercial sources and used without purification. 2-bromothieno[2,3-*c*]furan-4,6-dione was prepared by our previously reported procedure.[12] 5-bromo-2-hexylisoindoline-1,3-dione (**15**), 6-bromo-2-(2-ethylhexyl)-1*H*-benzo[*de*]isoquinoline-1,3(2*H*)-dione (**21**) and 3-bromofuro[3,4-*b*]pyridine-5,7-dione were prepared by reported procedures, and ^{1}H NMR data of these compounds were in agreement with those previously reported.[13]

Synthesis

*Synthesis of **16***: 4-Bromophthalic anhydride (4.00 g, 17.6 mmol) and 1-dodecylamine (3.26 g, 17.6 mmol) were placed in a round-bottomed flask and dissolved with DMF (100 mL). The reaction mixture was stirred at 140 °C for 12 h. After being cooled to room temperature and addition of water, the resulting mixture was extracted with ethyl acetate (EtOAc) and the organic layer was washed with water. After removal of the solvent under reduced pressure, the residue was purified by column chromatography on silica gel (hexane/EtOAc = 10/1) to give **16** (4.74 g, 68%). Colorless solid; m.p.: 63-64 °C; ^{1}H NMR (400 MHz, $CDCl_3$, TMS, δ): 7.97 (d, J = 1.4 Hz, 1H), 7.85 (dd, J = 8.0, 1.6 Hz, 1H), 7.70 (d, J = 8.0 Hz, 1H), 3.66 (t, J = 7.3 Hz, 2H), 1.65 (m, 2H), 1.35-1.23 (br, 16H), 0.88 (t, J = 6.6 Hz, 3H); ^{13}C NMR (100 MHz, $CDCl_3$, δ): 167.54, 166.99, 136.79, 133.81, 130.69, 128.71, 126.51, 124.51, 38.30, 31.91, 29.62, 29.62, 29.59, 29.49, 29.35, 29.18, 28.52, 26.84, 22.69, 14.14; MS (GC) *m/z* 393 (M^+, Calcd 393.13). Anal. calcd for $C_{20}H_{28}BrNO_2$: C 60.91, H 7.16, N 3.55; found: C 60.82, H 7.06, N 3.42.

*Synthesis of **17***: 4-Bromophthalic anhydride (5.00 g, 22.0 mmol) and 2-aminoheptane (2.50 g, 22.0 mmol) were placed in a round-bottomed flask and dissolved with DMF (100 mL). The reaction mixture was stirred at 145 °C for 12 h. After being cooled to room temperature and addition of water, the resulting mixture was extracted with EtOAc and the organic layer was washed with water. After removal of the solvent under reduced pressure, the residue was purified by column chromatography on silica gel (hexane/EtOAc = 4/1) to give **17** (3.60 g, 50%). Colorless solid;

m.p.: 84-85 °C; ^{1}H NMR (400 MHz, $CDCl_3$, TMS, δ): 7.95 (d, J = 1.8 Hz, 1H), 7.84 (dd, J = 7.8, 1.8 Hz, 1H), 7.68 (d, J = 7.8 Hz, 1H), 4.32 (m, 1H), 2.02 (m, 1H), 1.71 (m, 1H), 1.45 (d, J = 7.3 Hz, 3H) , 1.30-1.15 (br, 6H), 0.84 (t, J = 6.8 Hz, 3H); ^{13}C NMR (100 MHz, $CDCl_3$, δ): 167.69, 167.12, 136.75, 133.65, 130.51, 128.65, 126.42, 124.43, 47.78, 33.59, 31.37, 26.42, 22.49, 18.64, 13.99; MS (GC) *m/z* 323 (M^+, Calcd 323.05). Anal. calcd for $C_{15}H_{18}BrNO_2$: C 55.57, H 5.60, N 4.32; found: C 55.50, H 5.33, N 4.34.

*Synthesis of **18***: 4-Bromophthalic anhydride (4.00 g, 17.6 mmol) and 3-isopropoxypropylamine (2.06 g, 17.6 mmol) were placed in a round-bottomed flask and dissolved with DMF (50 mL). The reaction mixture was stirred at 140 °C for 24 h. After being cooled to room temperature and addition of water, the resulting mixture was extracted with EtOAc and the organic layer was washed with water. After removal of the solvent under reduced pressure, the residue was purified by column chromatography on silica gel (hexane/EtOAc = 10/1) to give **18** (3.50 g, 61%). Colorless solid; m.p.: 74-75 °C; ^{1}H NMR (400 MHz, $CDCl_3$, TMS, δ): 7.97 (d, J = 1.5 Hz, 1H), 7.84 (dd, J = 8.0, 1.5 Hz, 1H), 7.70 (d, J = 8.0 Hz, 1H), 3.80 (d, J = 6.9 Hz, 2H), 3.49 (m, 1H), 3.45 (t, J = 6.0 Hz, 2H), 1.93 (m, 2H), 1.06 (d, J = 6.4 Hz, 6H); ^{13}C NMR (100 MHz, $CDCl_3$, δ): 167.59, 167.05, 136.78, 133.89, 130.78, 128.66, 126.50, 124.49, 71.56, 65.61, 36.08, 28.81, 21.94; MS (GC) *m/z* 325 (M^+, Calcd 325.03). Anal. calcd for $C_{14}H_{16}BrNO_3$: C 51.55, H 4.94, N 4.29; found: C 51.42, H 5.03, N 4.36.

*Synthesis of **19***: 2-Bromothieno[2,3-*c*]furan-4,6-dione (1.00 g, 4.29 mmol) and 2-ethyl-1-hexylamine (555 mg, 4.29 mmol) were placed in a round-bottomed flask and dissolved with toluene (40 mL), and the resulting mixture was refluxed for 20 h. After being cooled to room temperature, the solvent was removed under reduced pressure and $SOCl_2$ (50 mL) was added. The resulting mixture was refluxed for 3 h. After removal of the solvent under reduced pressure, the residue was purified by column chromatography on silica gel (hexane/EtOAc = 19/1) to give **19** (770 mg, 52%). Colorless solid; m.p.: 61-62 °C; ^{1}H NMR (400 MHz, $CDCl_3$, TMS, δ): 7.31 (s, 1H), 3.48 (d, J = 7.3 Hz, 2H), 1.76 (m, 1H), 1.35-1.25 (br, 8H), 0.90 (t, J = 7.3 Hz, 3H), 0.88 (t, J = 6.9 Hz, 3H); ^{13}C NMR (100 MHz, $CDCl_3$, δ): 163.26, 162.24, 143.78, 140.38, 125.42, 123.83, 42.47, 38.34, 30.39, 28.43, 23.71, 23.01, 14.07, 10.39; MS (GC) *m/z* 343 (M^+, Calcd 343.02). Anal. calcd for $C_{14}H_{18}BrNO_2S$: C 48.84, H 5.27, N 4.07; found: C 49.32, H 5.09, N 4.09.

*Synthesis of **20***: 3-Bromofuro[3,4-*b*]pyridine-5,7-dione (460 mg, 2.01 mmol) and 2-ethyl-1-hexylamine (340 mg, 2.62 mmol) were placed in a round-bottomed flask and dissolved with AcOH (4 mL). The reaction mixture was refluxed for 12 h. After being cooled to room temperature and addition of water, the resulting mixture was extracted with toluene and the organic layer was washed with water. After removal of the solvent under reduced pressure, the residue was purified by column chromatography on silica gel (hexane/$CHCl_3$ = 1/1) to give **20** (288 mg, 42%). Colorless solid; m.p.: 97-98 °C; ^{1}H NMR (400 MHz, $CDCl_3$, TMS, δ): 9.02 (d, J = 2.0 Hz, 1H), 8.28 (d, J = 2.0 Hz, 1H), 3.64 (d, J = 7.3 Hz, 2H), 1.85 (m, 1H), 1.40-1.24 (br, 8H), 0.91 (t, J = 7.3 Hz, 3H), 0.88 (t, J = 7.0 Hz, 3H); ^{13}C NMR (100 MHz, $CDCl_3$, δ): 165.82, 165.17, 156.31, 149.64, 133.73, 128.42, 125.44, 42.40, 38.21, 30.41, 28.38, 23.75, 22.98, 14.05, 10.35; MS (GC) *m/z* 337 (M^+, Calcd 338.06). Anal. calcd for $C_{15}H_{19}BrN_2O_2$: C 53.11, H 5.65, N 8.26; found: C 53.11, H 5.54, N 8.21.

*Synthesis of **Ph-H***: 1a (194 mg, 0.63 mmol), **2** (48 mg, 0.26 mmol), CuI (5 mg, 0.03 mmol), and $Pd(PPh_3)_4$ (30 mg, 0.03 mmol) were placed in a test tube with screw cap and dissolved with toluene (6 mL) and triethylamine (3 mL). The reaction mixure was refluxed for 1.5 h. After being cooled to room temperature, the reaction mixture was concentrated under reduced pressure and then purified by column chromatography on silica gel ($CHCl_3$), followed by purification with preparative GPC ($CHCl_3$) to give **Ph-H** (102 mg, 61%). Yellow solid; m.p.: 200-201 °C; ^{1}H NMR (400 MHz, $CDCl_3$, TMS, δ): 8.11 (s, 2H), 7.99 (d, J = 7.8, 2H), 7.88 (d, J = 7.8 Hz, 2H), 7.87 (s, 2H), 3.70 (t, J = 7.3 Hz, 4H), 1.69 (m, 4H), 1.40-1.27 (br, 12H), 0.89 (t, 6H); ^{13}C NMR (100 MHz, $CDCl_3$, δ): 167.69, 167.59, 154.17, 137.17, 132.91, 132.51, 131.69, 128.36, 126.41, 123.28, 117.03, 95.83, 88.94, 38.33, 31.36, 28.54, 26.54, 22.52, 14.03; MS MALDI-TOF (1,8,9-trihydroxyanthracene matrix) *m/z* 642.41 (M^+, Calcd 642.23); Anal. calcd for $C_{38}H_{34}N_4O_4S$: C 71.01, H 5.33, N 8.72; found: C 71.03, H 5.45, N 8.72.

*Synthesis of **Ph-D***: **Ph-D** was synthesized from compound **1b** (529 mg, 1.34 mmol), **2** (103 mg, 0.56 mmol), CuI (11 mg, 0.06 mmol), and $Pd(PPh_3)_4$ (65 mg, 0.06 mmol) with a yield of 59% by following the procedure used for the preparation of **Ph-H**. Yellow solid; m.p.: 175-176 °C; ^{1}H NMR (400 MHz, $CDCl_3$, TMS, δ): 8.11 (s, 2H), 7.99 (dd, J = 7.8, 1.4 Hz, 2H), 7.88 (d, J = 7.8 Hz, 2H), 7.87 (s, 2H), 3.70 (t, J = 7.6 Hz, 4H), 1.69 (m, 4H), 1.35-1.25 (br, 36H), 0.88 (t, J = 7.0 Hz, 6H); ^{13}C NMR (100 MHz, $CDCl_3$, δ): 167.70, 167.59, 154.17, 137.17, 132.91, 132.52, 131.69, 128.36, 123.28, 117.04, 95.84, 88.94, 38.34, 31.92, 29.62, 29.62, 29.57, 29.50, 29.35, 29.19, 28.58, 26.89, 22.69, 14.14; MS MALDI-TOF (1,8,9-trihydroxyanthracene matrix) *m/z* 810.77 (M^+, Calcd 810.42). Anal. calcd for $C_{50}H_{58}N_4O_4S$: C 74.04, H 7.21, N 6.91; found: C 74.03, H 7.21, N 6.79.

*Synthesis of **Ph-MH***: **Ph-MH** was synthesized from compound **1c** (414 mg, 1.28 mmol), **2** (98 mg, 0.53 mmol), CuI (10 mg, 0.05 mmol), and $Pd(PPh_3)_4$ (61 mg, 0.05 mmol) with a yield of 60% by following the procedure used for the preparation of **Ph-H**. Yellow solid; m.p.: 203-204 °C; ^{1}H NMR (400 MHz, $CDCl_3$, TMS, δ): 8.09 (s, 2H), 7.98 (d, J = 7.6 Hz, 2H), 7.88 (s, 2H), 7.86 (d, J = 7.6 Hz, 2H), 4.36 (m, 2H), 2.06 (m, 2H), 1.75 (m, 2H), 1.49 (d, J = 6.9 Hz, 6H), 1.28 (br, 12H), 1.28 (t, J = 6.9 Hz, 6H); ^{13}C NMR (100 MHz, $CDCl_3$, δ): 167.81, 167.68, 154.17, 137.14, 132.91, 132.34, 131.54, 128.30, 126.30, 123.17, 117.04, 95.88, 88.86, 47.79, 33.65, 31.41, 26.47, 22.51, 18.67, 14.01; MS MALDI-TOF (1,8,9-trihydroxyanthracene matrix) *m/z* 670.52 (M^+, Calcd 670.26). Anal. calcd for $C_{40}H_{38}N_4O_4S$: C 71.62, H 5.71, N 8.35; found: C 71.60, H 5.74, N 8.24.

*Synthesis of **Ph-Ipop***: **Ph-Ipop** was synthesized from compound **1d** (217 mg, 0.66 mmol), **2** (51 mg, 0.28 mmol), CuI (5 mg, 0.03 mmol), and $Pd(PPh_3)_4$ (32 mg, 0.03 mmol) with a yield of 55% by following the procedure used for the preparation of **Ph-H**. Yellow solid; m.p.: 219-220 °C; ^{1}H NMR (400 MHz, $CDCl_3$, TMS, δ): 8.11 (s, 2H), 7.99 (d, J = 7.8, 2H), 7.88 (d, J = 7.8 Hz, 2H), 7.87 (s, 2H), 3.83 (t, J = 6.6 Hz, 4H), 3.51 (m, 2H), 3.48 (t, J = 6.0 Hz, 4H), 1.96 (m, 4H), 1.08 (d, J = 6.0 Hz, 12H); ^{13}C NMR (100 MHz, $CDCl_3$, δ): 167.71, 167.56, 154.18, 137.15, 132.92, 132.62, 131.82, 128.32, 126.37, 123.25, 117.04, 95.85, 88.90, 71.58, 65.68, 36.12, 28.87, 21.97; MS MALDI-TOF (1,8,9-trihydroxyanthracene matrix) *m/z* 674.50 (M^+, Calcd 674.22). Anal. calcd for $C_{38}H_{34}N_4O_6S$: C 67.64, H 5.08, N 8.30; found: C 67.60, H 5.18, N 8.26.

*Synthesis of **Th-EH***: **Th-EH** was synthesized from compound **1e** (351 mg, 1.02 mmol), **2** (85 mg, 0.46 mmol), CuI (8 mg, 0.05 mmol), and $Pd(PPh_3)_4$ (54 mg, 0.05 mmol) in THF (8 mL) and diisopropylethylamine (0.8 mL) with a yield of 91% by following the procedure used for the preparation of **Ph-H**. Yellow solid; m.p.: 254-255 °C; ^{1}H NMR (400 MHz, $CDCl_3$, TMS, δ): 7.87 (s, 2H), 7.57 (s, 2H), 3.53 (d, J = 6.9 Hz, 4H), 1.80 (m, 2H), 1.37-1.25 (m, 16H), 0.92 (t, J = 7.2 Hz, 6H), 0.89 (t, J = 7.2 Hz, 6H); ^{13}C NMR (100 MHz, $CDCl_3$, δ): 163.66, 162.57, 153.79, 143.82, 141.11, 134.37, 132.85, 125.95, 116.69, 93.35, 89.21, 42,60, 38.41, 30.43, 28.48, 23.77, 23.02, 14.07, 10.41; MS MALDI-TOF (1,8,9-trihydroxyanthracene matrix) *m/z* 710.40 (M^+, Calcd 710.21). Anal. calcd for $C_{38}H_{38}N_4O_4S_3$: C 64.20, H 5.39, N 7.88; found: C 64.24, H 5.47, N 7.70.

*Synthesis of **Py-EH***: **Py-EH** was synthesized from compound **1f** (288 mg, 0.85 mmol), **2** (71 mg, 0.39 mmol), CuI (7 mg, 0.04 mmol), and $Pd(PPh_3)_4$ (45 mg, 0.04 mmol) THF (8 mL) and diisopropylethylamine (0.8 mL) with a yield of 63% by following the procedure used for the preparation of **Ph-H**. Orange solid; m.p.: 232-233 °C; ^{1}H NMR (400 MHz, $CDCl_3$, TMS, δ): 9.20 (d, J = 1.8 Hz, 2H), 8.38 (d, J = 1.8, 2H), 7.93 (s, 2H), 3.68 (d, J = 6.9 Hz, 4H), 1.88 (m, 1H), 1.40-1.26 (br, 8H), 0.94 (t, J = 7.6, 6H), 0.90 (t, J = 7.0, 6H); ^{13}C NMR (100 MHz, $CDCl_3$, δ): 165.91, 165.71, 157.54, 154.02, 150.18, 133.46, 133.20, 126.90, 123.71, 116.90, 92.90, 91.73, 42.43, 38.26, 30.45, 28.41, 23.79, 23.00, 14.06, 10.37; MS MALDI-TOF (1,8,9-trihydroxyanthracene matrix) *m/z* 700.41 (M^+, Calcd 700.28). Anal. calcd for $C_{40}H_{40}N_6O_2S$: C 68.55, H 5.75, N 11.99; found: C 68.55, H 5.74, N 11.88.

*Synthesis of **Na-EH***: **Na-EH** was synthesized from compound **1g** (306 mg, 0.92 mmol), **2** (123 mg, 0.41 mmol), CuI (8 mg, 0.04 mmol), and $Pd(PPh_3)_4$ (48 mg, 0.04 mmol) THF (8 mL) and diisopropylethylamine (0.8 mL) with a yield of 98% by following the procedure used for the preparation of **Ph-H**. This compound was purified by column chromatography on silica gel ($CHCl_3$), followed by precipitation using $CHCl_3$ and acetone. Orange solid; m.p.: 281-282 °C; ^{1}H NMR (400 MHz, $CDCl_3$, TMS, δ): 9.03 (d, J = 8.0 Hz, 2H), 8.68 (d, J = 7.3 Hz, 2H), 8.55 (d, J = 8.0 Hz, 2H), 8.08 (d, J = 7.3 Hz, 2H), 7.97 (s, 2H), 7.93 (t, J = 7.3 Hz, 2H), 4.14 (m, 4H), 1.97 (m, 2H), 1.45-1.30 (br, 16H), 0.95 (t, J = 7.6 Hz, 6H), 0.88 (t, J = 7.1 Hz, 6H); ^{13}C NMR (100 MHz, $CDCl_3$, δ): 164.30, 164.04, 154.64, 132.68, 132.46, 131.98, 131.83, 131.30, 130.28, 128.28, 128.00, 126.47, 123.32, 123.27, 117.48, 94.97, 94.26, 44.46, 38.14, 30.97, 28.82, 24.28, 23.11, 14.03, 10.72; MS MALDI-TOF (1,8,9-trihydroxyanthracene matrix) *m/z* 798.55 (M^+, Calcd 798.32). Anal. calcd for $C_{50}H_{46}N_4O_4S$: C 75.16, H 5.80, N 7.01; found: C 75.01, H 5.90, N 6.80.

3.9 References

1 M. Mas-Torrent and C. Rovira, *Chem. Rev.*, 2011, **111**, 4833.

2 J. Cornil, D. Beljonne, J.-P. Calbert and J.-L. Brédas, *Adv. Mater.*, 2001, **13**, 1053; H. Yamagata, J. Norton, E. Hontz, Y. Olivier, D. Beljonne, J.-L. Brédas, R. J. Silbey and F. C. Spano, *J. Chem. Phys.*, 2011, **134**, 204703.

3 D. Placencia, W. Wang, J. Gantz, J. L. Jenkins and N. R. Armstrong, *J. Phys. Chem. C*, 2011, **115**, 18873; Y. Yuan, G. Giri, A. L. Ayzner, A. P. Zoombelt, S. C. B. Mannsfeld, J. Chen, D. Nordlund, M. F. Toney, J. Huang and Z. Bao, *Nat. Commun.*, 2014, **5**, 3005.

4 D. H. Kaelble and K. C. Uy, *J. Adhesion*, 1970, **2**, 50.

5 F. M. Fowkes, *J. Phys. Chem.*, 1962, **66**, 382; X. Ma, T.-S. Chung and R. J. Good, *J. Polym. Sci., Part B: Polym.*

Phys., 1998, **36**, 2327; E. Ruckenstein and S. V. Gourisankar, *J. Colloid Interface Sci.*, 1986, **109**, 557.

6 A. Hadipour, R. Müller and P. Heremans, *Org. Electron.*, 2013, **14**, 2379.

7 A. Maurano, R. Hamilton, C. G. Shuttle, A. M. Ballantyne, J. Nelson, B. O'Regan, W. Zhang, I. McCulloch, H. Azimi, M. Morana, C. J. Brabec and J. R. Durrant, *Adv. Mater.*, 2010, **22**, 4987.

8 K. Vandewal, K. Tvingstedt, A. Gadisa, O. Inganäs and J. V. Manca, *Nat. Mater.*, 2009, **8**, 904.

9 J.-L. Brédas, J. E. Norton, J. Cornil and V. Coropceanu, *Acc. Chem. Res.*, 2009, **42**, 1691; T. M. Clarke and J. R. Durrant, *Chem. Rev.*, 2010, **110**, 6736; R. A. J. Janssen and J. Nelson, *Adv. Mater.*, 2013, **25**, 1847; S. D. Dimitrov and J. R. Durrant, *Chem. Mater.*, 2014, **26**, 616.

10 G. G. Malliaras, J. R. Salem, P. J. Brock and C. Scott, *Phys. Rev. B*, 1998, **58**, 13411; C. Goh, R. J. Kline, M. D. McGehee, E. N. Kadnikova and J. M. J. Fréchet, *Appl. Phys. Lett.*, 2005, **86**, 122110; H. Azimi, A. Senes, M. C. Scharber, K. Hingerl and C. J. Brabec, *Adv. Energy. Mater.*, 2011, **1**, 1162.

11 A. Gadisa, W. Mammo, L. M. Andersson, S. Admassie, F. Zhang, M. R. Andersson and O. Ingnäs, *Adv. Funct. Mater.*, 2007, **17**, 3836; M. Abbas and N. Tekin, *Appl. Phys. Lett.*, 2012, **101**, 073302.

12 Y. Ie, C. Sato, M. Nitani, H. Tada and Y. Aso, *Chem. Lett.* 2014, **43**, 1640.

13 W. C. W. Leu, A. E. Fritz, K. M. Digianantonio and C. Scott Hartley, *J. Org. Chem.*, 2012, **77**, 2285; D. Gudeika, R. Lygaitis, V. Mimaite, J. V. Grazulevicius, V. Jankauskas M. Lapkowski and P. Data, *Dyes and Pigments*, 2011, **91**, 13; G. Jaeschke, S. Jolidon, L. Lindemann, A. Ricci, D. Rueher, H. Stadler and E. Vieira, U.S. 2012/270852.

Chapter 4
Influence of Acceptor Unit Orientation at Donor–Acceptor Interfaces on Photocurrent Generation Efficiency of Perylene Bisimide based Three-Dimensional Acceptor Materials

4.1 Introduction

High γ^{d} values of acceptor materials were found to be of advantage to photocarrier generation in OPV devices. Detailed analysis on relation between the molecular orientation of thin-films and the estimated γ^{d} values were performed in the chapter 3. The result suggested that the γ^{d}s of acceptors are related to the amount of exposed π-conjugated framework toward interface between donor and acceptor. In this respect, solubilized acceptor materials with no alkyl chain at the outer edge of molecules might become candidates to achieve high γ^{d}.

From this standpoint, the author synthesized and evaluated new acceptor materials of **MHPI-BTCN**, **PhPI-BTCN**, **F4PI-BTCN**, and **F4(PI-BTCN)2** (Figure 4.1 and detailed results are shown in experimental section).[1] Thanks to its twisted π-conjugated framework, **PhPI-BTCN**, **F4PI-BTCN**, and **F4(PI-BTCN)2** posess solubility even though they have no solubilizing alkyl chain at the outer edge. The highest J_{SC} of 7.65 mA cm^{-2} was obtained for the device employing the acceptor of **F4PI-BTCN** (Table 4.1). As expected, the γ^{d} and J_{SC} values of **PhPI-BTCN**, **F4PI-BTCN**, and **F4(PI-BTCN)2** were increased compared with those of branched alkylated acceptors of **MHPI-BTCN**. However, the author also noticed that clear correlation between γ^{d} and J_{SC} is not applicable among **PhPI-BTCN**, **F4PI-BTCN**, and **F4(PI-BTCN)2**.

In addition, no clear correlation was found within *as*NTz/*s*NTz based acceptors (Figure 4.2). The author also designed and synthesized a new acceptor material of ***as*NTz-NP-F** and compared the OPV performance with recently developed ***s*NTz-NP-F**.[2] As the results of SFE estimation, γ^{d}s of ***as*NTz-NP-F** and ***s*NTz-NP-F** were

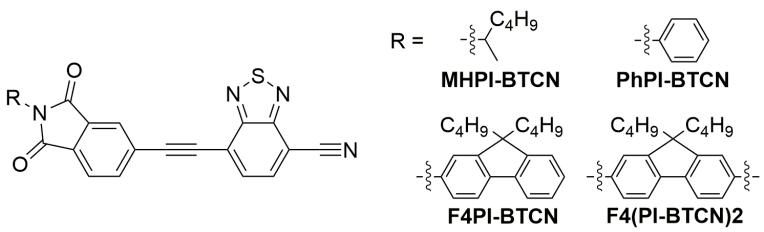

Figure 4.1. Chemical structure of cyano-substituted benzothiadiazole-based acceptors.

Table 4.1. Properties and OPV performances of cyano-substituted benzothiadiazole-based acceptors.

Compounds	E_{LUMO} [eV][a]	PCE [%][b]	J_{sc} [mA cm^{-2}][b]	V_{oc} [V][b]	FF[b]	γ^{d} [mJ cm^{-2}]
MePI-BTCN	–3.48	0.19	0.93	0.57	0.36	9.9
PhPI-BTCN	–3.47	0.12	1.39	0.23	0.37	10.9
F4PI-BTCN	–3.48	0.32	1.45	0.53	0.41	11.6
F4(PI-BTCN)2	–3.48	0.28	1.34	0.47	0.45	17.3

[a] Estimated from CV measurements in *o*-DCB/acetonitrile (5/1) containing 0.1 M $TBAPF_6$. [b] ITO/ZnO/P3HT:acceptor/MoO_3/Al.

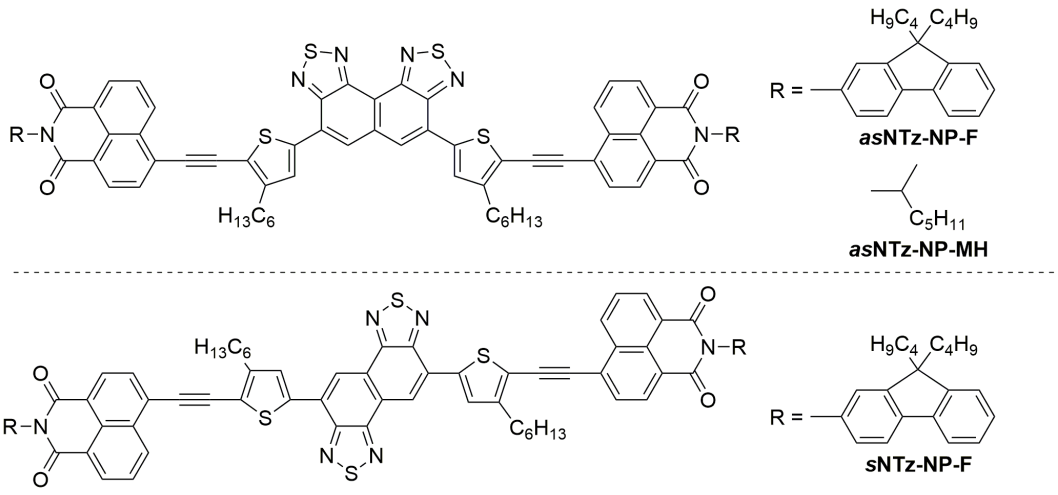

Figure 4.2. Chemical structure of *as*NTz/*s*NTz based acceptors.

.

Table 4.2. Properties and OPV performances of *as*NTz/*s*NTz based acceptors.

Compounds	E_{LUMO} [eV][a]	PCE [%][b]	J_{sc} [mA cm^{-2}][b]	V_{oc} [V][b]	FF[b]	γ^d [mJ cm^{-2}]
***as*NTz-NP-F**	–3.51	0.54	1.73	0.79	0.39	27.9
***as*NTz-NP-MH**	-	0.17	0.70	0.55	0.38	16.1
***s*NTz-NP-F**	–3.65	2.48	5.31	0.90	0.52	28.1

[a] Estimated from LEIPS measurements of acceptor films. [b] ITO/ PEDOT:PSS/P3HT:acceptor/Ca/Al.

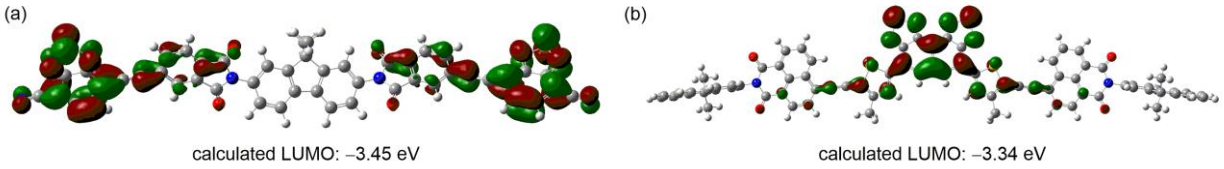

Figure 4.3. Calculated LUMO and energy levels of (a) **F4(PI-BTCN)2** and (b) ***as*NTz-NP-F**. All the alkyl groups were replaced with methyl groups to facilitate the calculation.

estimated to be 27.9 and 28.1 mJ cm^{-2}, respectively (Table 4.2). However, the OPV performances of ***as*NTz-NP-F** was lower than that of ***s*NTz-NP-F** even though both compound indicated high γ^d values. This indicates that high γ^d value of acceptor material is not the sufficient condition for high performance acceptor materials.

In both case of cyano-substituted benzothiadiazole-based acceptors and *as*NTz based acceptors, each molecule contains several segments of π-conjugated frameworks. For example, **F4(PI-BTCN)2** contains fluorene, phthalimide, and cyano-substituted benzothiadiazole and for the case of ***as*NTz-NP-F**, it contains fluorene, naphtylimide, and central *as*NTz unit. All these molecular segments can bring high γ^d value if it are exposed to interface. On the other hand, as shown in Figure 4.3, the LUMO coefficients are localized on cyano-substituted benzothiadiazole unit and *as*NTz unit. Therefore, just because the materials indicate high γ^d values, they may not necessarily indicate high J_{SC} in these cases. In addition, as a supporting evidence, the γ^d and J_{SC} values of branched

alkylated compound ***as*NTz-NP-MH** went low. The correlation between γ^{d} and J_{SC} is considered to be effective when the electron accepting units are exposed toward interface.

In this context, a promising acceptor molecular structure is 3-D arranged molecule surrounded with extended π-electron acceptor units; which is considered to expose its acceptor units toward interface. Very recently, large non-planar structures is begin to be employed for non-fullerene acceptors, [4–7] which is based on the hypothesis that large non-planarity contributes to diminishing π-stacked self-aggregations, promoting the favorable phase separation, and increasing dimensionality of electron-transport pathways.[7,8] Among these acceptors, 3-D perylene bis(dicarboximide) (PDI) derivatives constructed by the use of tetraphenyl methane, spirobifluorene, or tetraphenylethylene as a central core block have been reported to exhibit promising OPV performance. Since the strong electron-accepting units are located in the outer edge of these molecules and thus the LUMOs localize on this part (vide infra), the author anticipated that the relationship between γ^{d} and J_{SC} would be observed for these 3D acceptors. In the final chapter, to systematically investigate the structure–properties–OPV characteristics of 3D acceptors, acceptor unit is fixed to be PDI (Figure 4.4), and the author focus on the influence of (1) alkyl group in the PDI (**TetraBP-*N*-PDIC9**[3] vs. **TetraBP-*N*-PDIC2**), (2) orientation of PDI unit in the molecules (**TetraBP-*N*-PDIC2** vs. **TetraP-*B*-PDI**), and (3) central core units (**TetraP-*B*-PDI**, **Pyrene-*B*-PDI**, and **SpiroF-*B*-PDI**). Note that **TetraP-*B*-PDI** and **SpiroF-*B*-PDI** derivatives have been reported to show high PCEs under the combination with a particular donor–acceptor copolymer.[5] As summarized in Figure 4.5, DFT calculation at the B3LYP/6-31G (d,p) level indicated that these molecules showed non-planar geometry and localized LUMOs on the PDI units. In this chapter, the synthesis, molecular properties, photovoltaic performance, and film properties of these acceptors are discussed.

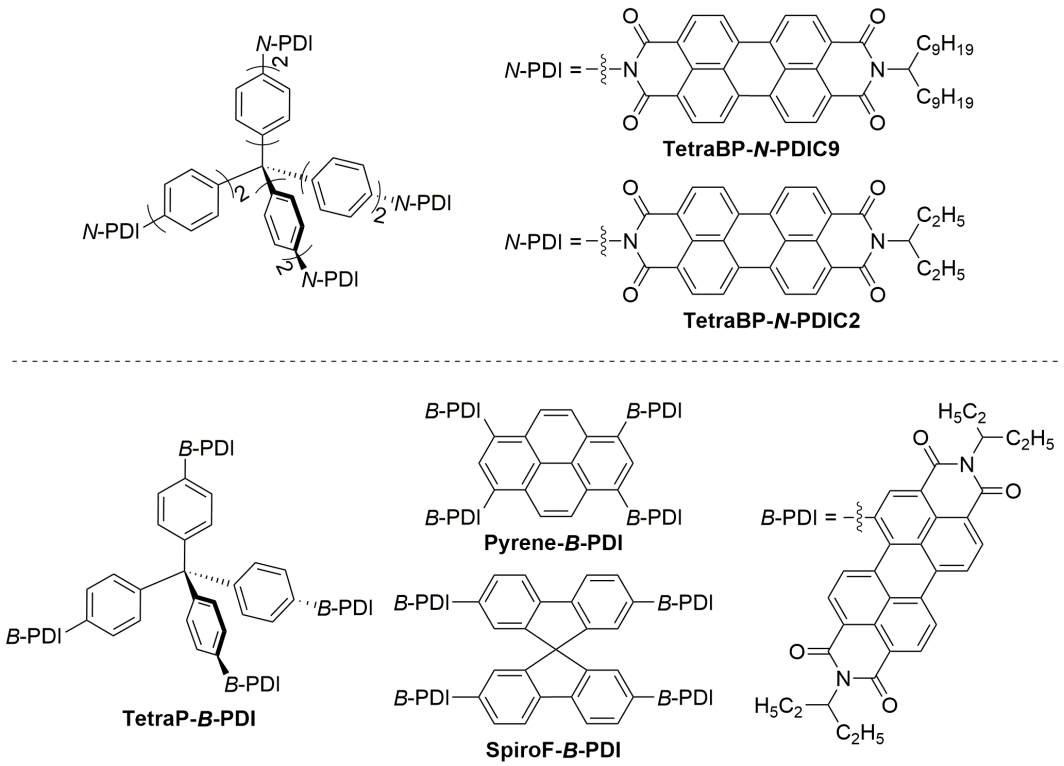

Figure 4.4. Chemical structure of 3-D arranged PDI-based acceptors investigated in this chapter.

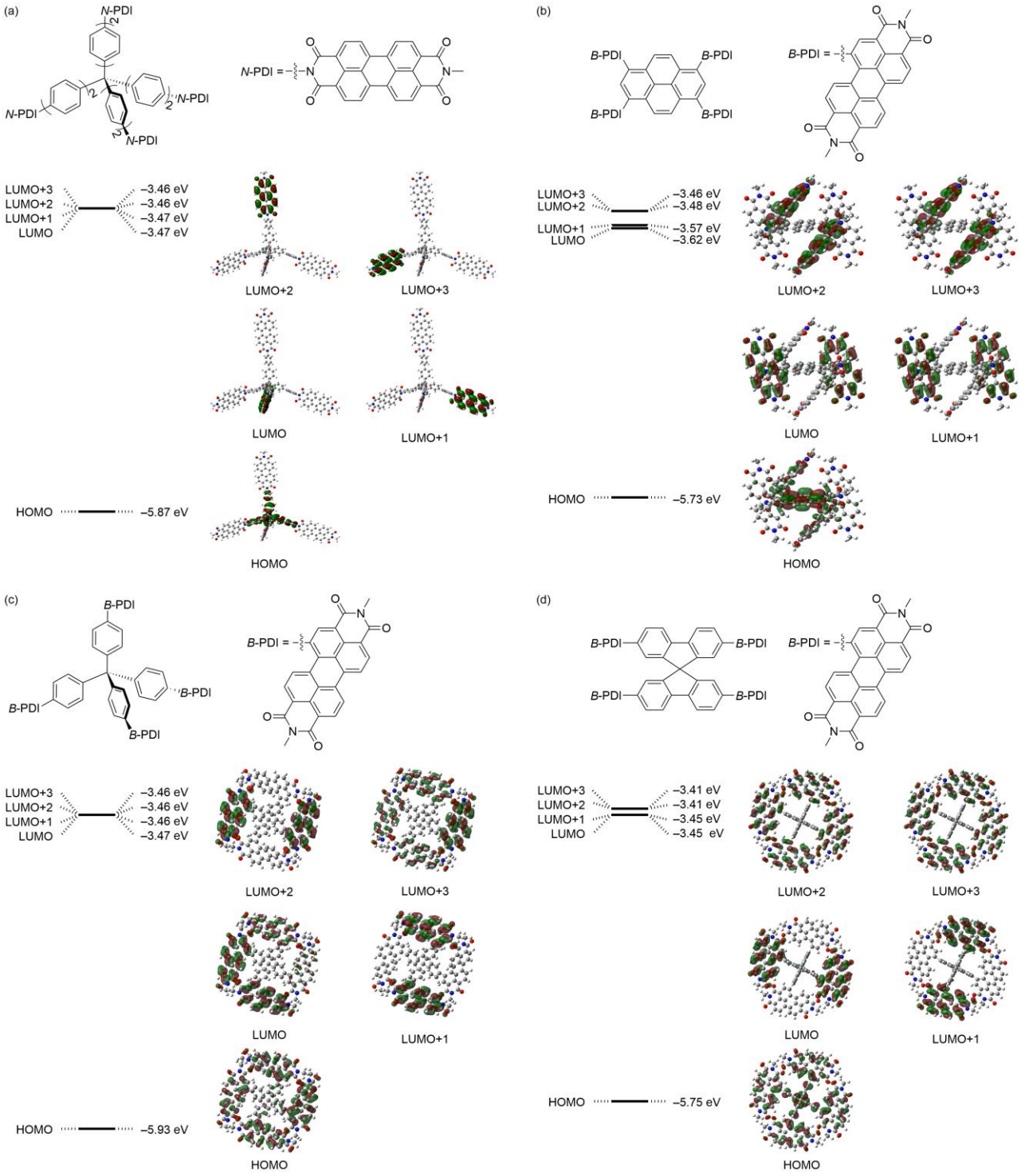

Figure 4.5. Calculated structures and molecular orbitals of model compounds for (a) **TetraBP-*N*-PDIC9** and **TetraBP-*N*-PDIC2**, (b) **Pyrene-*B*-PDI**, (c) **TetraP-*B*-PDI**, and (d) **SpiroF-*B*-PDI**. All alkyl groups were replaced with methyl groups to ease the calculation.

4.2 Synthesis and Molecular Properties

The 3-D arranged PDI derivatives were synthesized by the Suzuki-Miyaura coupling reaction between central cores and terminal PDI units in the presence of $Pd(PPh_3)_4$ in toluene/H_2O/MeOH (Scheme 4.1). Due to the presence of

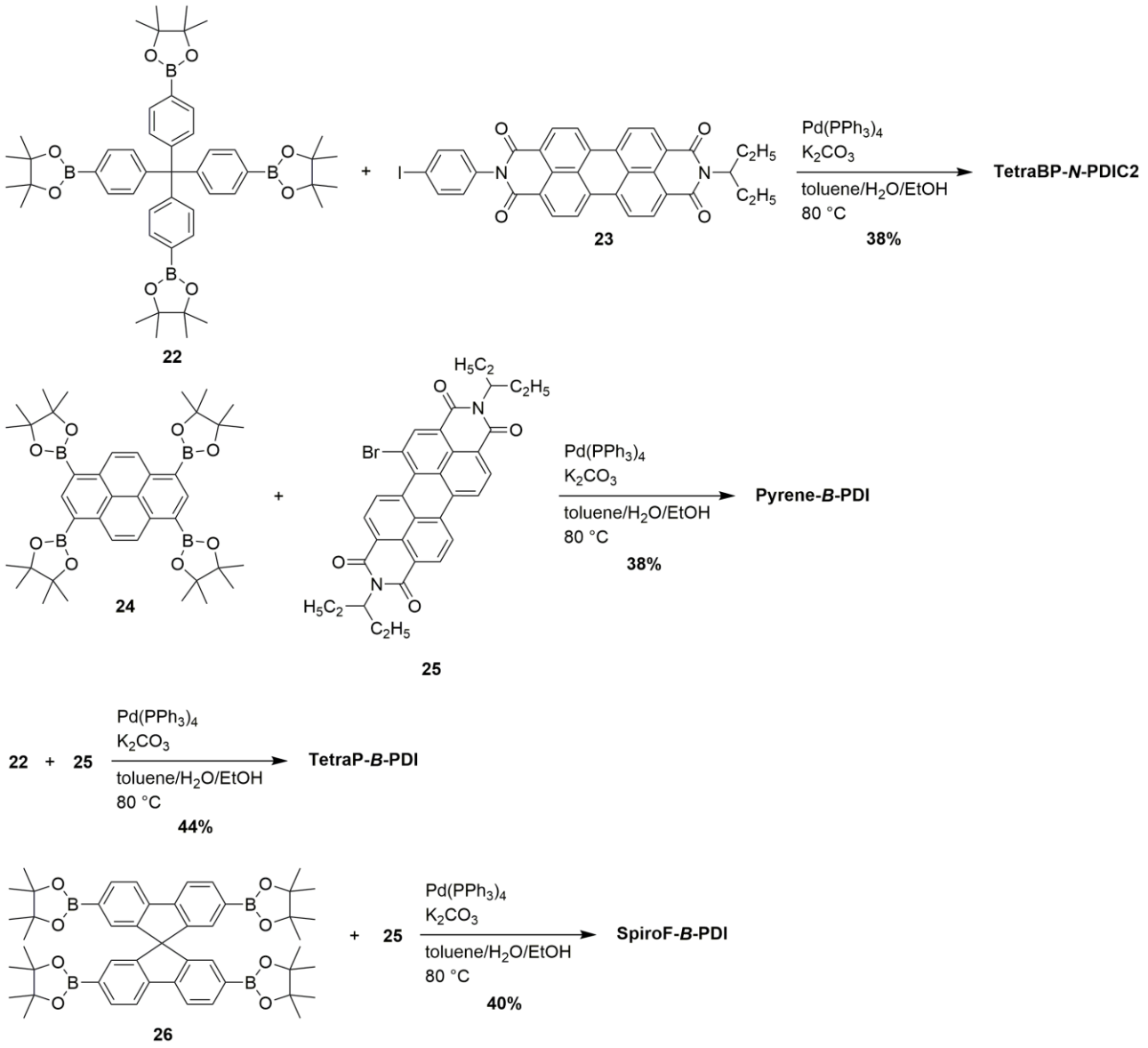

Scheme 4.1. Synthesis of 3-D acceptors.

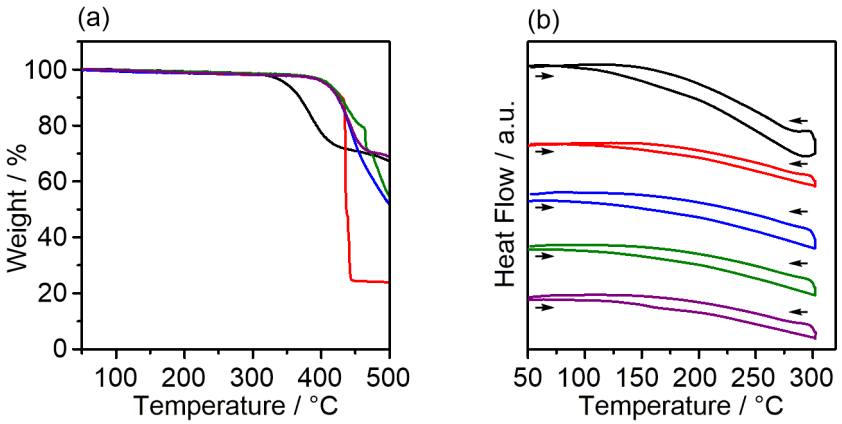

Figure 4.6. (a) TGA and (b) DSC curves of **TetraBP-*N*-PDIC9** (black), **TetraBP-*N*-PDIC2** (red), **Pyrene-*B*-PDI** (blue), **TetraP-*B*-PDI** (green), and **SpiroF-*B*-PDI** (purple) with a scanning rate of 10 °C min^{-1} under N_2.

alkyl chains and steric hindrance within the chemical structures, the synthesized acceptors exhibited good solubilities in common chlorinated solvents such as chloroform, CB, and *o*-DCB.

The thermal properties of the synthesized compounds were investigated using TGA and DSC. As shown in Figure 4.6(a), the TGA curves of **TetraBP-*N*-PDIC9**, **TetraBP-*N*-PDIC2**, **Pyrene-*B*-PDI**, **TetraP-*B*-PDI**, and **SpiroF-B-PDI** showed T_d of higher than 348 °C. The DSC trace of these compounds showed no obvious melting or thermal decomposition peaks up to 300 °C, indicating that these compounds are sufficiently stable for use in OPV device application (Figure 4.6(b)).

In UV-vis spectra in dilute $CHCl_3$ solution, all the compounds exhibit one absorption band with several vibronic peaks in visible region of between 450 and 550 nm (Figure 4.7(a)). In reflection with having the same π-conjugated framework, **TetraBP-*N*-PDIC9** and **TetraBP-*N*-PDIC2** showed similar molar extinction coefficients (ε). On the other hand, **Pyrene-*B*-PDI**, **TetraP-*B*-PDI**, and **SpiroF-B-PDI** showed blunt absorptions ascribable to the bay-linked framework. Moreover, compared with **TetraP-*B*-PDI**, **Pyrene-*B*-PDI** and **SpiroF-*B*-PDI** showed slight tailing to a long-wavelength region in both solutions and films (Figure 4.7), which could be due to their MOs partially delocalized between the central core and PDI units as seen in their HOMOs (Figure 4.5(b) and (d)). The optical energy gaps (ΔE_{film}^{opt}) of our investigated acceptors determined from the onset of thin-film spectra are distributed in a narrow range between 1.93 and 2.28 eV (Table 4.3).

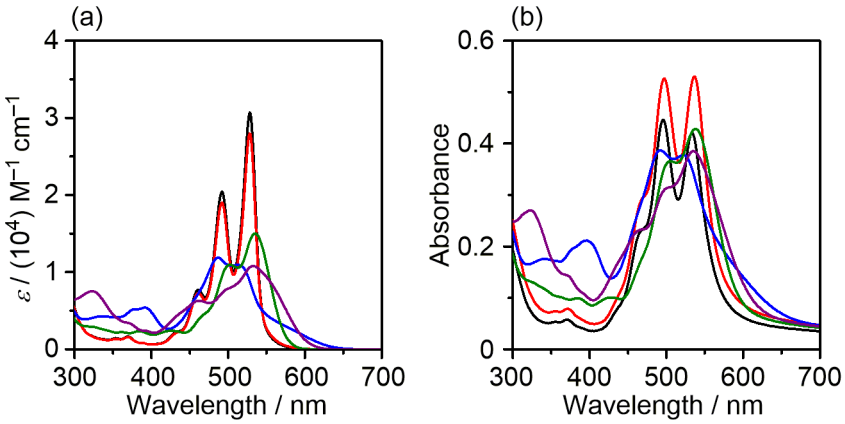

Figure 4.7. UV-vis absorption spectra of **TetraBP-*N*-PDIC9** (black), **TetraBP-*N*-PDIC2** (red), **Pyrene-*B*-PDI** (blue), **TetraP-*B*-PDI** (green), and **SpiroF-*B*-PDI** (purple) (a) in $CHCl_3$ solution and (b) in films.

Table 4.3. Estimated LUMOs, HOMOs, and corresponding energy gaps of PDI-based acceptors.

Compounds	E_{LUMO} [eV][a]	E_{HOMO} [eV][b]	ΔE [eV]	ΔE_{sol}^{opt} [eV][c]	ΔE_{film}^{opt} [eV][d]
TetraBP-*N*-PDIC9	–3.70	–5.83	2.13	2.17	2.18
TetraBP-*N*-PDIC2	–3.75	–5.90	2.15	2.28	2.18
Pyrene-*B*-PDI	–3.78	–5.85	2.07	1.93	1.94
TetraP-*B*-PDI	–3.69	–5.92	2.23	2.16	2.10
SpiroF-*B*-PDI	–3.70	–5.86	2.16	2.05	2.04

[a] Estimated from LEIPS in the film. [b] Estimated from PESA in the film. [c] Determined by the onset of UV-vis absorption spectrum in $CHCl_3$, [d] Determined by the onset of UV-vis absorption spectrum in the film.

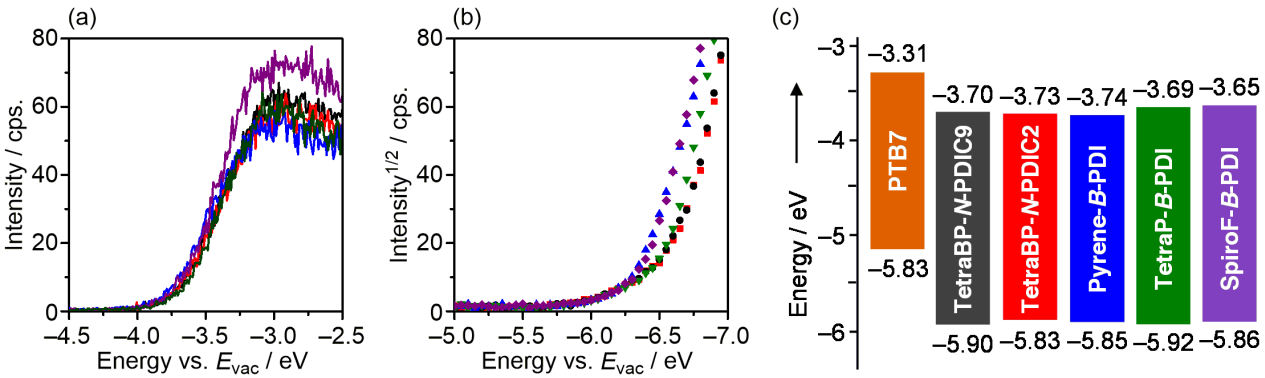

Figure 4.8. (a) LEIPS and (b) PESA measurements of TetraBP-*N*-PDIC9 (black), TetraBP-*N*-PDIC2 (red), Pyrene-*B*-PDI (blue), TetraP-*B*-PDI (green), and SpiroF-*B*-PDI (purple). (c) Estimated energy levels of materials investigated in this study.

The electrochemical properties of **TetraBP-*N*-PDIC9** were investigated previously by CV measurements performed in a dichloromethane solution.[3] However, **TetraBP-*N*-PDIC9** displayed broad reduction waves due to inter- and intramolecular aggregation of the terminal PDI units, which prevents the precise estimation of LUMO energy level. To overcome this problem, the author performed low-energy inverse photoemission spectroscopy (LEIPS)[9] measurements in order to determine the LUMO energy levels of the present PDI-based acceptors in the film state (Figure 4.8(a)). The electron affinities of **TetraBP-*N*-PDIC9**, **TetraBP-*N*-PDIC2**, **Pyrene-*B*-PDI**, **TetraP-*B*-PDI**, and **SpiroF-*B*-PDI** determined from the onset energy with respect to the vacuum level are listed in Table 1. The LUMO energy levels of these compounds range in the narrow distribution between −3.69 and −3.78 eV.

The ionization potentials of the acceptor films were estimated by PESA. The HOMO energies determined from the onset energy were in the range between −5.83 and −5.92 eV (Figure 4.8(b) and Table 4.3). The estimated LUMO and HOMO energies for these compounds as well as those of the donor material of PTB7 (Poly[[4,8-bis[(2-ethylhexyl)oxy]benzo[1,2-*b*:4,5-*b*']dithiophene-2,6-diyl][3-fluoro-2-[(2-ethylhexyl)carbonyl]thieno[3,4-*b*]thiophenediyl]]) are summarized in Figure 4.8(c). Based on this energy diagram, these acceptor molecules provide sufficient LUMO and HOMO offsets for charge carrier generation in OPVs under the combination with PTB7.[10]

4.3 Photovoltaic Performances

OPV devices with a conventional structure of ITO/PEDOT:PSS/active layer/Ca/Al were fabricated using the blended films of PTB7 and the acceptors as the active layers. The donor/acceptor ratio (1:1), processing solvent ($CHCl_3$), and concentration (10 mg/mL) were fixed for a comparison of the OPV characteristics under the same fabrication conditions. Indeed, the thicknesses of the active layers are distributed in a narrow range (Table 4.4), which eases an elucidation of the main factor for determining OPV performance. The *J*–*V* characteristics of devices under AM 1.5 G solar irradiation (100 mW cm^{-2}) are shown in Figure 4.9(a) and the representative device parameters are summarized in Table 4.4 and Tables S1−5. Although all the devices showed a typical photovoltaic conversion phenomenon, the PCEs varied between 0.02% and 2.02%, depending on the acceptors. The highest PCE of 2.02% with an V_{OC} of 0.72 V, a J_{SC} of 7.65 mA cm^{-2}, and a FF of 0.37 was obtained for the device employing the

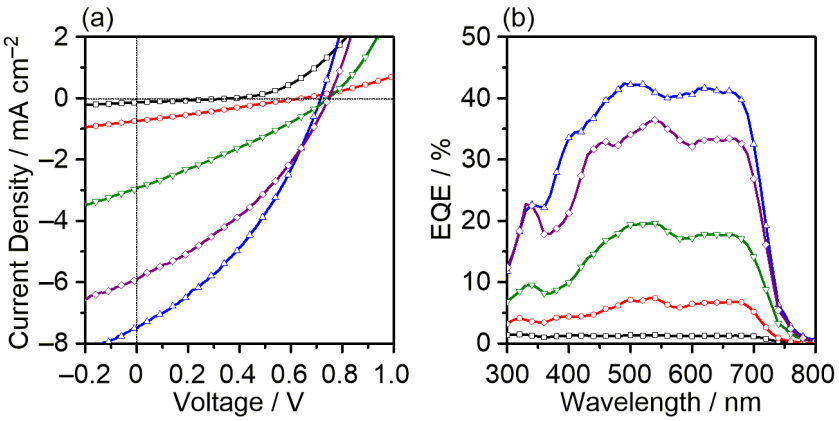

Figure 4.9. (a) *J*-*V* curves and (b) EQE spectra for PTB7/**TetraBP-*N*-PDIC9** (black), PTB7/**TetraBP-*N*-PDIC2** (red), PTB7/**Pyrene-*B*-PDI** (blue), PTB7/**TetraP-*B*-PDI** (green), and PTB7/**SpiroF-*B*-PDI** (purple) OPV devices.

Table 4.4. OPV characteristics and properties of PTB7/PDI-based acceptor blend films.

Blend films	J_{SC} [mA cm^{-2}]	V_{OC} [V]	FF	PCE [%][a,b]	Thickness [nm][c]
PTB7/**TetraBP-N-PDIC9**	0.14	0.39	0.29	0.02 (0.01±0.00)	80.1
PTB7/**TetraBP-N-PDIC2**	0.74	0.65	0.27	0.13 (0.11±0.01)	87.3
PTB7/**Pyrene-B-PDI**	7.65	0.72	0.37	2.02 (1.92±0.07)	79.4
PTB7/**TetraP-B-PDI**	2.94	0.74	0.30	0.65 (0.63±0.01)	89.6
PTB7/**SpiroF-B-PDI**	5.90	0.75	0.36	1.57 (1.56±0.01)	85.8

[a] ITO/PEDOT:PSS/blend films/Ca/Al. [b] The average and standard deviation of five devices are provided in parentheses, see the SI for details. [c] Thickness of the active layer.

newly designed acceptor of **Pyrene-*B*-PDI**. The EQE measurements showed that all the devices exhibit a broad photoresponse between 300 and 750 nm (Figure 4.9(b)). The photocurrent at wavelength regions of 450~550 nm and 550~750 nm can be mainly attributed to the absorptionof the acceptor material and PTB7, respectively (Figure 4.10). This result indicates that both the donor and acceptor materials contribute to the photocurrent generation. The EQE intensities are well correlate with the PCE values as well as J_{sc} values, for example, the best performance device based on **Pyrene-*B*-PDI** showed the maximum EQE. This result indicates that the differe ence in PCEs mainly comes from the difference of largely varied J_{SC} values, that is, from the efficiency of photocurrent generation.

As discussed in chapter 3, the overall photocurrent generation process can be divided into five efficiency factors: η_{Abs}, η_{ED}, η_{CT}, η_{CS}, and η_{CC}.[11] To clarify the origin of the observed J_{SC} differences between the acceptors, we evaluated the properties of the blended films, which were formed on quartz plate under the same fabrication conditions as the active layers in OPVs. The film thicknesses were determined to be around 70–75 nm. As shown in Figures 4.10, UV-vis absorption spectra of all blended films did not show much difference in absorbance and spectral shape. This result indicates that the η_{Abs} is not the dominant factor to determine the photovoltaic characteristics.

The efficiencies, η_{ED} and η_{CT}, were estimated from the PLQE of the blended films relative to the PL intensities of the acceptor films. The PL spectra of the blended films and pristine acceptor films excited at the absorption

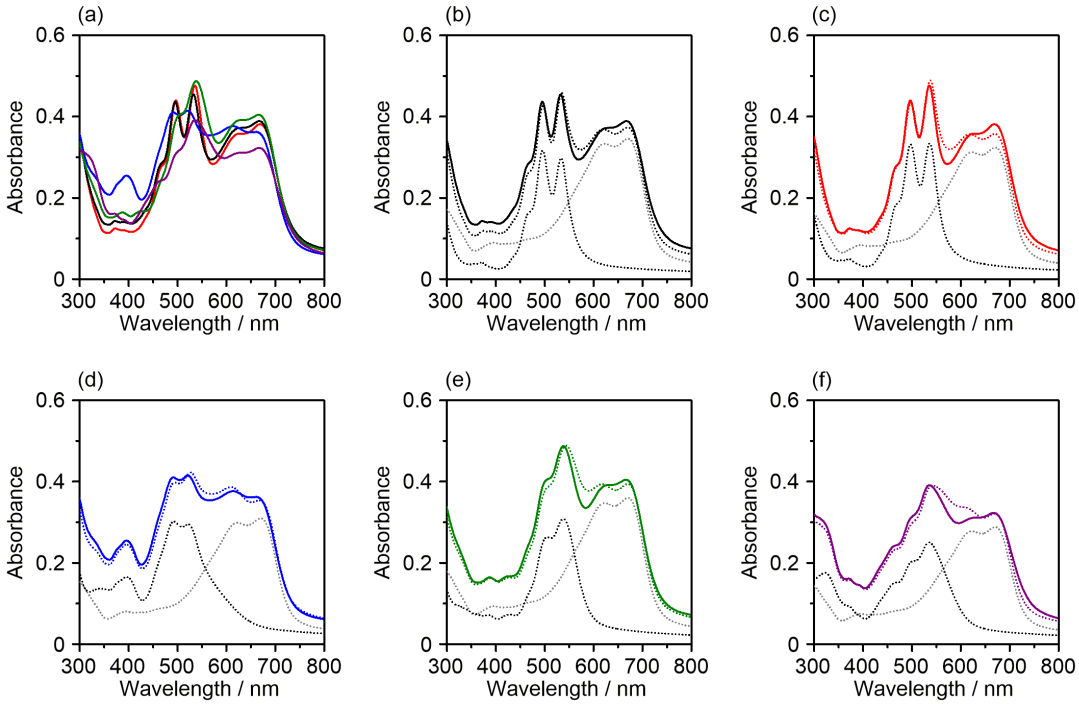

Figure 4.10. (a) UV-vis absorption spectra of PTB7/**TetraBP-*N*-PDIC9** (black), PTB7/**TetraBP-*N*-PDIC2** (red), PTB7/**Pyrene-*B*-PDI** (blue), PTB7/**TetraP-*B*-PDI** (green), and PTB7/**SpiroF-*B*-PDI** (purple) blended films. (b–f) UV-vis absorption spectra of PTB7/acceptor blended films (solid line), PTB7 (gray dotted line), acceptor (black dotted line), and summed spectra of PTB7 and acceptor (colored dotted line).

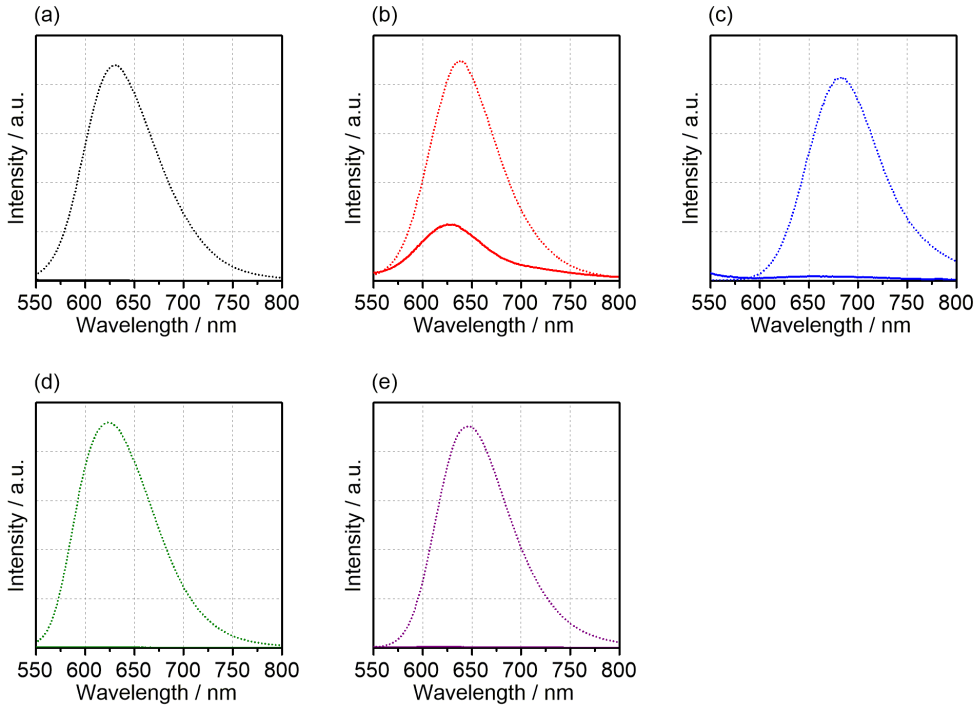

Figure 4.11. Photoluminescence spectra of the PTB7/acceptor blended films (solid line) and acceptor pristine films (dotted line) for (a) **TetraBP-*N*-PDIC9**, (b) **TetraBP-*N*-PDIC2**, (c) **Pyrene-*B*-PDI**, (d) **TetraP-*B*-PDI**, and (e) **SpiroF-*B*-PDI**.

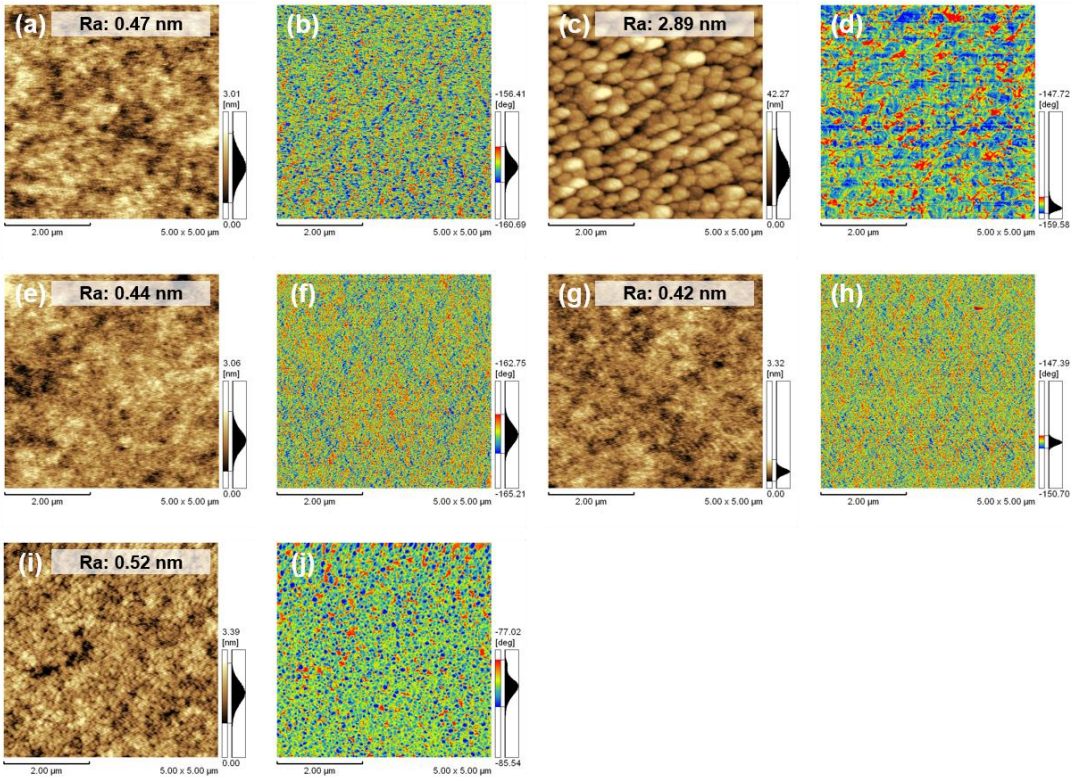

Figure 4.12. AFM height and phase images of (a, b) PTB7/**TetraBP-*N*-PDIC9**, (c, d) PTB7/**TetraBP-*N*-PDIC2**, (e, f) PTB7/**Pyrene-*B*-PDI**, (g, h) PTB7/**TetraP-*B*-PDI**, and (i, j) PTB7/**SpiroF-*B*-PDI** blended films.

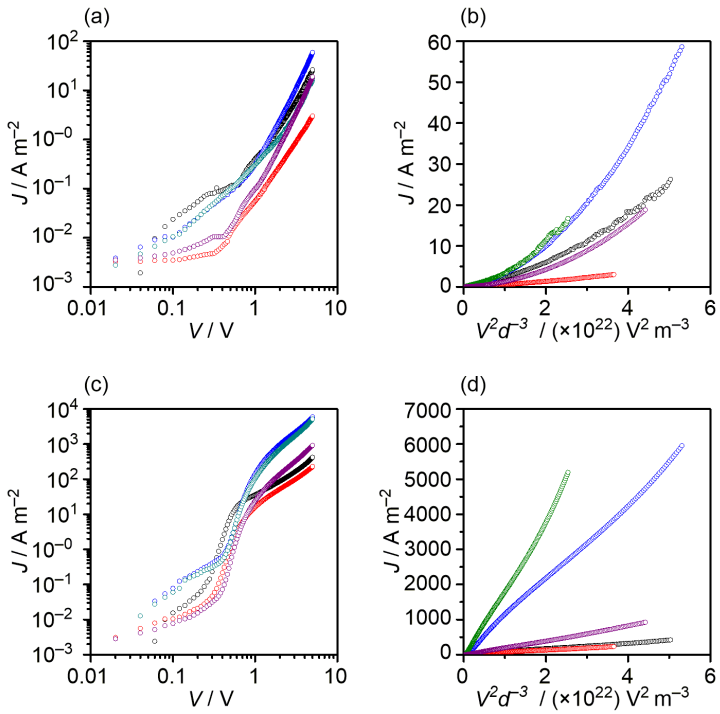

Figure 4.13. (a) *J*–*V* and (b) *J*–V^2 d^{-3} characteristics of electron-only devices and (c) *J*–*V* and (d) *J*–V^2 d^{-3} characteristics of hole-only devices for PTB7/**TetraBP-*N*-PDIC9** (black), PTB7/**TetraBP-*N*-PDIC2** (red), PTB7/**Pyrene-*B*-PDI** (blue), PTB7/**TetraP-*B*-PDI** (green), and PTB7/**SpiroF-*B*-PDI** (purple) blended films.

Table 4.5. OPV characteristics and properties of PTB7/PDI-based acceptor blend films.

Blend films	μ_e [cm^2 V^{-1} s^{-1}]	μ_h [cm^2 V^{-1} s^{-1}]	PLQE [%]
PTB7/**TetraBP-N-PDIC9**	1.5×10^{-8}	2.0×10^{-7}	100
PTB7/**TetraBP-N-PDIC2**	2.9×10^{-8}	8.7×10^{-8}	74
PTB7/**Pyrene-B-PDI**	1.9×10^{-7}	5.4×10^{-7}	98
PTB7/**TetraP-B-PDI**	8.7×10^{-8}	1.0×10^{-6}	100
PTB7/**SpiroF-B-PDI**	1.1×10^{-7}	5.7×10^{-8}	100

maximum of acceptors (520–540 nm) are shown in Figure 4.11. The intensities are normalized against the absorbances of the acceptor components, which were determined from the ratio of donors and acceptors in the UV-vis absorption spectra (Figure 4.10), which show the sums of the donor and acceptor spectra. Although the PLQE of the PTB7/**TetraBP-*N*-PDIC2** blend film was found to be 74%, the other blend films were mostly quenched (Table 4.5). The AFM images of PTB7/**TetraBP-*N*-PDIC2** mixed film showed the formation of large grains, while the other blended films showed favorable smooth surfaces (Figure 4.12). The formation of unfavorable grain structure result in the relatively low PLQE for PTB7/**TetraBP-*N*-PDIC2** film. The almost quantitative PLQEs observed for the other four blend films can be explained by efficient photo-induced hole-transfer from the acceptors to PTB7, implying that the η_{ED} and η_{CT} are high enough in these blended films.

To characterize the η_{CC}, SCLC of the blended films were measured with the device structures of ITO/TiO_x/active layer/Ca/Al and ITO/PEDOT:PSS/active layer/Au for electron and hole only devices, respectively.[12] The *J*–*V* and J–V^2d^{-3} characteristics are shown in Figure 4.13, and estimated electron and hole mobilities are listed in Table 4.5. Among the acceptors investigated in this study, PTB7/**Pyrene-*B*-PDI** film showed the highest electron mobility. Thanks to the high electron mobility, balanced electron and hole mobilities were achieved for PTB7/**Pyrene-*B*-PDI** film, which showed the highest J_{SC} value on the OPV device. However, among the other acceptors, no clear trend between SCLC mobilities and J_{SC} values was found, indicating that the influence of η_{CC} on the photovoltaic characteristics is restricted.

In chapter 3, the correlation between the γ^d and the J_{SC} of OPV devices was discussed using the linearly extended non-fullerene acceptors, and proposed that the acceptors with large γ^d lead to increase the amount of π-conjugated framework exposed to the D–A interface, which is advantageous to the η_{CS}. To reveal whether this correlation can be applied to the present three-dimensional acceptors, SFE, γ^d, and γ^p of **TetraBP-*N*-PDIC9**, **TetraBP-*N*-PDIC2**, **Pyrene-*B*-PDI**, **TetraP-*B*-PDI**, and **SpiroF-*B*-PDI** were determined from the contact-angle measurements using θ_{water} and $\theta_{glycerol}$ as probe liquids (Table 4.6). As can be seen in Figure 4.14(a), a plot of the γ^d against the J_{SC} also showed a similar correlation to the linear acceptors. For the same π-conjugated structures (**TetraBP-*N*-PDIC9** versus **TetraBP-*N*-PDIC2**), the γ^d was increased by a shortening of the alkyl chain, and, in spite of the low PLQE of **Tetra-*N*-PDIC2**, the J_{SC} value of OPV using this acceptor was increased in correspondence to the larger γ^d value. The γ^ds of **Pyrene-*B*-PDI**, **TetraP-*B*-PDI**, and **SpiroF-*B*-PDI** were larger than those of **TetraBP-*N*-PDIC9** and **TetraBP-*N*-PDIC2**, indicating that the attachment of PDI unit at the bay-position is effective for an increase in the γ^d (Figure 4.14(b)). These results indicate that the exposure of PDI frameworks to the D–A interface is desirable for efficient charge separation, and, furthermore, this effect dominantly determines the OPV performances

Table 4.6. Contact angles and calculated surface free energy data of PDI-based acceptor films.

Compounds	θ_{water} [°]	$\theta_{grycerol}$ [°]	γ^d [mJ cm^{-2}]	γ^p [mJ cm^{-2}]	SFE [mJ cm^{-2}]
TetraBP-*N*-PDIC9	98.1	92.7	8.0	6.4	14.4
TetraBP-*N*-PDIC2	80.0	72.1	15.4	11.7	27.1
Pyrene-*B*-PDI	88.9	74.2	25.2	3.7	28.9
TetraP-*B*-PDI	89.0	71.5	30.7	2.5	33.2
SpiroF-*B*-PDI	90.7	71.6	33.8	1.5	35.3

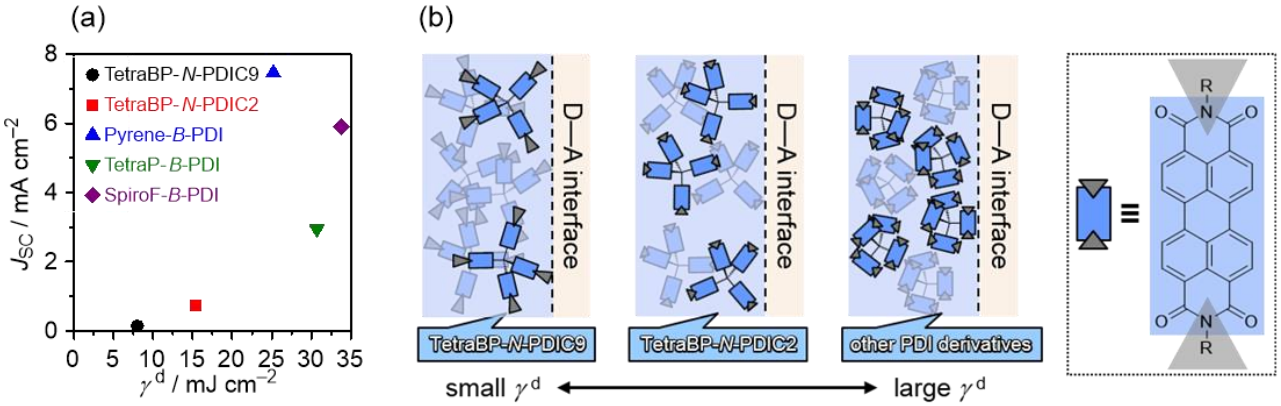

Figure 4.14. (a) Plot of γ^d vs. J_{SC} values for acceptor materials used in this study. (b) Graphical representation of the molecular orientation at donor–acceptor interfaces.

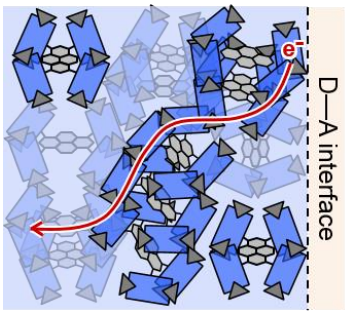

Figure 4.15. Graphical representation of the molecular arrangement and electron transport in the **Pyrene-*B*-PDI** phase of D–A interface.

of our investigated PDI-based acceptors. In addition to this, despite the moderate γ^d value of **Pyrene-*B*-PDI** compared with those of **TetraP-*B*-PDI** and **SpiroF-*B*-PDI**, the high electron mobility and highest J_{SC} value of the **PTB7/Pyrene-*B*-PDI** film compared with those of the other blend films suggests that the large, flat pyrene core (instead of the tetrahedral core of the other acceptors) effectively contribute to the construction of carrier transport pathways (Figure 4.15). The correlation between γ^d of acceptor films and J_{SC} of OPVs support the importance of molecular design toward the control of acceptor unit orientation at D–A interface.

4.4 Conclusion

In summary, the author investigated the structure–properties–OPV characteristics of three-dimensional non-fullerene acceptors having PDIs as electron-accepting transporting units to reveal the influence of structural

modification on the characteristics of D–A interface in the BHJ active films. Thermal and photophysical properties as well as molecular energy levels of these compounds did not show apparent differences. On the other hand, OPV characteristics based on PTB7 and these acceptors resulted in a broad distribution of PCEs between 0.02% and 2.02%, which originates from the difference of J_{SC} values. Absorption spectra, photoluminescence spectra, and SCLC mobilities of these BHJ films were measured to consider the origin of this significant difference of J_{SC}. These measurements indicated that the efficiency of charge-separation process has a main influence on the photovoltaic characteristics. As expected, a correlation was found between the J_{SC} of OPVs and the γ^{d} components of SFE for the three-dimensional acceptors. Since an increase of exposed π-conjugated framework at the interface leads to the increase of γ^{d} values, this correlation indicates that the orientation of PDI π-plane toward D–A interfaces is desirable for the efficient charge separation into free carrier. These results imply that the fine-tuning of molecular structure contributes to the construction of appropriate D–A interfaces in the BHJ films. Importantly, the estimation of γ^{d} values becomes an useful guideline for molecular design in terms of molecular arrangement manipulation in the BHJ films.

4.5 Experimental Section

Supplemental Figures and Tables

Table S1. OPV characteristics of PTB7/**TetraBP-*N*-PDIC9** based devices.

Run	J_{SC} [mA/cm^{-2}]	V_{OC} [V]	FF	PCE [%]
1	0.14	0.39	0.29	0.02
2	0.12	0.38	0.32	0.01
3	0.12	0.38	0.31	0.01
4	0.13	0.36	0.32	0.01
average	0.13 ± 0.00	0.38 ± 0.01	0.31 ± 0.01	0.01 ± 0.00

Table S2. OPV characteristics of PTB7/**TetraBP-*N*-PDIC2** based devices.

Run	J_{SC} [mA/cm^{-2}]	V_{OC} [V]	FF	PCE [%]
1	0.74	0.65	0.27	0.13
2	0.74	0.61	0.26	0.12
3	0.68	0.56	0.26	0.10
4	0.65	0.55	0.25	0.09
average	0.70 ± 0.02	0.59 ± 0.02	0.26 ± 0.00	0.11 ± 0.01

Table S3. OPV characteristics of PTB7/**Pyrene-*B*-PDI** based devices.

Run	J_{SC} [mA/cm^{-2}]	V_{OC} [V]	FF	PCE [%]
1	7.65	0.72	0.37	2.02
2	7.49	0.72	0.37	1.97
3	7.44	0.72	0.37	1.96
4	6.61	0.72	0.36	1.72
average	7.30 ± 0.23	0.72 ± 0.02	0.37 ± 0.02	1.92 ± 0.07

Table S4. OPV characteristics of PTB7/**TetraP-*B*-PDI** based devices.

Run	J_{SC} [mA/cm^{-2}]	V_{OC} [V]	FF	PCE [%]
1	2.94	0.74	0.30	0.65
2	2.95	0.75	0.29	0.64
3	2.96	0.74	0.30	0.64
4	2.73	0.74	0.30	0.60
average	2.90 ± 0.06	0.74 ± 0.00	0.30 ± 0.00	0.63 ± 0.01

Table S5. OPV characteristics of PTB7/**SpiroF-*B*-PDI** based devices.

Run	J_{SC} [mA/cm^{-2}]	V_{OC} [V]	FF	PCE [%]
1	5.90	0.75	0.36	1.57
2	6.07	0.74	0.35	1.56
3	5.83	0.75	0.35	1.56
4	5.96	0.75	0.34	1.54
average	5.94 ± 0.05	0.75 ± 0.00	0.35 ± 0.00	1.56 ± 0.01

Summarized Results for cyano-substituted benzothiadiazole-based acceptors

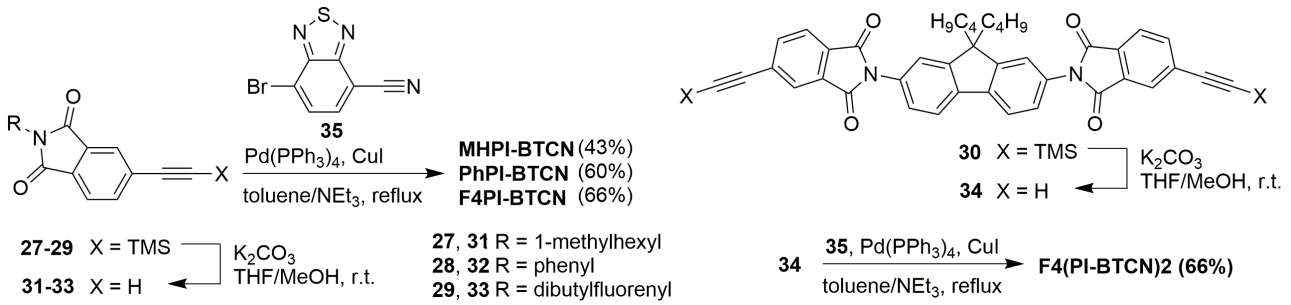

Scheme S4.1. Synthesis of cyano-substituted benzothiadiazole-based acceptors.

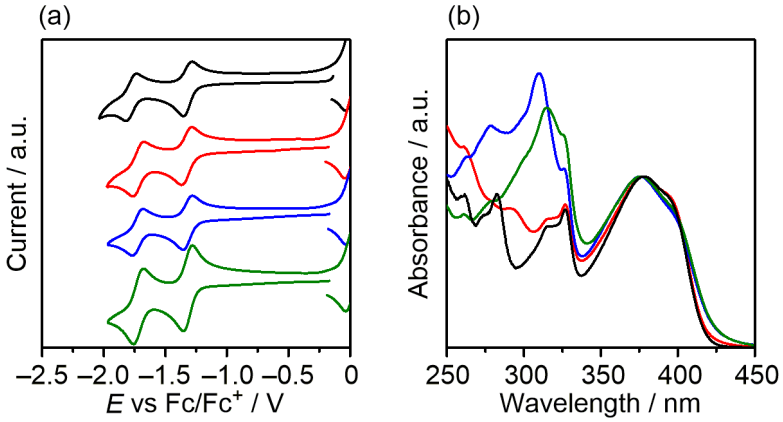

Figure S4.1. (a) Cyclic voltammograms and (b) UV-Vis absorption spectra of **MHPI-BTCN** (black), **PhPI-BTCN** (red), **F4PI-BTCN** (blue), and **F4(PI-BTCN)2** (green) in solution.

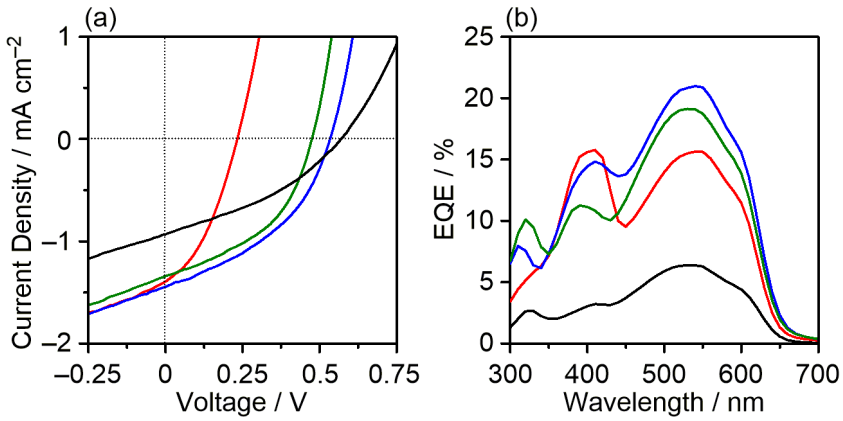

Figure S4.2. (a) *J-V* curves and (b) EQE spectra for P3HT/**MHPI-BTCN** (black), P3HT/**PhPI-BTCN** (red), P3HT/**F4PI-BTCN** (blue), and P3HT/**F4(PI-BTCN)2** (green) OPV devices.

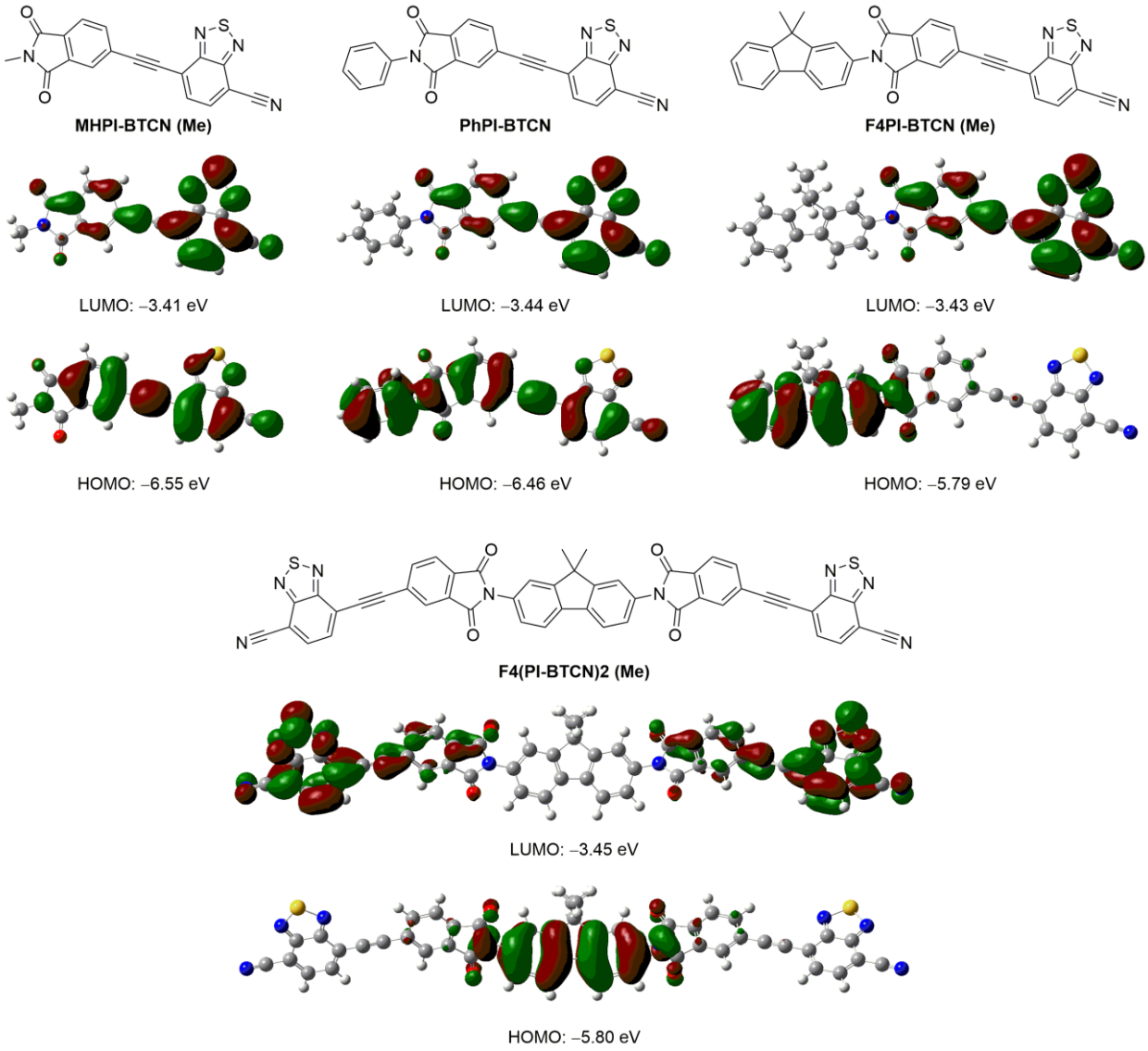

Figure S4.3. Energy levels and molecular orbitals of cyano-substituted benzothiadiazole-based acceptors. All the alkyl groups were replaced with methyl groups to facilitate the calculation.

Summarized Results for asNTz-NP-R

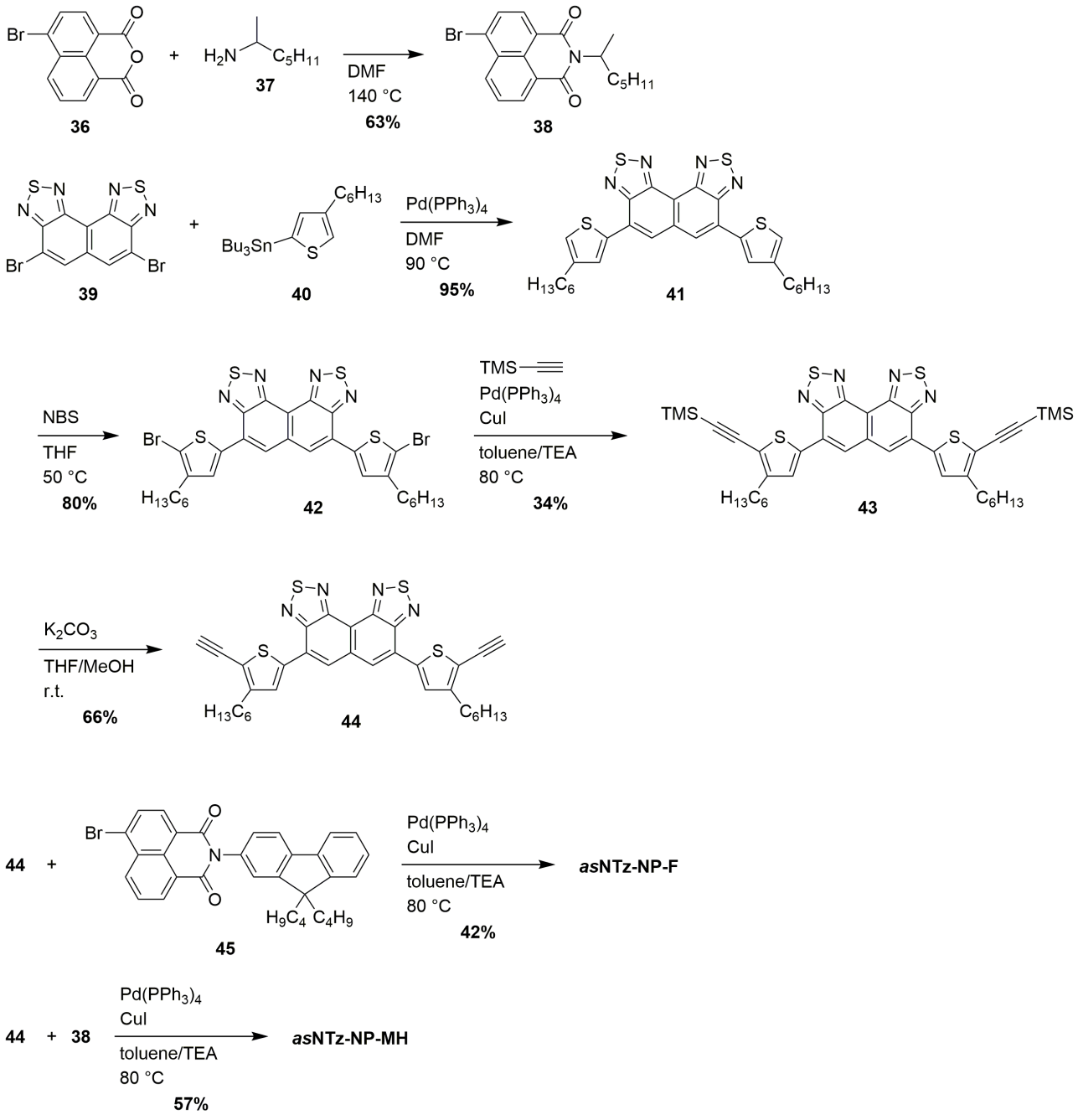

Scheme S4.2. Synthesis of ***as*NTz-NP-F** and ***as*NTz-NP-MH**.

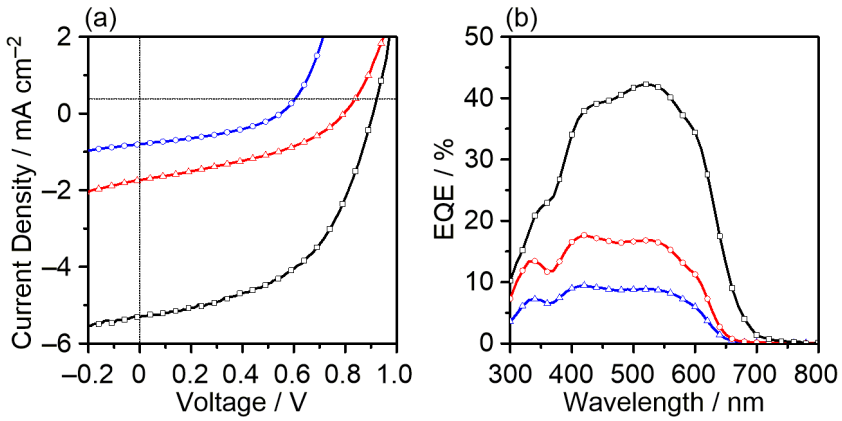

Figure S4.4. (a) *J*–*V* curves and (b) EQE spectra for P3HT/***as*NTz-NP-F** (red), P3HT/***as*NTz-NP-MH** (blue), and P3HT/***s*NTz-NP-F** (black) OPV devices.

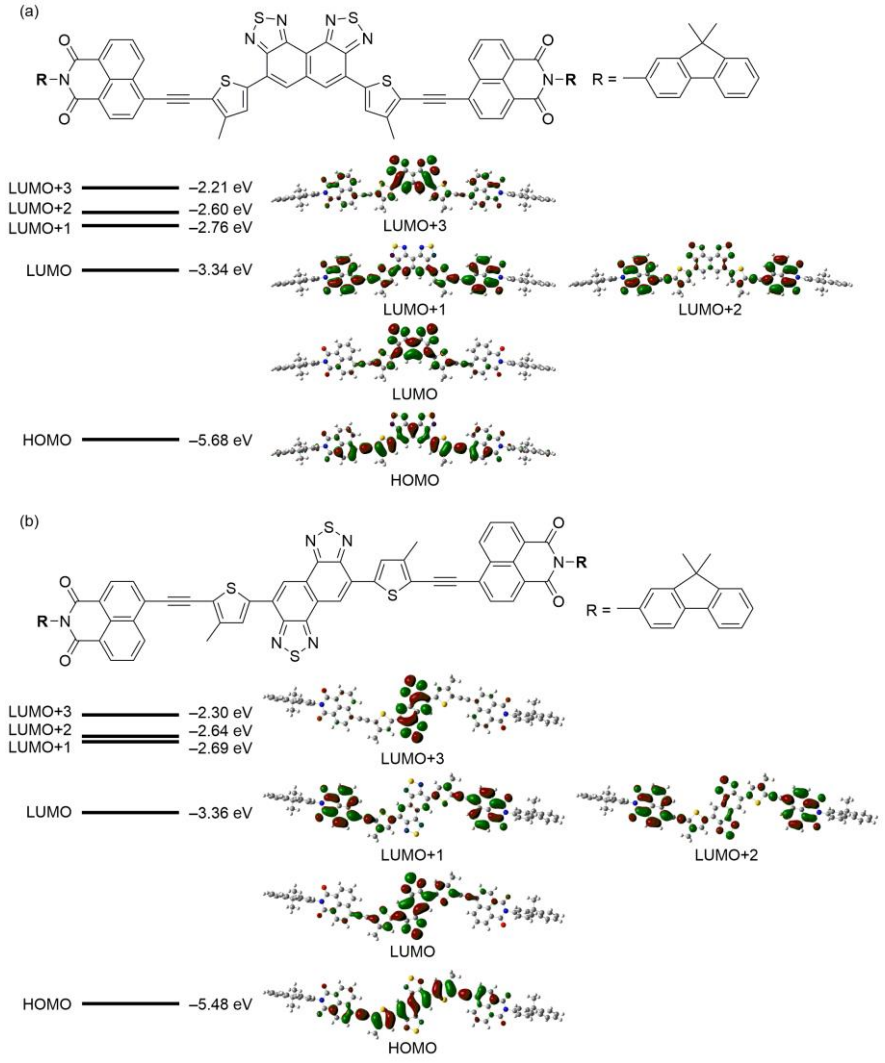

Figure S4.5. Energy levels and molecular orbitals of (a) ***as*NTz-NP-F** and (b) ***s*NTz-NP-F** calculated by DFT at B3LYP/6-31 G(d,p) level. All the alkyl groups were replaced with methyl groups to facilitate the calculation.

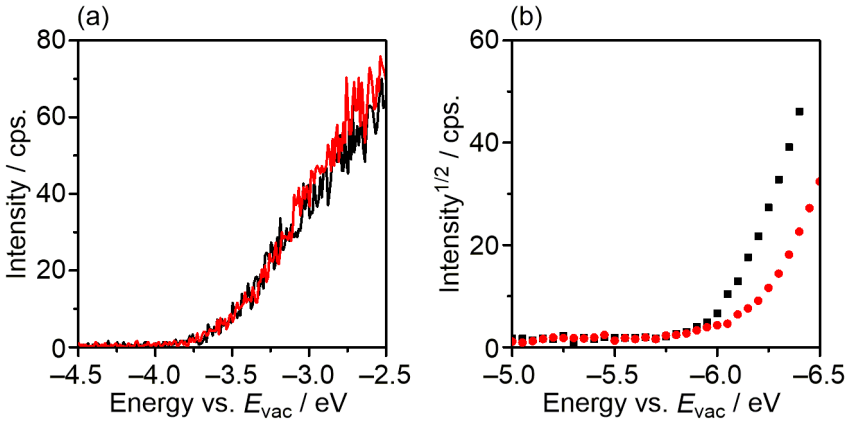

Figure S4.6. (a) LEIPS and (b) PESA of ***as*NTz-NP-F** (red) and ***s*NTz-NP-F** (black).

General Information

Column chromatography was performed on silica gel, KANTO Chemical silica gel 60N (40–50 μm). TLC plates were visualized with UV light. Preparative GPC was performed on a Japan Analytical Industry LC-918 equipped with JAI-GEL 1H/2H. ^{1}H and ^{13}C NMR spectra were recorded on a JEOL ECS-400 spectrometer. Data are reported as follows: chemical shift in ppm (δ), multiplicity (s = singlet, d = doublet, t = triplet, m = multiplet, br = broad), coupling constant (Hz). Mass spectra were obtained on a Shimadzu GCMS-QP-5050 or Shimadzu AXIMA-TOF. High-resolution mass spectrum (HRMS) was obtained using a Brucker ultraflex III (MALDI-TOF) or Brucker microTOF II (ESI-TOF). Elemental analyses were performed on Perkin Elmer LS-50B by the Elemental Analysis Section of CAC, ISIR, Osaka University. DSC and TGA were performed under nitrogen at a heating rate of 10 °C min^{-1} with a Shimadzu DSC-60 and a Shimadzu TGA-50, respectively. UV-Vis spectra were recorded on a Shimadzu UV-3600 spectrophotometer. PESA was carried out using a Riken Keiki Co. Ltd. AC-3 with a light intensity of 20 mW. Fluorescence spectra were recorded using a Fluoromax-4 spectrometer in the photo-counting mode equipped with a Hamamatsu R928P photomultiplier. The bandpass for the emission spectra was 1.0 nm. All spectra were obtained in spectrograde solvents. The surface structures of the deposited organic films were observed by atomic force microscopy (Shimadzu, SPM9600).

OPV Device Fabrication and Evaluation

Organic photovoltaic devices were prepared with a structure of ITO/PEDOT:PSS/active layer/Ca/Al. ITO-coated glass substrates were first cleaned by ultrasonication in toluene, acetone, water, and 2-propanol for 10 min, respectively. ITO-coated glass substrates were then activated by ozone treatment for 1 h. PEDOT:PSS was spin-coated on the ITO surface at 3000 rpm for 1 min and dried at 135 °C for 10 min. The active layers were then prepared by spin-coating on the ITO/PEDOT:PSS electrode at 1000 rpm for 2 min in a glove box. The typical thickness of the active layer was 60–90 nm. Ca and Al electrode were evaporated on the top of active layer through a shadow mask to define the active area of the devices (0.09 cm^2) under a vacuum of 10^{-5} Pa to a thickness of 30, 100 nm determined by a quartz crystal monitor. After sealing the device from the air, the photovoltaic characteristics were measured in air under simulated AM 1.5G solar irradiation (100 mW cm^{-2}) (SAN-EI ELECTRIC, XES-301S). The current density–voltage characteristics of photovoltaic devices were measured by using a KEITHLEY 2400 source

meter. The EQE spectra were measured by using a Soma Optics Ltd. S-9240. The thickness of active layer was determined by KLA Tencor Alpha-step IQ.

LEIPS Measurements

Experimental setup for the LEIPS is described elsewhere.[13] Sample films were incident to an electron beam with the kinetic energy in the range between 0 and 4 eV and the emitted photons were detected with an optical bandpass filter and a photomultiplier to obtain the LEIPS sepctrum. The electron affinities (EA) were determined as the onset energy of LEIPS spectrum with reference to the vaccuum level. EA were measured at two photon energies by changing the bandpass filter with the center wavelength of 260 and 285 nm.[9]

SCLC Measurements

Hole-only and electron-only devices were prepared with a structure of ITO/PEDOT:PSS/active layer/Au and ITO/TiO_x/active layer/Ca/Au, respectively.[12] The active layers were prepared from 10 mg mL^{-1} solution of materials in chloroform. The carrier mobilities of these devices were calculated by the following equation:

$$J = \frac{9}{8}\varepsilon\varepsilon_0\mu\frac{V^2}{d^3}$$

where ε, ε_0, μ, and d are the dielectric constant of the active layer, the permittivity of free space, the carrier mobility, and the measured thickness of active layer, respectively. We used the values of $\varepsilon = 3$, $\varepsilon_0 = 8.8 \times 10^{-12}$ F/m.

PLQE Estimation

Acceptor pristine films and PTB7/acceptor blended films were prepared on the quartz substrate by spin-coating using 10 mg mL^{-1} $CHCl_3$ solution, and the UV-vis absorption spectra and emission spectra were recorded, respectively. PLQE of blended films were calculated using following equation:

$$\mathrm{PLQE} = 1 - \frac{\phi_{p:n}}{\phi_p}$$

where Φ_p and $\Phi_{p:n}$ are the normalized photoluminescence intensities of pristine films using absorbed photons at λ_{max} and the normalized photoluminescence intensities of blended films against relative ratio of acceptor component, respectively.

Surface Free Energy Estimation

The contact angles of film surface were measured by a NiCK LSE-ME1 using distilled water and glycerol. SFEs were estimated based on the theory established by Kaelble and Uy.[14]

Materials

All reactions were carried out under a nitrogen atmosphere. Solvents of the highest purity grade were used as received. All reagents were purchased from commercial sources and used without purification. **22**,[15] **23**,[16] **24**,[17] **25**,[18] **26**,[19] **35**,[20] **39**,[21] **40**,[22] and **45**[2] was prepared by our previously reported procedure and ^{1}H NMR data of these compounds were in agreement with those previously reported.

Synthesis

*Synthesis of **TetraBP-N-PDIC2***: **22** (50 mg, 0.061 mmol), **23** (241 mg, 0.364 mmol), $Pd(PPh_3)_4$ (14 mg, 0.012 mmol), and K_2CO_3 (168 mg, 1.21 mmol) were placed in a test tube with screw cap and dissolved with toluene (10 mL), H_2O (2 mL), and EtOH (1mL). The reaction mixture was stirred at 85 °C for 12 h. After being cooled to room temperature and addition of water, the resulting mixture was extracted with $CHCl_3$ and the organic layer was washed with water. After removal of the solvent under reduced pressure, the residue was purified by column chromatography on silica gel ($CHCl_3$), followed by purification with preparative GPC ($CHCl_3$) to give **TetraBP-*N*-PDIC2** (57 mg, 38%). Deep red solid; ^{1}H NMR (400 MHz, 1,1,2,2-tetrachloroethane-d_2, 100 °C, δ): 8.76-8.59 (m, 32H), 7.92-7.83 (m, 8H), 7.75-7.68 (m, 8H), 7.58-7.51 (m, 8H), 7.50-7.43 (m, 8H), 5.08-5.00 (m, 4H), 2.30-2.21 (m, 8H), 2.03-1.95 (m, 8H), 1.55-1.44 (m, 12H), 0.99-0.95 (m, 12H); MS (MALDI-TOF, 1,8,9-trihydroxyanthracene matrix) *m/z* 2456.75 (M^-); HRMS (MALDI-TOF) *m/z* calcd for $C_{165}H_{108}N_8O_{16}$ (M^-): 2457.7917, found: 2457.7913.

*Synthesis of **Pyrene-B-PDI***: **24** (40 mg, 0.057 mmol), **25** (207 mg, 0.400 mmol), $Pd(PPh_3)_4$ (13 mg, 0.011 mmol), and K_2CO_3 (157 mg, 1.13 mmol) were placed in a test tube with screw cap and dissolved with toluene (10 mL), H_2O (2 mL), and EtOH (1mL). The reaction mixture was stirred at 80 °C for 24 h. After being cooled to room temperature and addition of water, the resulting mixture was extracted with $CHCl_3$ and the organic layer was washed with water. After removal of the solvent under reduced pressure, the residue was purified by column chromatography on silica gel ($CHCl_3$), followed by purification with preparative GPC ($CHCl_3$) to give **Pyrene-*B*-PDI** (50 mg, 38%). Deep red solid; ^{1}H NMR (400 MHz, 1,1,2,2-tetrachloroethane-d_2, 140 °C, δ): 8.77-8.52 (m, 20H), 8.34-8.31 (m, 2H), 8.28-7.96 (m, 10H), 7.73-7.62 (m, 1H), 7.29-7.27 (s, 1H), 5.06-4.84 (m, 8H), 2.23-2.13 (m, 8H), 2.00-1.85 (m, 12H), 1.49-1.34 (m, 12H), 0.97-0.66 (m, 48H); MS (MALDI-TOF, 1,8,9-trihydroxyanthracene matrix) *m/z* 2315.36 (M^-); Anal. calcd for $C_{152}H_{122}N_8O_{16}$: C 78.81, H 5.31, N 4.84; found: C 78.58, H 5.45, N 4.71.

*Synthesis of **TetraP-B-PDI***: **22** (40 mg, 0.049 mmol), **25** (177 mg, 0.291 mmol), $Pd(PPh_3)_4$ (11 mg, 0.010 mmol), and K_2CO_3 (134 mg, 0.97 mmol) were placed in a test tube with screw cap and dissolved with toluene (10 mL), H_2O (2 mL), and EtOH (1mL). The reaction mixture was stirred at 80 °C for 24 h. After being cooled to room temperature and addition of water, the resulting mixture was extracted with $CHCl_3$ and the organic layer was washed with water. After removal of the solvent under reduced pressure, the residue was purified by column chromatography on silica gel ($CHCl_3$), followed by purification with preparative GPC ($CHCl_3$) to give **TetraP-*B*-PDI** (52 mg, 44%). Deep red solid; ^{1}H NMR (400 MHz, $CDCl_3$, 50 °C, TMS, δ): 8.73–8.59 (m, 20H), 8.00–7.96

(m, 8H), 7.72–7.65 (m, 16H), 5.10–5.02 (m, 4H), 4.77–4.67 (m, 4H), 2.31–2.20 (m, 8H), 1.96–1.85 (m, 16H), 1.68–1.58 (m, 8H), 0.93 (t, J = 7.4 Hz, 24H), 0.65 (t, J = 6.0 Hz, 24H); ^{13}C NMR (100 MHz, $CDCl_3$, 50 °C, δ): 164.38, 164.33, 164.14, 164.06, 146.57, 141.61, 141.13, 135.97, 135.93, 134.97, 134.92, 134.58, 133.15, 132.89, 131.16, 131.03, 129.95, 129.73, 129.70, 129.63, 129.61, 129.28, 128.82, 128.63, 128.24, 127.77, 123.52, 122.70, 65.00, 57.85, 57.46, 25.12, 24.85, 11.29, 11.15; MS (MALDI-TOF, 1,8,9-trihydroxyanthracene matrix) *m/z* 2344.33 (M^-); HRMS (MALDI-TOF) *m/z* calcd for $C_{161}H_{132}N_8O_{16}$ (M^-): 2433.9795, found: 2433.9800.

Synthesis of ***SpiroF-B-PDI***: **26** (40 mg, 0.049 mmol), **25** (178 mg, 0.293 mmol), $Pd(PPh_3)_4$ (11 mg, 0.010 mmol), and K_2CO_3 (135 mg, 0.98 mmol) were placed in a test tube with screw cap and dissolved with toluene (10 mL), H_2O (2 mL), and EtOH (1mL). The reaction mixture was stirred at 80 °C for 24 h. After being cooled to room temperature and addition of water, the resulting mixture was extracted with $CHCl_3$ and the organic layer was washed with water. After removal of the solvent under reduced pressure, the residue was purified by column chromatography on silica gel ($CHCl_3$), followed by purification with preparative GPC ($CHCl_3$) to give **SpiroF-*B*-PDI** (48 mg, 40%). Deep red solid; ^{1}H NMR (400 MHz, 1,1,2,2-tetrachloroethane-d_2, 140 °C, δ): 8.68-8.44 (m, 20H), 7.99-7.96 (m, 4H), 7.80-7.65 (m, 6H), 7.50 (s, 4H), 7.44-7.25 (m, 6H), 5.05-4.96 (m, 4H), 4.69-4.61 (m, 4H), 2.26-2.16 (m, 8H), 1.98-1.72 (m, 16H), 1.47-1.39 (m, 8H), 0.98-0.91 (m, 24H), 0.80-0.74 (m, 24H); MS (MALDI-TOF, 1,8,9-trihydroxyanthracene matrix) *m/z* 2429.19 (M^-); MS MALDI-TOF (1,8,9-trihydroxyanthracene matrix) *m/z* 2429.19 (M^-); HRMS (ESI-TOF) *m/z* calcd for $C_{161}H_{128}N_8O_{16}$ (M^-): 2429.9482, found: 2429.9490.

Synthesis of ***27***: 4-Bromo-*N*-(2-heptyl)phthalimide (1.00 g, 3.08 mmol), trimethylsilylacetylene (1.21 g, 12.3 mmol), $Pd(PPh_3)_4$ (356 mg, 0.31 mmol), and CuI (59 mg, 0.31 mmol) were placed in a test tube with screw cap and dissolved with THF (10 mL) and triethylamine (10 mL). The reaction mixure was refluxed for 12 h. After being cooled to room temperature, the reaction mixture was concentrated under reduced pressure and then purified by column chromatography on silica gel (hexane/$CHCl_3$=1/1) to give **27** (1.04 g, 99%). White solid; ^{1}H NMR (400 MHz, $CDCl_3$, TMS): δ 7.86 (s, 1H), 7.76 (d, 1H, J = 7.8 Hz), 7.74 (d, 1H, J = 7.8 Hz), 4.33 (m, 1H), 2.03 (m, 1H), 1.73 (m, 1H), 1.45 (d, 3H, J = 6.9 Hz), 1.30-1.20 (br, 6H), 0.85 (t, 3H, J = 7.3 Hz), 0.27 (s, 9H); ^{13}C NMR (100 MHz, $CDCl_3$): δ 168.21, 168.07, 137.35, 132.34, 131.22, 129.39, 126.58, 123.16, 103.29, 99.68, 47.92, 33.90, 31.67, 26.71, 22.77, 18.93, 14.26; MS (EI): *m/z* calcd for $[M]^+$: 341. Found: 341; Anal. calcd for $C_{20}H_{27}NO_2Si$: C, 70.34; H, 7.97; N, 4.10. Found: C, 70.41; H, 7.87; N, 3.98.

Synthesis of ***31***: To a stirred solution of **27** (1.04 g, 3.05 mmol) in THF (10 mL) and methanol (2.5 mL) was added K_2CO_3 (853 mg, 3.08 mmol), and the resulting mixture was stirred at room temperature for 1 h. After filtration over celite and removal of the solvent under reduced pressure, the residue was isolated by column chromatography on silica gel (hexane/$CHCl_3$=1/1) to give **31** (790 mg, 96%). White solid; ^{1}H NMR (400 MHz, $CDCl_3$, TMS): δ 7.89 (d, 1H, J = 0.9 Hz), 7.79 (dd, 1H, J = 7.8, 0.9 Hz), 7.77 (dd, 1H, J = 7.8, 0.9 Hz), 4.33 (m, 1H), 3.31 (s, 1H), 2.03 (m, 1H), 1.71 (m, 1H), 1.46 (d, 3H, J = 6.9 Hz), 1.30-1.20 (br, 6H), 0.84 (t, 3H, J = 7.3 Hz). This compound was used for next step without further purification.

*Synthesis of **MHPI-BTCN***: **31** (73 mg, 0.27 mmol), **35** (65 mg, 0.27 mmol), $Pd(PPh_3)_4$ (31 mg, 0.027 mmol), and CuI (5.1 mg, 0.027 mmol) were placed in a test tube with screw cap and dissolved with THF (2 mL) and triethylamine (2 mL). The reaction mixture was refluxed for 24 h. After being cooled to room temperature, the reaction mixture was concentrated under reduced pressure and then purified by column chromatography on silica gel (hexane/AcOEt=5/1), followed by recrystallization using MeOH to give **MHPI-BTCN** (50 mg, 43%). Yellow solid; ^{1}H NMR (400 MHz, $CDCl_3$, TMS): δ 8.09 (s, 1H), 8.07 (d, 1H, *J* = 7.3 Hz), 7.99 (dd, 1H, *J* = 7.8 Hz), 7.90 (d, 1H, *J* = 7.3 Hz), 7.88 (d, 1H, *J* = 7.8 Hz), 4.36 (m, 1H), 2.05 (m, 1H), 1.74 (m, 1H), 1.48 (d, 3H, *J* = 6.9 Hz), 1,30-1.23 (br, 6H), 0.85 (t, 3H, 6.4 Hz); ^{13}C NMR (100 MHz, $CDCl_3$): δ 167.68, 167.53, 153.94, 152.70, 137.36, 135.33, 132.39, 132.06, 131.83, 127.57, 126.48, 123.27, 121.50, 114.98, 106.19, 98.02, 87.68, 47.86, 33.63, 31.39, 26.46, 22.50, 18.67, 14.00; MS (EI): *m/z* calcd for $[M]^+$: 428. Found: 428; HRMS (APCI): m/z calcd for $C_{24}H_{21}N_4O_2S$ ($[M+H]^+$): 429.1385. Found: 429.1375.

*Synthesis of **28***: **28** was synthesized from 4-bromo-*N*-phenylphthalimide and trimethylsilylacetylene with a yield of 67% by following the procedure used for the preparation of **27**. This compound was purified by column chromatography on silica gel (hexane/AcOEt=4/1). White solid; ^{1}H NMR (400 MHz, $CDCl_3$, TMS): δ 8.00 (d, 1H, *J* = 1.4 Hz), 7.89 (d, 1H, *J* = 7.8 Hz), 7.84 (dd, 1H, *J* = 7.8, 1.4 Hz), 7.51 (t, 2H, *J* = 7.6 Hz), 7.42 (d, 2H, *J* = 7.6 Hz), 7.41 (t, 1H, *J* = 7.6 Hz); ^{13}C NMR (100 MHz, $CDCl_3$): δ 166.67, 166.57, 137.63, 131.84, 131.50, 130.62, 130.07, 129.79, 129.15, 128.21, 126.99, 126.48, 126.44, 123.62, 102.80, 100.14; MS (EI): *m/z* calcd for $[M]^+$: 319. Found: 319; Anal. calcd for $C_{19}H_{17}NO_2Si$: C, 71.44; H, 5.36; N, 4.38. Found: C, 71.23; H, 5.53; N, 4.40.

*Synthesis of **32***: **32** was synthesized from compound **28** with a yield of 77% by following the procedure used for the preparation of **31**. This compound was isolated by column chromatography on silica gel (hexane/AcOEt=4/1). White solid; ^{1}H NMR (400 MHz, $CDCl_3$, TMS): δ 8.05 (s, 1H), 7.92 (d, 1H, *J* = 7.8 Hz), 7.88 (d, 1H, *J* = 7.8 Hz), 7.52 (t, 2H, *J* = 7.8 Hz), 7.43 (d, 2H, *J* = 7.8 Hz), 7.42 (t, 1H, *J* = 7.8 Hz), 3.37 (s, 1H). This compound was used for next step without further purification.

*Synthesis of **PhPI-BTCN***: **PhPI-BTCN** was synthesized from **32** and **35** with a yield of 60% by following the procedure used for the preparation of **MHPI-BTCN**. This compound was purified by column chromatography on silica gel (CH_2Cl_2) to give **PhPI-BTCN** (104 mg, 60%), followed by precipitation using $CHCl_3$ and MeOH. Yellow solid; ^{1}H NMR (400 MHz, $CDCl_3$, TMS): δ 8.24 (s, 1H), 8.09 (d, 1H, *J* = 7.8 Hz), 8.08 (d, 1H, *J* = 7.3 Hz), 8.02 (d, 1H, *J* = 7.9 Hz), 7.92 (d, 1H, *J* = 7.3 Hz), 7.54 (t, 2H, *J* = 7.4 Hz), 7.46 (d, 2H, *J* = 7.4 Hz), 7.44 (t, 1H, *J* = 7.4 Hz); ^{13}C NMR (101 MHz, $CDCl_3$): δ 166.41, 166.32, 153.92, 152.70, 137.86, 135.33, 132.15, 131.92, 131.72, 131.37, 129.23, 128.38, 128.24, 127.14, 126.47, 123.99, 121.34, 114.94, 99.91, 97.70, 88.46; MS (EI): *m/z* calcd for $[M]^+$: 406. Found: 406; HRMS (APCI): m/z calcd for $C_{23}H_{11}N_4O_2S$ ($[M+H]^+$): 407.0603. Found: 407.0590.

*Synthesis of **29***: **29** was synthesized from 4-bromo-*N*-(9,9-dibutyl-2-fluorenyl)phthalimide and trimethylsilylacetylene with a yield of 97% by following the procedure used for the preparation of **27**. This compound was purified by column chromatography on silica gel (hexane/$CHCl_3$=2/1). White solid; ^{1}H NMR (400

MHz, $CDCl_3$, TMS): δ 8.01 (s, 1H), 7.89 (d, 1H, *J* = 7.8 Hz), 7.84 (d, 1H, *J* = 7.8 Hz), 7.80 (d, 1H, *J* = 8.0 Hz), 7.72 (d, 1H, *J* = 7.2 Hz), 7.42 (s, 1H), 7.40 (d, 1H, *J* = 8.0 Hz), 7.37-7.32 (m, 3H), 1.98 (4H, t, *J* = 8.2 Hz), 1.09 (4H, m), 0.70 (6H, m, *J* = 7.3 Hz), 0.66 (m, 4H); ^{13}C NMR (100 MHz, $CDCl_3$): δ 167.12, 167.00, 151.72, 151.39, 141.14, 140.46, 137.91, 132.21, 131.01, 130.46, 130.00, 127.96, 127.17, 127.12, 125.15, 123.77, 123.22, 121.42, 120.26, 120.24, 103.14, 100.34, 55.52, 40.24, 26.23, 23.30, 14.08; MS (EI): *m/z* calcd for $[M]^+$: 519. Found: 519; HRMS (APCI): m/z calcd for $C_{34}H_{38}NO_2Si$ ($[M+H]^+$): 520.2672. Found: 520.2658.

*Synthesis of **33***: **33** was synthesized from compound **29** with a yield of 24% by following the procedure used for the preparation of **31**. This compound was isolated by column chromatography on silica gel (hexane/$CHCl_3$=2/1). White solid; ^{1}H NMR (400 MHz, $CDCl_3$, TMS): δ 8.03 (s, 1H), 7.92 (d, 1H, *J* = 7.1 Hz), 7.87 (d, 1H, *J* = 7.1 Hz), 7.80 (d, 1H, *J* = 8.6 Hz), 7.72 (d, 1H, *J* = 6.9 Hz), 7.41 (s, 1H), 7.40 (d, 1H, *J* = 8.6 Hz), 7.37-7.33 (m, 3H), 3.36 (s, 1H), 1.97 (4H, t, *J* = 8.2 Hz), 1.08 (4H, m), 0.70 (4H, m), 0.69 (t, 6H, *J* = 7.3 Hz). This compound was used for next step without further purification.

*Synthesis of **F4PI-BTCN***: **F4PI-BTCN** was synthesized from **33** and **35** with a yield of 57% by following the procedure used for the preparation of **MHPI-BTCN**. This compound was purified by column chromatography on silica gel ($CHCl_3$), followed by precipitation using $CHCl_3$ and MeOH. Yellow solid; ^{1}H NMR (400 MHz, $CDCl_3$, TMS): δ 8.24 (s, 1H), 8.09 (d, 1H, *J* = 7.3 Hz), 8.08 (d, 1H, *J* = 7.8 Hz), 8.03 (d, 1H, *J* = 7.8 Hz), 7.93 (d, 1H, *J* = 7.3 Hz), 7.83 (d, 1H, *J* = 8.7 Hz), 7.74 (d, 1H, *J* = 7.3 Hz), 7.45 (s, 1H), 7.74 (m, 1H), 7.38-7.34 (m, 3H), 1.99 (t, 4H, *J* = 8.2 Hz), 1.11 (m, 4H), 0.72-0.64 (br, 4H), 0.71 (t, 6H, *J* = 7.3 Hz); ^{13}C NMR (100 MHz, $CDCl_3$): δ 166.59, 166.48, 153.93, 152.70, 151.54, 151.13, 141.03, 140.11, 137.86, 135.34, 132.25, 131.92, 131.85, 130.03, 128.19, 127.51, 127.00, 126.93, 124.87, 123.87, 122.97, 121.37, 121.13, 120.04, 120.01, 114.95, 106.32, 97.79, 88.10, 55.27, 39.96, 25.96, 23.03, 13.82; MS (EI): *m/z* calcd for $[M]^+$: 606. Found: 606; Anal. calcd for $C_{38}H_{30}N_4O_2S$: C, 75.22; H, 4.98; N, 9.23. Found: C, 75.11; H, 5.09; N, 9.11.

*Synthesis of **30***: **30** was synthesized from 2,2'-(9,9-dibutylfluorene)bis(5-bromoisoindoline-1,3-dione) and trimethylsilylacetylene with a quantitative yield by following the procedure used for the preparation of **27**. White solid; ^{1}H NMR (400 MHz, $CDCl_3$, TMS): δ 8.01 (s, 2H), 7.90 (d, 2H, *J* = 7.8 Hz), 7.85 (d, 2H, *J* = 7.8 Hz), 7.83 (d, 2H, *J* = 8.7 Hz), 7.46 (s, 2H), 7.45 (d, 2H, *J* = 8.7 Hz), 2.00 (4H, t, *J* = 8.2 Hz), 1.13 (4H, m), 0.76 (4H, m), 0.73 (t, 6H, *J* = 7.4 Hz), 0.30 (s, 18H); ^{13}C NMR (100 MHz, $CDCl_3$): δ 167.06, 166.94, 152.21, 140.16, 137.96, 132.18, 130.97, 130.88, 130.05, 127.16, 125.32, 123.83, 121.49, 120.63, 103.12, 100.41, 55.85, 40.02, 26.29, 23.28, 14.08; MS (EI): m/z calcd for $[M]^+$: 760. Found: 760; HRMS (APCI): *m/z* calcd for $C_{47}H_{49}N_2O_4Si_2$ ($[M+H]^+$): 761.3231. Found: 761.3209.

*Synthesis of **34***: **34** was synthesized from **30** with a yield of 56% by following the procedure used for the preparation of **31**. White solid; ^{1}H NMR (400 MHz, $CDCl_3$, TMS): δ 8.06 (s, 2H), 7.94 (d, 2H, *J* = 7.8 Hz), 7.89 (d, 2H, *J* = 7.8 Hz), 7.85 (d, 2H, *J* = 8.2 Hz), 7.45 (s, 2H), 7.43 (d, 2H, *J* = 8.2 Hz), 3.38 (s, 2H), 2.00 (4H, t, *J* = 8.7 Hz), 1.13 (4H, m), 0.75 (4H, m), 0.73 (t, 6H, *J* = 7.8 Hz). This compound was used for next step without further purification.

*Synthesis of **F4(PI-BTCN)$_2$***: **F4(PI-BTCN)$_2$** was synthesized from **34** and **35** with a yield of 66% by following the procedure used for the preparation of **MHPI-BTCN**. This compound was purified by column chromatography on silica gel ($CHCl_3$), followed by precipitation using $CHCl_3$ and acetone. Yellow solid; ^{1}H NMR (400 MHz, $CDCl_3$, TMS): δ 8.26 (s, 2H), 8.10 (d, 2H, *J* = 7.8 Hz), 8.09 (d, 2H, *J* = 7.3 Hz), 8.04 (d, 2H, *J* = 7.8 Hz), 7.94 (d, 2H, *J* = 7.3 Hz), 7.85 (t, 2H, *J* = 8.6 Hz), 7.49 (s, 2H), 7.49 (t, 2H, *J* = 8.6 Hz), 2.03 (t, 4H, *J* = 8.2 Hz), 1.14 (m, 4H), 0.78 (m, 4H), 0.75 (t, 6H, *J* = 7.3 Hz); ^{13}C NMR (100 MHz, $CDCl_3$): δ 166.49, 166.39, 154.10, 152.85, 152.16, 140.09, 137.89, 135.28, 132.45, 132.01, 131.90, 130.82, 128.42, 127.07, 125.16, 123.92, 121.48, 121.33, 120.44, 114.86, 106.61, 97.86, 88.27, 55.77, 39.81, 26.15, 23.04, 13.75; MS (MALDI-TOF): *m/z* calcd for $[M]^-$: 934.2. Found: 934.4; HRMS (APCI): *m/z* calcd for $C_{55}H_{35}N_8O_4S_2$ ($[M+H]^+$): 935.2223. Found: 935.2194.

*Synthesis of **38***: **36** (1.00 g, 3.61 mmol) and **37** (416 mg, 3.61 mmol) were placed in a test tube with screw cap and dissolved with DMF (100 mL). The reaction mixture was stirred at 140 °C for 12 h. After being cooled to room temperature and addition of water, the resulting mixture was extracted with ethyl acetate (EtOAc) and the organic layer was washed with water. After removal of the solvent under reduced pressure, the residue was purified by column chromatography on silica gel (hexane/$CHCl_3$ = 2/1) to give **38** (847 mg, 63%). Colorless solid; ^{1}H NMR (400 MHz, $CDCl_3$, TMS, δ): 8.64 (dd, *J* = 8.5, 1.1 Hz, 1H), 8.56 (dd, *J* = 8.5, 1.1 Hz, 1H), 8.40 (d, *J* = 7.8 Hz, 1H), 8.04 (d, *J* = 7.8 Hz, 1H), 7.85 (td, *J* = 8.5, 1.1 Hz, 1H), 5.25 (m, 1H), 2.18 (m, 1H), 1.89 (m, 1H), 1.56 (d, *J* = 7.3 Hz, 3H), 1.27 (m, 6H), 0.83 (t, *J* = 6.9 Hz, 3H); ^{13}C NMR (100 MHz, $CDCl_3$, δ):163.88, 163.84, 132.68, 131.80, 131.02, 130.92, 130.26, 129.68, 128.89, 127.95, 123.44, 122.58, 49.85, 33.42, 31.63, 26.73, 22.54, 18.26, 14.03; MS (EI) *m/z* 373 (M^+); Anal. calcd for $C_{19}H_{20}BrNO_2$: C 60.97, H 5.39, N 3.74; found: C 60.89, H 5.43, N 3.64.

*Synthesis of **41***: **39** (300 mg, 0.75 mmol), **40** (819 mg, 1.79 mmol) and $Pd(PPh_3)_4$ (172 mg, 0.15 mmol) were placed in a round-bottomed flask and dissolved with DMF (100 mL). The reaction mixture was stirred at 90 °C for 12 h. After being cooled to room temperature, the solvent was evaporated under reduced pressure. The residue was purified by column chromatography on silica gel (hexane/$CHCl_3$ = 2/1) to give **41** (407 mg, 95%). Yellow solid; ^{1}H NMR (400 MHz, $CDCl_3$, TMS, δ): 8.29 (s, 2H), 8.19 (s, 2H), 7.16 (s, 2H), 2.75 (t, *J* = 8.0 Hz, 4H), 1.75 (m, 4H), 1.45-1.34 (br, 12H), 0.92 (t, *J* = 7.3 Hz, 6H); ^{13}C NMR (100 MHz, $CDCl_3$, δ): 152.23, 151.84, 144.63, 138.11, 134.75, 130.46, 128.55, 126.32, 122.63, 114.69, 31.73, 30.67, 30.49, 29.09, 22.67, 14.16; MS (EI) *m/z* 577 (M^+); HRMS (ACPI) calcd for $C_{30}H_{33}N_4S_4$ ($[M+H]^+$): 577.1588, found: 577.1578.

*Synthesis of **42***: To a stirred solution of **41** (407 mg, 0.71 mmol) in THF (140 mL) was added NBS (276 mg, 1.55 mmol), and the resulting mixture was stirred at 50 °C for 6 h. After being cooled to room temperature, the reaction was quenched by the addition of $NaHCO_3$ aq., and the resulting mixture was extracted with CH_2Cl_2 and the organic layer was washed with water. After removal of the solvent under reduced pressure, the residue was purified by column chromatography on silica gel (hexane/$CHCl_3$ = 1/1) to give **42** (416 mg, 80%). Orange solid; ^{1}H NMR (400 MHz, $CDCl_3$, TMS, δ): 8.15 (s, 2H), 7.96 (s, 2H), 2.69 (t, *J* = 7.3 Hz, 4H), 1.72 (m, 4H), 1.44-1.35 (br, 12H), 0.92 (t, *J* = 6.9 Hz, 6H); ^{13}C NMR (100 MHz, $CDCl_3$, δ): 151.53, 151.30, 143.27, 137.41, 134.15, 129.27, 127.24, 125.04,

114.38, 112.92, 31.68, 29.76, 29.71, 29.07, 22.68, 14.18; MS (EI) *m/z* 732 (M^+); Anal. calcd for $C_{30}H_{30}BrN_4O_4$: C 49.05, H 4.12, N 7.63; found: C 49.08, H 4.13, N 7.79.

*Synthesis of **43***: **42** (416 mg, 0.57 mmol), trimethylsilylacetylene (167 mg, 0.1.70 mmol), CuI (22 mg, 0.11 mmol), and Pd(PPh3)4 (131 mg, 0.11 mmol) were placed in a test tube with screw cap and dissolved with toluene (10 mL) and triethylamine (5 mL). The reaction mixure was stirred at 80 °C for 6 h. After being cooled to room temperature, the reaction mixture was concentrated under reduced pressure and then purified by column chromatography on silica gel (hexane/$CHCl_3$ = 1/1) to give **43** (150 mg, 34%). Orange solid; ^{1}H NMR (400 MHz, $CDCl_3$, TMS, δ): 8.25 (s, 2H), 8.08 (s, 2H), 2.80 (t, *J* = 7.6 Hz, 4H), 1.75 (m, 4H), 1.41-1.35 (br, 12H), 0.92 (t, *J* = 6.9 Hz, 6H), 0.30 (s, 18H); ^{13}C NMR (100 MHz, $CDCl_3$, δ): 152.09, 151.67, 149.85, 137.80, 134.41, 129.82, 127.76, 126.30, 121.11, 114.98, 103.72, 97.33, 31.73, 30.22, 29.83, 29.11, 22.75, 14.26, 0.07; MS (EI) *m/z* 768 (M^+); Anal. calcd for $C_{40}H_{48}N_4S_4Si_2$: C 62.45, H 6.29, N 7.28; found: C 62.45, H 6.35, N 7.17.

*Synthesis of **44***: **43** (150 mg, 0.20 mmol), K_2CO_3 (108 g, 0.78 mmol), THF (6 mL) and MeOH (3 mL) were placed in a test tube and the resulting slurry was stirred for 1 h. After celite filtration and extraction with CH_2Cl_2, the filtrate was condensed under reduced pressure. The residue was purified by column chromatography on silica gel (hexane/$CHCl_3$ = 1/1) to give **44** (80 g, 66%). Orange solid; ^{1}H NMR (400 MHz, $CDCl_3$, TMS, δ): 8.25 (s, 2H), 8.09 (s, 2H), 3.63 (s, 2H), 2.82 (t, *J* = 7.8 Hz, 4H), 1.75 (m, 4H), 1.44-1.35 (br, 12H), 0.92 (t, *J* = 5.5 Hz, 6H); ^{13}C NMR (100 MHz, $CDCl_3$, δ): 151.73, 151.39, 150.04, 137.98, 134.08, 129.58, 127.39, 126.10, 119.62, 114.90, 85.47, 76.53, 31.66, 30.21, 29.70, 29.09, 22.68, 14.16; MS MALDI-TOF (1,8,9-trihydroxyanthracene matrix) *m/z* 624.02 (M^-). This compound was used for next step without further purification.

*Synthesis of **asNTz-NP-F***: **44** (80 mg, 0.13 mmol), **45** (170 mg, 0.38 mmol), CuI (5 mg, 0.03 mmol), and $Pd(PPh_3)_4$ (30 mg, 0.03 mmol) were placed in a test tube with screw cap and dissolved with toluene (5 mL) and triethylamine (2.5 mL). The reaction mixure was stirred at 110 °C for 6 h. After being cooled to room temperature, the reaction mixture was concentrated under reduced pressure and then purified by column chromatography on silica gel ($CHCl_3$), followed by purification with preparative GPC ($CHCl_3$) to give ***asNTz-NP-F*** (84 mg, 42%). Red solid; ^{1}H NMR (400 MHz, $CDCl_3$, TMS, δ): 8.76 (d, *J* = 7.3 Hz, 2H), 8.71 (d, *J* = 7.0 Hz, 2H), 8.62 (d, *J* = 7.3 Hz, 2H), 8.32 (s, 2H), 8.19 (s, 2H), 7.98 (d, *J* = 7.0 Hz, 2H), 7.89 (t, *J* = 7.3 Hz, 2H), 7.86 (d, *J* = 8.2 Hz, 2H), 7.75 (dd, *J* = 7.8, 1.8 Hz, 2H), 7.40-7.35 (m, 3H), 7.31-7.29 (m, 2H), 3.03 (t, *J* = 7.8 Hz, 4H), 2.00 (t, *J* = 8.0 Hz, 8H), 1.91 (m, 4H), 1.47-1.38 (m, 8H), 1.15-1.09 (m, 8H), 0.93 (t, *J* = 8.2 Hz, 6H), 0.87-0.81 (m, 4H), 0.72 (t, *J* = 8.0 Hz, 12H), 0.74-0.67 (m, 8H); ^{13}C NMR (100 MHz, $CDCl_3$, δ): 163.86, 163.61, 151.66, 151.59, 151.23, 151.18, 150.44, 141.31, 140.46, 139.66, 133.87, 131.85, 131.66, 130.85, 130.36, 130.07, 129.81, 128.16, 127.36, 127.30, 127.15, 127.10, 126.86, 126.03, 126.01, 123.50, 123.20, 122.97, 122.14, 120.30, 120.08, 120.02, 114.97, 99.91, 95.20, 92.36, 55.21, 39.98, 31.76, 30.48, 30.34, 29.41, 26.02, 23.09, 22.78, 14.24, 13.87; MS MALDI-TOF (1,8,9-trihydroxyanthracene matrix) *m/z* 1566.40 (M^-); Anal. calcd for $C_{100}H_{90}N_6O_4S_6$: C 76.60, H 5.79, N 5.36; found: C 76.34, H 5.88, N 5.24.

Synthesis of ***asNTz-NP-MH***: **44** (90 mg, 0.14 mmol), **38** (129 mg, 0.35 mmol), CuI (5 mg, 0.03 mmol), and $Pd(PPh_3)_4$ (33 mg, 0.03 mmol) were placed in a test tube with screw cap and dissolved with toluene (5 mL) and triethylamine (2.5 mL). The reaction mixure was stirred at 110 °C for 6 h. After being cooled to room temperature, the reaction mixture was concentrated under reduced pressure and then purified by column chromatography on silica gel ($CHCl_3$), followed by purification with preparative GPC ($CHCl_3$) to give ***asNTz-NP-MH*** (95 mg, 54%). Red solid; ^{1}H NMR (400 MHz, $CDCl_3$, TMS, δ): 8.64 (d, J = 7.8 Hz, 2H), 8.61 (d, J = 7.3 Hz, 2H), 8.52 (d, J = 7.8 Hz, 2H), 8.28 (s, 2H), 8.13 (s, 2H), 7.91 (d, J = 7.3 Hz, 2H), 7.82 (t, J = 7.8 Hz, 2H), 5.27 (m, 2H), 2.20-2.15 (m, 4H), 1.93-1.81 (m, 4H), 1.58 (d, J = 6.9 Hz, 6H), 1.55-1.48 (d, J = 6.9 Hz, 8H), 1.43-1.22 (m, 20H), 0.90 (t, J = 7.1 Hz, 6H), 0.84 (t, J = 7.0 Hz, 6H); ^{13}C NMR (100 MHz, $CDCl_3$, δ): 164.16, 163.92, 151.64, 151.27, 150.24, 139.45, 134.04, 131.33, 130.67, 130.04, 129.72, 127.96, 127.31, 127.09, 126.49, 126.09, 123.40, 122.40, 122.33, 119.96, 115.03, 114.96, 95.12, 91.82, 49.88, 33.55, 31.71, 30.96, 30.38, 30.22, 29.36, 26.84, 22.74, 22.61, 18.30, 14.21, 14.08; MS MALDI-TOF (1,8,9-trihydroxyanthracene matrix) *m/z* 1210.00 (M^-); HRMS (ACPI) calcd for $C_{72}H_{71}N_6O_4S_4$ ($[M+H]^+$): 1211.4420, found: 1211.4385.

4.6 References

1 Y. Ie, S. Jinnai, M. Karakawa and Y. Aso, *Chem. Lett.*, 2015, **44**, 694.

2 S. Chatterjee, Y. Ie, M. Karakawa and Y. Aso, *Adv. Funct. Mater.*, 2016, **26**, 1161.

3 Y. Ie, T. Sakurai, S. Jinnai, M. Karakawa, K. Okuda, S. Mori and Y. Aso, *Chem. Commun.*, 2013, **49**, 8386.

4 Y. Ie, S. Jinnai, M. Karakawa, A. Saeki, S. Seki and Y. Aso, *J. Fluorine Chem.*, 2015, **174**, 75.

5 Y. Liu, J. Y. L. Lai, S. Chen, Y. Li,K. Jiang, J. Zhao, Z. Li, H. Hu,T. Ma, H. Lin, J. Liu, J. Zhang, F. Huang, D. Yu and H. Yan, *J. Mater. Chem. A*, 2015, **3**, 13632; J. Lee, R. Singh, D. H. Sin, H. G. Kim, K. C. Song and K. Cho, *Adv. Mater.*, 2016, **28**, 69; J. Yi, Y. Wang, Q. Luo, Y. Lin, H. Tan, H. Wang and C.-Q. Ma, *Chem. Commun.*, 2016, **52**, 1649.

6 C. Zhan and J. Yao, *Chem. Mater.*, 2016, **28**, 1948; Y. Zang, C.-Z. Li, C. C. Chueh, S. T. Williams, W. Jiang, Z.-H. Wang, J.-S. Yu and A. K. Y. Jen, *Adv. Mater.*, 2014, **26**, 5708; Y. Liu, C. Mu, K. Jiang, J. Zhao, Y. Li, L. Zhang, Z. Li, J. Y. L. Lai, H. Hu, T. Ma, R. Hu, D. Yu, X. Huang, B. Z. Tang and H. A. Yan, *Adv. Mater.*, 2015, **27**, 1015; H. Lin, S. Chen, H. Hu, L. Zhang, T. Ma, J. Y. L. Lai, Z. Li, A. Qin, X. Huang, B. Tang and H. Yan, *Adv. Mater.*, 2016, **28**, 8546; N. Qlu, X. Yan, H. Zhang, X. Wan, C. Li, F. Llu, H. Zhang, T. P. Russell and Y. Chen, *Chem. Mater.*, 2016, **28**, 6770.

7 Z. Liu, Y. Wu, Q. Zhang and Z. Gao, *J. Mater. Chem. A*, 2016, DOI: 10.1039/c6ta06978a.

8 N. E. Jackson, B. M. Savole, T. J. Marks, L. X. Chen and M. A. Ratner, *J. Phys. Chem. Lett.*, 2015, **6**, 77.

9 H. Yoshida, *Chem. Phys. Lett.*, 2012, **539-540**, 180; H. Yoshida, *Anal. Bioanal. Chem.*, 2014, **406**, 2231; H. Yoshida, *J. Electron Spectrosc. Relat. Phenom.*, 2015, **204**, 116.

10 Y. Liang, Z. Xu, J. Xia, S.-T. Tsai, Y. Wu, G. Li, C. Ray and L. Yu, *Adv. Mater.*, 2010, **22**, E135.

11 J.-L. Brédas, J. E. Norton, J. Cornil and V. Coropceanu, *Acc. Chem. Res.*, 2009, **42**, 1691; T. M. Clarke and J. R. Durrant, *Chem. Rev.*, 2010, **110**, 6736; R. A. J. Janssen and J. Nelson, *Adv. Mater.*, 2013, **25**, 1847.

12 S. D. Dimitrov and J. R. Durrant, *Chem. Mater.*, 2014, **26**, 616; G. G. Malliaras, J. R. Salem, P. J. Brock and C. Scott, *Phys. Rev. B*, 1998, **58**, 13411; C. Goh, R. J. Kline, M. D. McGehee, E. N. Kadnikova and J. M. J. Fréchet,

Appl. Phys. Lett., 2005, **86**, 122110.

13 H. Yoshida, *Rev. Sci. Instrum.*, 2014, **85**, 016101.

14 D. H. Kaelble and K. C. Uy, *J. Adhesion*, 1970, **2**, 50.

15 P. K. Iyer and S. Wang, *Tetrahedron Lett.*, 2006, **47**, 437.

16 A. M. Ramos, S. C. J. Meskers, E. H. A. Beckers, R. B. Prince, L. Brunsveld and R. A. J. Janssen, *J. Am. Chem. Soc.*, 2004, **126**, 9630.

17 B. A. G. Hammer, M. Baumgarten and K. Müllen, *Chem. Commun.*, 2014, **50**, 2034.

18 P. Rajasingh, R. Cohen, E. Shirman, L. J. Shimon and B. Rybtchinski, *J. Org. Chem.*, 2007, **72**, 5973.

19 X.-F. Wu, W.-F. Fu, Z. Xu, M. Shi, F. Liu, H.-Z. Chen, J.-H. Wan and T. P. Russell, *Adv. Funct. Mater.*, 2015, **25**, 5954.

20 L.-Y. Lin, C.-W. Lu, W.-C. Huang, Y.-H. Chen, H.-W. Lin and K.-T. Wong, *Org. Lett.* 2011, **13**, 4962.

21 S. Mataka, K. Takahashi, Y. Ikezaki, T. Hatta, A. Tori-i and M. Tashiro, *Bull. Chem. Soc. Japan*, 1991, **64**, 68.

22 F. P. V. Koch, P. Smith and M. Heeney, *J. Am. Chem. Soc.*, 2013, **135**, 13695.

Conclusion

In this thesis, the design, synthesis, properties, and OPV characterisitcs of electron acceptors were discussed towards clarification of relationship among structural feature, physical properties, thin-film properties, and photovoltaic performances. The major results in each chapter of this thesis are summarized as follows.

In chapter 1, the author designed and synthesized a series of tetrathienyl silane based acceptors end-capped with dicyanomethylene-substituted difluorocyclopenta[*b*]thiophene units. From the comparison of planar and non-planar acceptors, 3-D arrangement of extended π-electron compounds were found to be advantageous in photocurrent generation. However the PCE of 3-D acceptors were at quite low level. Toward the further evaluation of structure−properties−OPV performances relationship, improved-performance acceptor materials with synthetic flexibility were considered to be essential.

In chapter 2, the author designed and investigated linearly extended π-conjugated compounds end-capped with phthalimide and phthaldithioimide units. Among the investigated acceptors, benzothiadiazole-based compound with phthalimide terminal groups showed a moderate PCE of 1.58%. In addition, from the evaluation of molecular properties, electron-mobilities and thin-film nature of acceptors, high SFE and γ^{d} values were found to be the characteristic property of high performance acceptors.

In the next chapter, it was mainly focused on the relationship among the thin-film properties and OPV characteristics of diethynylbenzothiadiazole/phthalimide based acceptors. Thanks to its synthetic flexibility, the author was able to prepare series of acceptors introduced the different type of solubilizing groups and arylimides. Among the investigated acceptors, the highest PCE of 2.05% were achieved by utilizing **Ph-MH**; low cyristallinity, low μ_e^{FET}, and high γ^{d} material. From the detailed investigation of crystallinities, μ_e, and SFE (and γ^{d}) values, it was found that the high γ^{d} values were originated to exposed π-conjugated framework at the acceptor interface. Furthermore, the correlation between γ^{d} of acceptors and its OPV performances were also found within the investigated materials in this chapter. Detailed analysis revealed that charge-separation step was facilitated when high γ^{d} acceptor was employed. Therefore, designing high γ^{d} acceptors should be one promising guideline towards the development of new materials.

At the next step of research, cyano-substituted benzothiadiazole-based acceptors and *as*NTz based acceptors were synthesized and examined. As the results of OPV characteristics evaluation and SFE estimation, the correlation between γ^{d} and J_{SC} was not clear in these systems. The author hypothesized that the correlation is effective when the electron accepting units are exposed toward interface and, therefore, 3-D arranged molecule surrounded with extended π-electron acceptor units is considered to be a promising acceptor material because which is considered to expose its acceptor units toward interface. In the chapter 4, the structure–properties–OPV characteristics of 3-D acceptors were investigated using PDI based materials. As the results, the PCEs of 3-D molecules were distributed between 0.02 and 2.02% and the correlation γ^{d} and J_{SC} was found within the investigated acceptors. From the detailed analysis of blend-film properties, the charge-separation process has mainly influenced the photovoltaic characteristics of linearly extended acceptors and 3-D acceptors.

This thesis discussed the relationship among the chemical structure, physical properties, thin-film properties, and photovoltaic performances of linealy extended acceptor materials and 3-D acceptor materials. In both cases, the

OPV performances mainly originated from the difference of the J_{SC} and which were mainly governed by the efficiency of charge separation into free carrier at the donor–acceptor interfaces. The thesis revealed that increase of exposed π-conjugated framework at the interface leads to the increase of γ^{d} value, and the orientation of acceptor π-plane toward D–A interfaces is desirable for the efficient charge separation. As described in this thesis, improvement of J_{SC} value was one of the key challenge for developments of acceptor materials. This thesis provides promising strategy for the design of non-fullerene acceptor materials.

List of Publications

(1) Arenedithiocarboxyimide-containing extended π-conjugated systems with high electron affinity
Yutaka Ie, Seihou Jinnai, Masashi Nitani, Yoshio Aso
Journal of Materials Chemistry C, Vol. 1, 5373–5380 (2013).

(2) Synthesis, properties, and semiconducting characteristics of electron-transporting three-dimensional π-conjugated compounds containing dicyanomethylene-substituted difluorocyclopenta[*b*]thiophene
Yutaka Ie, Seihou Jinnai, Makoto Karakawa, Akinori Saeki, Shu Seki, Yoshio Aso
Journal of Fluorine Chemistry, Vol. 174, 75–80 (2015).

(3) Electron-accepting π-Conjugated Systems Based on Cyclic Imide and Cyano-substituted Benzothiadiazole for Non-fullerene Organic Photovoltaics
Yutaka Ie, Seihou Jinnai, Makoto Karakawa, Yoshio Aso
Chemistry Letters, Vol. 44, 694–696 (2015).

(4) Electron-Accepting π-Conjugated Systems for Organic Photovoltaics: Influence of Structural Modification on Molecular Orientation at Donor−Acceptor Interfaces
Seihou Jinnai, Yutaka Ie, Makoto Karakawa, Tom Aernouts, Yukihiko Nakajima, Shogo Mori, Yoshio Aso
Chemistry of Materials, Vol. 28, 1705–1713 (2016).

(5) Three-dimensional π-conjugated compounds as non-fullerene acceptors in organic photovoltaics: the influence of acceptor unit orientation at phase interfaces on photocurrent generation efficiency
Seihou Jinnai, Yutaka Ie, Yuki Kashimoto, Hiroyuki Yoshida, Makoto Karakawa, Yoshio Aso
Journal of Materials Chemistry A, in press, DOI:10.1039/c6ta10608k (2017).

List of Supplementary Publications

(1) Three-Dimensional Electron-Accepting Compounds Containing Perylene Bis(dicarboximide)s as n-Type Organic Photovoltaic Materials
Yutaka Ie, Takahiro Sakurai, Seihou Jinnai, Makoto Karakawa, Kouichi Okuda, Shogo Mori, Yoshio Aso
Chemical Communications, Vol. 49, 8386–8388 (2013).

(2) Electron-donor function of methanofullerenes in donor–acceptor bulk heterojunction systems
Yutaka Ie, Makoto Karakawa, Seihou Jinnai, Hiroyuki Yoshida, Akinori Saeki, Shu Seki, Shunsuke Yamamoto, Hideo Ohkita, Yoshio Aso
Chemical Communications, Vol. 50, 4123–4125 (2014).

Acknowledgements

Foremost, the author wishes to express his sincerest gratitude to Professor Yoshio Aso for his continuous guidance and suggestion of my Ph.D study and research.

The author is deeply grateful to Associate Professor Yutaka Ie for his helpful advice and discussions throughout the duration of this work.

The author is also indebted to Assistant Professors Makoto karakawa and Masashi Nitani for the invaluable discussions, technical assistance, and helpful suggestions.

The author would like to thank Professor Shu Seki and Associate Professor Akinori Saeki for FP-TRMC measurements and useful discussion.

The author thank Professor Hiroyuki Yoshida and the laboratory member at Graduate School of Integration Science, Chiba University, for LEPIS measurement and suggestions.

The author also thank Associate Professor Shogo Mori and the laboratory member at Faculty of Textile Science and Technology, Shinshu University, for charge density measurements and useful discussion.

The author wishes to thank Professor Yasujiro Murata and Associate Professor Atsushi Wakamiya at the Graduate School of Engineering, Kyoto University, for PESA measurements and useful discussion.

The author grateful to Dr. Tom Aernouts and Ms. Tamara Merckx at Interuniversity Microelectronics Centre (IMEC), Belgium, for inverted type OPV fabrication and evaluation.

The author thanks all labmate: Dr. Masaru Endo, Dr. Tomoya Hirose, Dr. Jianming Huang, Dr. Chatterjee Shreyam, Dr. Shunsuke Tamba, Mr. Takahiro Nozawa, Mr. Kazufumi Nishida, Mr. Takahiro Sakurai, Mr. Masashi Ueta, Ms. Aya Kojima, Mr. Kazunari Tanaka, Mr. Chihiro Sato, Ms. Saori Tone, Ms. Yi Wang, Mr. Shohei Sasada, Ms. Aya Tashiro, Ms. Ayana Uchida, Mr. Yuji Okamoto, Ms. Nana Kawaguchi, Mr. Koki Morikawa, Mr. Keitaro Yamamoto, Mr. Takuya Inoue and Mr. Kakeru Izuno for their useful advices, discussions, and creating a pleasant atmosphere.

The author acknowledge Japan Society for the Promotion of Science (JSPS) for Young Scientists for financial support during his PhD program.

Finaly, the author would like to express his sincerest thanks to his mother, Chiyoko Jinnai for her perpetual supports, encouragement during the graduate study.

Seihou Jinnai

Ibaraki, Osaka
January 2017